Soft Multifunctional Composites Using Liquid Metal

Submitted in partial fulfillment of the requirements for

the degree of

Doctor of Philosophy

in

Civil and Environmental Engineering Department

Navid Kazem

M.S., Civil and Environmental Engineering, Carnegie Mellon University

B.S., Civil Engineering, Sharif University of Technology

Carnegie Mellon University
Pittsburgh, PA

May, 2018

Acknowledgement

First of all, I would like to thank my advisor Prof. Carmel Majidi for giving me the opportunity to work at Soft Materials Laboratory and supporting me throughout my PhD. It has been an amazing journey with a lot of highs and some downs that without Carmel's support wouldn't have been possible. I will always be grateful. I would also like to thank Prof. Craig Maloney who helped shaping my scientific thinking during the first 2 years of my PhD program. Additionally, I thank all of my lab-mates for making the work in the lab much more enjoyable with having many thoughtfull conversations. I learned a lot from being around all of you. I would like to specially thank my thesis committee members, Prof. Whitesides, Prof. Dayal, and Prof. Malen. It has been an honor to have Prof. Whitesides in my committee and I am grateful for it.

I would like to thank my parents, Soudabeh Jafari Salim and Dr. Hossein Kazem for their unconditional support and love. I am grateful for all of your encouragements for continuing my grad school, and can't thank them enough for all they have done for me. I wished they were able to be here with me; nonetheless I can feel their love from the other side of the world. I would also like to thank my brother, Dr. Hamid Kazem. You have always (throughout my life) been a few steps ahead of me and made all the obstacle in life much easier to deal with.

I also must thank my friends in Pittsburgh (Hannah, Reza, Milad, Salim, Yashar, and Mohammad), AC Mellon club soccer team-mates (Andrew, Kosa, and Kyle) and all the members of Persian Student Organization & Persian Panthers who welcomed me into their lives and was a big part of keeping me mentally strong during my graduate school.

Finally, I would like to thank my research sponsors for funding my work. This work was supported by NSF, CMMI (Div Of Civil, Mechanical, and Manufacturing Innovation; Dr. Mary M. Toney; Award 1635824), Air Force Office of Scientific Research Young Investigator Program (Mechanics of Multifunctional Materials and Microsystems; Dr. Les Lee; Award FA9550-13-1-0123) and the Innovation Fellowship from Swartz Center for Entrepreneurship.

Abstract

Progress in the fields of wearable computing, soft robotics and bio hybrid engineering depend on new classes of soft multifunctional materials that match the mechanical properties of soft biological tissue and possess high toughness, while having metal-like electrical and thermal properties. Elastomers and polymers are popular because they are both soft (softer than skin, i.e. elastic modulus in the order of hundreds of kPa) and highly stretchable (strain at failure of up to 700-900%). However they generally have poor electrical and thermal properties, and low resistance to tear propagation. Traditionally, rigid metallic and ceramic fillers have been embedded inside elastomers in order to increase electrical, thermal and toughness properties of them. Even though these fillers can increase the electrical and thermal functionalities of the composites, they significantly deteriorate their extreme mechanical functionality; the same properties that make elastomers popular in the first place. Due to the extreme mechanical mismatch between the soft host matrix and rigid inclusions, the fillers significantly increase the stiffness and decrease the stretchability of the elastomers. I am taking a different approach by embedding micro scale inclusions of *liquid metals* inside elastomers. Gallium alloys (EGaIn, eutectic gallium indium; or Galinstan, gallium indium and tin) are of particular interest due to their low melting temperature (EGaIn $T_m = 15.5°C$, and Galinstan $T_m = -19°C$), negligible vapor pressure, and non-toxicity. In an oxygenated environment a thin (0.5-3 nm) layer of gallium oxide forms on the surface and makes the liquid moldable and printable. Since the liquid metals have high electrical and thermal conductivity ($\sigma = 3.46 \times 10^6\, S/m$ and $k = 26.4\, W/m.K$), using them as fillers enhances the dielectric and thermal properties of composites. The integration of LM microdroplets increases the dielectric constant of liquid metal embedded elastomers (LMEEs) to over 400% and displays a low dielectric dissipation factor. Importantly, This enhancement in dielectric performance is achieved without degradation in mechanical compliance and stretchability of the composite. The liquid inclusions inside the elastomer eliminates the internal compliance mismatch occurs in rigid fillers composites and thus preserve the mechanics of host elastomer. By shear mixing a soft silicone elastomer and EGaIn, I achieved stiffness of less than 100 kPa and maximum strain at break of ~600%, virtually similar to the host material. Furthermore, soft dielectric

materials typically exhibit poor heat transfer properties due to the dynamics of phonon transport, which constrain thermal conductivity (k) to decrease monotonically with decreasing elastic modulus (E). This thermal-mechanical trade-off is limiting for applications that require materials with both high thermal conductivity and low mechanical stiffness. With LMEE composites, I overcome this constraint with an electrically insulating composite that exhibits an unprecedented combination of metal-like thermal conductivity, an elastic compliance. I achieve a $\sim 25\times$ increase in thermal conductivity (4.7 ± 0.2 W/mK) over the base polymer (0.20 ± 0.01 W/mK) under stress-free conditions and a $\sim 50\times$ increase (9.8 ± 0.8 W/mK) when strained. This exceptional combination of thermal and mechanical properties is enabled by a unique thermal-mechanical coupling in which the liquid inclusions can be elongated and align with each other to create thermally conductive pathways in situ. In addition, this unique ultra deformability of liquid inclusions inside elastomers can give rise to desirable fracture properties. Exploiting this high deformability of LMs, I observed that LMEEs exhibit multi-modal toughening, where the fracture energy dramatically increases by means of (i) increasing energy dissipation, (ii) adaptive crack movement, and (iii) effective elimination of the crack tip. Using pure shear toughness measurements, I observed an increase in fracture toughness by up to $50\times$ (from $250 \pm 50\, J/m^2$ to $11,900 \pm 2,600\, J/m^2$) over an unfilled polymer. The above-mentioned combined properties arise from the deformability and dynamic rearrangement of the LM inclusions during loading. Hence, the extent of temperatures in which the micron-sized inclusions phase remains liquid is significantly important for reliable performance. Surprisingly, micro droplets of EGaIn inside a silicone elastomer remain liquid above $T = -65°C$. This reduction in freezing temperature of EGaIn particles is due to i) supercooling of the liquid metal ii) micron scale size of the inclusions, and ii) existence of smooth layer of elastomer isolating each inclusion. In closing, a combination of i) elasticity similar to soft biological tissue, ii) metal-like thermal and dielectric properties, and iii) ultra toughness, with a wide range of temperatures that these properties remain active, can enable elastomers to play a more active role in wearable computing, soft robotics and and bio-inspired engineering applications.

Contents

List of Figures

Chapter 1

Introduction

Reference:

N. Kazem, T. Hellebrekers, and C. Majidi, "*Soft Multifunctional Composites and Emulsions with Liquid Metals*", Advanced Materials, 2017.

Machines and electronics composed of rigid metals, plastics, and semiconductors can be engineered to be extremely precise, powerful, and applicable to a wide range of tasks.[1] However, these technologies have poor capabilities for physical interaction with humans due to the extreme mechanical mismatch between the building blocks of these machines and soft tissues. Furthermore, most of the natural environment around us is comprised of soft materials that are able to deform and adapt to their surroundings. Over the last decade, extensive research efforts have been directed toward improving this mechanical mismatch with the goal of making machines and devices that can assist humans and be safe around people. Interdisciplinary fields like soft robotics and bio-hybrid engineering have emerged to address challenges in human-machine interactions and bridge the technological gap necessary to develop multifunctional and human-compatible machines.

To this end, material scientists, chemists, and mechanicians have an especially important role and "*should not miss the opportunity*" to be part of the revolution in robotics and human-machines interaction.[2] In particular, these scientists can promote progress by introducing new classes of soft multifunctional materials that match the mechanical properties of soft biological tissue, possess me-

chanical reliability (toughness), while having metal-like electrical and thermal properties. In the following sections, I discuss recent efforts to create multifunctional soft and stretchable systems. This includes research in elastomer composites,[3,4] graft copolymers,[5] deterministic architectures,[6,7] soft microfluidic,[8,9] and microsolidic[10] systems in which an elastomer is embedded with microchannels of a fluid or low-melting-point material. Next, I review the material choices for engineering soft multifunctional systems and close by presenting the objectives of this dissertation.

1.1 Background

Since the early 2000s, there has been remarkable progress in new classes of soft and stretchable electronics that are mechanically robust and compatible with human tissue.[7] Some of these technologies incorporate soft conductive materials that have been under development for decades: metalized textiles[11], conductive conjugated polymers[12–18], and rubbery nanocomposites composed of a percolating network of metal nanoparticles or carbon allotropes embedded in an elastomer.[19,20] There has also been rapidly growing interest in the use of 1D and 2D nanomaterials for flexible and stretchable electronics.[21–25] This includes 3D aerogels with carbon nanotubes[26] and Ag nanowires[27] (Fig. 1.1a) and related efforts to perform Brownian dynamic simulations on generalized "patchy rods" networks (Fig. 1.1b).[28] Other approaches to stretchable functionality are based on patterning thin metal films into wavy or serpentine shapes that can stretch through elastic bending or torsion.[6] A key advantage of this approach is that it can be extended to thin semiconductor films for stretchable np junctions and logic arrays.[29] Using novel lithography techniques they can be integrated with conventional microelectronics for creating fully-functional circuits on a stretchable carrier medium.[30–39]

In the last decade, there has also been extraordinary progress in the emerging field of *soft-matter electronics* with Ga-based LM alloys such as eutectic gallium-indium (EGaIn, Fig. 1.1d) and gallium-indium-tin (Galinstan).[40–51] Such systems can be influenced by the unique wetting properties and moldability of these alloys[52] (Fig. 1.1e), which have a role in approaches like fluidic injection[53] (Fig. 1.1c and f). More generally, soft-matter electronics represent the class of electronic materials and circuits that are composed entirely of soft condensed matter i.e. materials that deform

under light mechanical loading. These heterogeneous systems typically use soft elastomer[54] as the continuous phase and exhibit bulk mechanical properties similar to that of soft biological tissue. In addition to liquid metal, soft-matter electronics have been successfully demonstrated using ionic microfluidics[55–59] and hydrogels.[60–62]

There have been several review articles that extensively cover the emerging field of Ga-based LM microfluidic electronics. The focus of these articles range from circuit and sensing applications[44,63,64] to emerging fabrication methods based on lithographic, additive, subtractive, and injection-based techniques.[46,50,65] More recent developments in LM microfluidics have been directed towards 3D printing of microfluidic channels[66,67] and applications of LM in antennas and resonators[45,48,51,68–76], electrodes[77–79] and metamaterials[80–82]. In addition, there has been an increased focus on exploring different phenomena like electro-chemistry[48,83–99], wettability, and interfaces[100–103] of liquid metals.

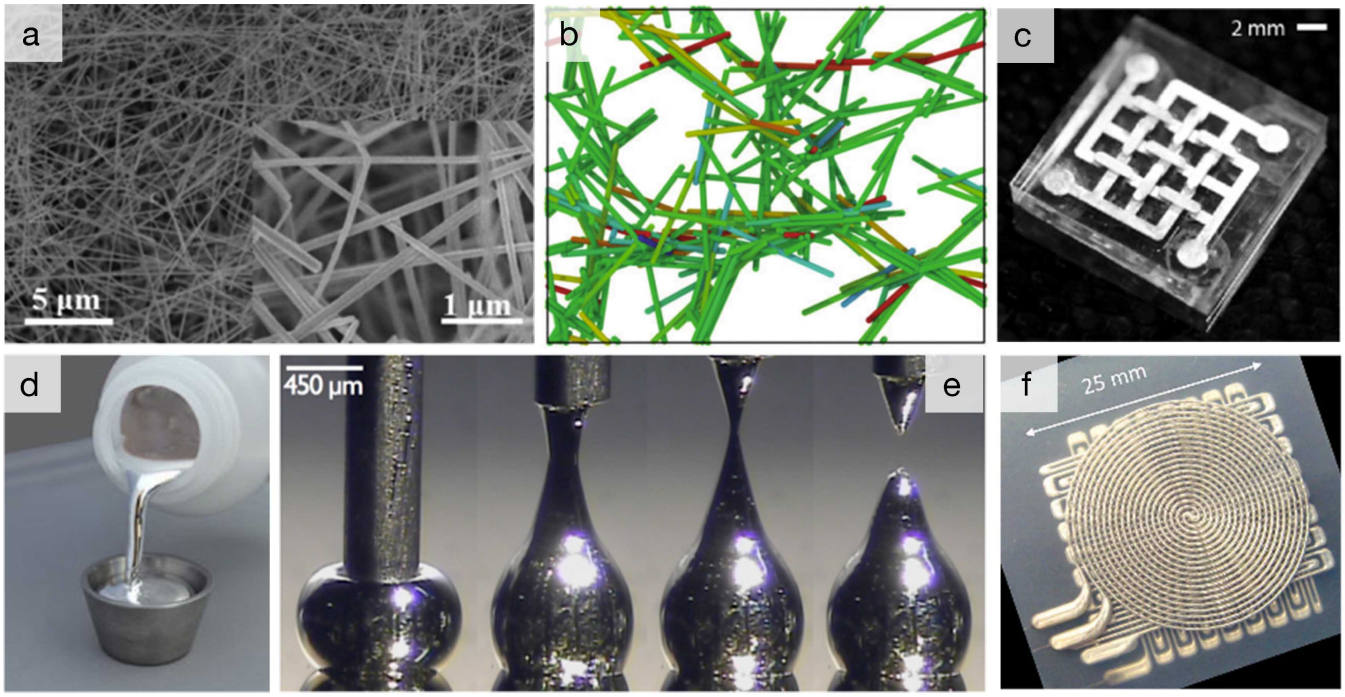

Figure 1.1: a) 3D network of silver nanowire.[27] b) Brownian dynamic simulation of rigid patchy rods showing percolation path at 30% strain.[28] c) Microsolidics with low melting point alloys (LMPA) embedded in polydimethylsiloxane (PDMS).[10] d) Eutectic gallium-indium (EGaIn) alloy is liquid at room temperature (Indium Corp.). e) Deposition of EGaIn showing "moldability" through formation of Ga_2O_3 skin.[52] f) Strain and pressure sensing with microfluidic channels of LM in a soft elastomer.[104]

1.2 Materials Overview

Efforts to incorporate liquid metal into soft elastomers began in the mid-2000s, with early work focused on Pb-based low melting point alloys (LMPA).[10,105] When heated, the molten solder is injected into a microfluidic channel embedded inside an elastomer and then allowed to solidify at room temperature. These so-called "microsolidic" devices (Figure 1.1c) are soft and flexible and represent an inexpensive method for rapid fabrication of flexible printed circuit boards (PCBs). In those applications Field's metal (instead of Pb-based solder) is typically used due to its low melting point and negligible toxicity. Ga-based LM alloys such as eutectic gallium-indium (EGaIn; 75% Ga and 25% In by wt., Figure 1.1d and e) and gallium-indium-tin (Galinstan; 68% Ga, 22% In, 10% Sn) are also popular liquid metals for soft microfluidic electronics (Figure 1.1f).[52,106] Both alloys have a volumetric electrical conductivity of 3.4×10^6 S/m[107] and thermal conductivity of 26.4 W/m·K at ~30°C.[108–110] Compared to Hg, Fr, Cs, and other metals that are liquid at (or near) room temperature, Ga-based alloys are especially attractive for their low viscosity (2 mPa·s)[111], low toxicity[112], and negligible vapor pressure. Moreover, in an oxygenated environment, they form a self-passivating Ga_2O_3 oxide skin that dramatically reduces its surface tension.[83,112,113] The Ga_2O_3 coating has a thickness of ~0.5-3 nm[114,115] and behaves like an elastic membrane that can support a maximum surface stress of 0.5-0.6 N/m.[106,116] When broken, it reforms almost instantaneously, allowing the droplet to be structurally self-stabilizing and moldable.[52,117]

Referring to Fig. 1.2, LM and LMPA systems span a wide range of length scales and architectures: mm-scale channels embedded in elastomer[10,104] (Fig. 1.2A,B), traces deposited on a substrate with a pressurized syringe[118] (Fig. 1.2C), microscale traces printed with soft lithography[119] (Fig. 1.2D), electrochemically manipulated LM traces and fingering phenomena of LMs[83] (Fig. 1.2E), LM droplets fabricated with hundreds of microns length scale using microfluidic devices[120] (Fig. 1.2F), and LM nanospheres synthesized with ultrasonication (Fig. 1.2H).[121] In general, EGaIn, Field's metals, and other low melting point alloys provide a great opportunity for further development and integration of thermal and electrical functionalities in materials that are soft and stretchable without degrading their mechanical performances.

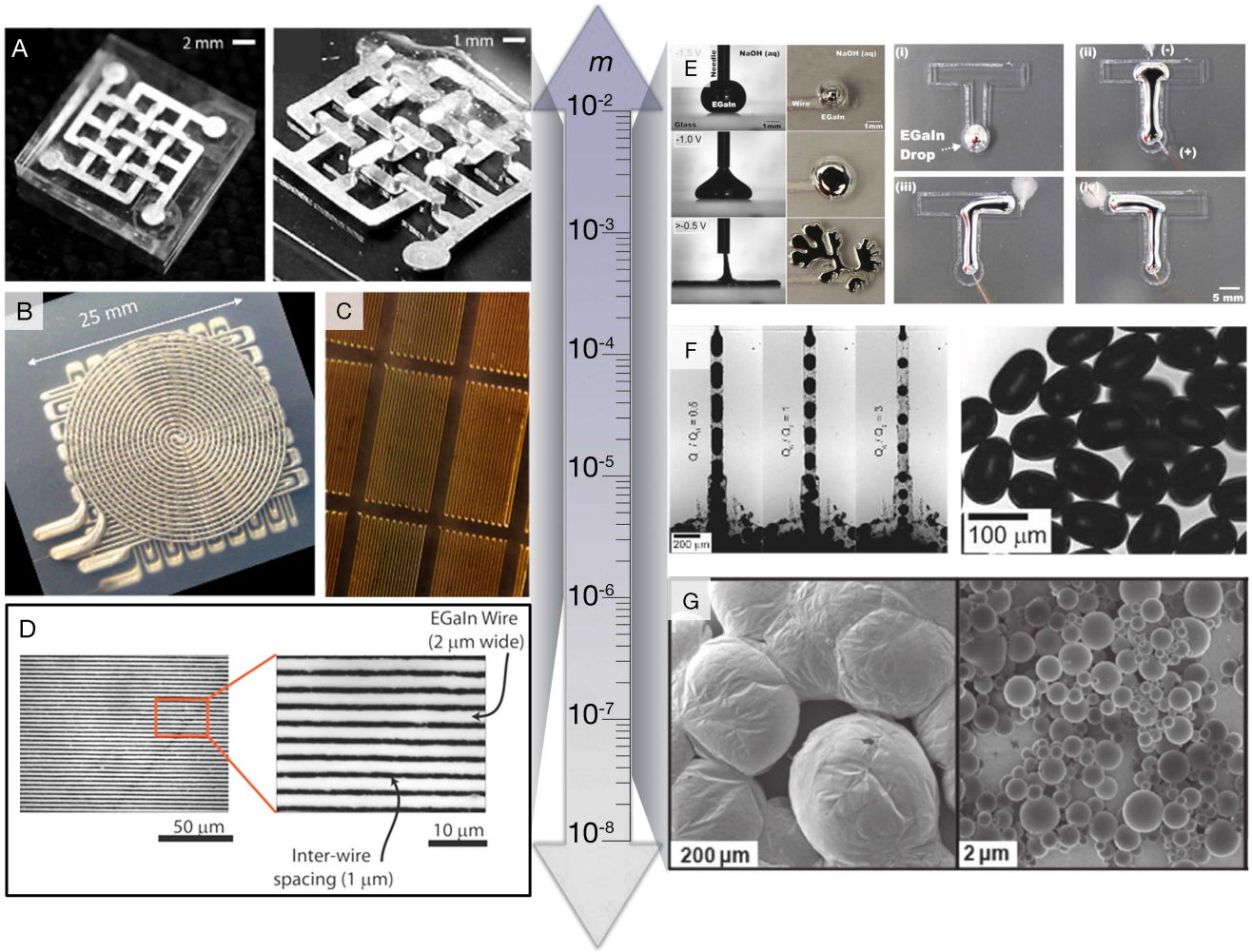

Figure 1.2: Applications of liquid metal alloy at different length scales. A) Microsolidics with LMPA embedded in polydimethylsiloxane (PDMS).[10] B) Strain and pressure sensing with microfluidic channels of LM in a soft elastomer.[104] C) EGaIn strain gauges produced by direct writing using a pressurized syringe.[118] D) Fabrication of microscale EGaIn traces with stamp lithography.[119] E) LM droplet manipulation with voltage-controlled wetting and electrochemistry.[83] F) Synthesis of LM microdroplets with microfluidics.[120] G) Nanoscale LM droplets produced with ultrasonication.[121]

1.3 Objectives and Overview of Dissertation

In my thesis, I study a new class of soft multifunctional composites that have the potential to satisfy many desired material properties required in the fields of soft robotics, wearable computing, and human-machine interactions. Compared to rigid fillers, liquid metals represent a promising alternative for the dispersion phase in elastomer composites. I have focused special attention on "liquid metal embedded elastomer" (LMEE) composites. In LMEE systems, since the inclusions are liquid phase, they significantly reduce the stress concentration at the interface between the matrix and

the fillers. This reduction in stress concentration can result in maintaining the mechanical properties of the host elastomer. In addition, the liquid metals are electrically and thermally conductive and can be used to tailor electrical and thermal properties of elastomers. In order to understand these composites, I have pursued the following:

1) Examine the mechanical properties of LMEE composites

2) Study the enhancement in relative permittivity and thermal conductivity of LMEEs

3) Examine the influence of liquid metals on fracture toughness of the composite

4) Examine influence of temperature on the linear viscoelasticity of LMEEs

The rest of this document is organized as follows: I first discuss the enhancement in dielectric properties of rubbers by embedding liquid metals. Additionally, I describe the microstructure of LMEEs using optical microscope images and nano Computed-Tomography (CT) scan, and characterize the mechanical performances of LMEEs under tensile tests (Chapter 2). This is followed by a discussion about the enhancement in thermal conductivity (Chapter 3), and fracture toughness (Chapter 4) of the composite. In all of the properties that are explained in the following chapters, the ability of LMs to deform and elongate as a result of background strain, plays an essential role in the high functionality of the composite. Therefore, in Chapter 5, I investigate the extent of temperatures in which low melting point alloys stay liquid inside elastomers, and hence LMEEs remain highly functional. In the end, I will make concluding remarks and give my perspective on the relevant future research directions.

Chapter 2

Liquid Metal Embedded Elastomers, High-k Dielectric and Mechanical Properties

Reference:

M. D. Bartlett*, A. Fassler*, N. Kazem, E. J. Markvicka, P. Mandal, and C. Majidi, "*Stretchable, High-k Dielectric Elastomers through Liquid-Metal Inclusions*", Advanced Materials, 2016.

and

N. Kazem*, M. D. Bartlett*, M. J. Powell-Palm*, X. Huang, W. Sun, J. A. Malen, and C. Majidi, "*High Thermal Conductivity in Soft Elastomers With Elongated Liquid Metal Inclusions*", Proceedings of the National Academy of Science, 2017.

2.1 Introduction

Soft electronic systems capable of sensing, actuating, and energy harvesting are key components for emerging applications in wearable electronics, bio-compatible machines and soft robotics.[122–126] Traditionally, the electronic properties of rubbery polymers like silicones, polyurethanes or copolymers such as styrene ethylene butylene styrene are tailored by adding 10 - 30 % by volume of inorganic fillers such as Ag powder, Ag-coated Ni microspheres, structured carbon black (CB), exfoliated graphite, carbon nanotubes, BaTiO3, TiO2, or other metallic, carbon-based, or ceramic micro/nanoparticles.[7,127–132] Although rigid particles have been incorporated into silicones, urethanes and acrylate-based elastomers to increase their dielectric constant,[133] the loadings required to achieve significant electric property enhancement can degrade the mechanical properties of these soft and stretchable material systems.[130,134–136] The inherently rigid nature of the inorganic filler particles creates a dramatic compliance mismatch with the soft, stretchable elastomer matrix that leads to internal stress concentrations, delamination, and friction that increase bulk rigidity, reduces extensibility, and results in inelastic stress-strain responses that can limit long term durability at the mesoscale.[136,137] One approach to reduce this compliance mismatch is to use fluid fillers. This has been investigated by Style et al. where ionic liquid inclusions modified the mechanical response of soft elastomers, but electrical properties were not investigated.[138]

2.2 Liquid Metal Embedded Elastomers

In collaboration with my former lab-mates, Drs. Michael Bartlett and Andrew Fassler, I incorporated liquid metal (LM) microdroplets into hyperelastic materials to create all soft matter systems with exceptional electro-elasto properties (Fig. 2.1a-c). The integration of LM microdroplets increases the dielectric constant to over 400 %, displays a low dielectric dissipation factor, and can be stretched to many times their original length (Fig. 2.1d). This approach eliminates the internal compliance mismatch of rigid fillers and thus preserves the mechanics of the host material, offering a unique combination of low mechanical rigidity and a high dielectric constant (Fig. 2.1e). These liquid-metal embedded elastomers (LMEE) can be tailored to match the elastic and rheological properties of soft synthetic materials and biological tissue to enable signal transduction, rigidity tuning, and a rich set of other functionalities for bio-compatible machines (artificial organs) and electronics (artificial skin and nervous tissue).

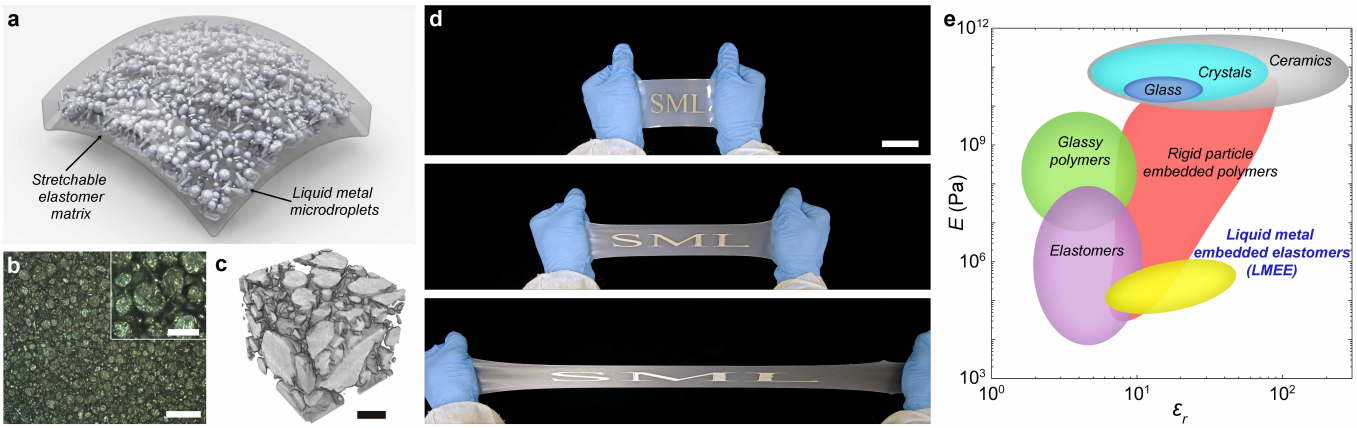

Figure 2.1: Stretchable, high-k dielectrics based on liquid metal embedded elastomers (LMEE). (a) Material schematic showing the dispersion of liquid metal drops in a flexible and stretchable elastomer matrix. (b) Top down optical micrographs of the $\phi = 50\%$ silicone LMEEs at different length scales. Scale bar, 100 μm and inset 25 μm. (c) Nano-CT scan showing the 3D microstructure of the LMEE. Scale bar, 25 μm (d) Photographs demonstrating the patterning and stretchability of the silicone LMEEs from 0% (top) to 250% (middle) to 500% (bottom) strain. Scale bar, 5 cm. (e) Plot of elastic modulus versus dielectric constant for a variety of insulating materials,[133,139] showing the unique combination of low modulus and high dielectric constant of LMEEs.

Composites are prepared by mixing the LM, eutectic Ga-In (EGaIn) alloy (75% Ga - 25% In, by wt.), with uncured liquid silicone (Ecoflex 00-30, Smooth-On) or polyurethane (Vytaflex 30, Smooth-On) at volume loadings (ϕ) of LM from 0 to 50%. The shear mixing is done using a mortar and pestle

until a viscous emulsion is formed and the droplets appear to be less than 30 μm under microscope ($\sim$10 minutes). EGaIn is selected as the LM due to its low melting point (MP = 15°C), high electrical conductivity ($\sigma = 3.4\times10^6 S/m$), low viscosity ($\eta = 2mPa.s$), and low toxicity (compared to Hg).[140,141] Additionally, EGaIn oxidizes in air to form a $\sim$0.5-3 nm thick Ga_2O_3 skin that allows the liquid droplets to be broken apart and dispersed in solution without the need for emulsifying agents. The microstructure of the EGaIn-silicone composite ($\phi = 50\%$) is investigated with top-down optical microscopy (Fig. 2.1b) and through non-destructive 3D X-ray imaging using a nano-CT scanner (Figs. 2.1c and 2.2, Xradia UltraXRM-L200). Together, these two levels of imaging show a disordered but statistically uniform dispersion of droplets and the absence of percolating networks that could result in electrical conductivity or shorting. The microdroplets are also generally ellipsoidal-shaped with dimensions measured through two dimensional particle analysis on the order of $\sim$ 4-15 μm (Figs. 2.3 and 2.4). Because the LMEE composite is a thermoset with a long working time ($\geq$ 30 min), multiple fabrication techniques can be used to pattern liquid metal materials, including 3D printing, soft lithography, laser ablation, or stencil lithography techniques.[142] Thin films can also be prepared and, as an example, a stencil patterned EGaIn-silicone specimen is presented in Fig. 2.1d. For materials with low volume percent EGaIn, a higher concentration sample is prepared first and diluted with the addition of further polymer.

Fig. 2.5, shows the indentation experiment to initiate conductivity in these composites. As shown, even by applying 6250 N/m force the LMEE traces do not become electrically conductive. This extreme resistance of the composite to rupturing and becoming electrically conductive is in contrast to LMEE composites previously studied by Fassler et. al.[137] that were composed of Sylgard 184 as the host matrix and exhibited permanent conductivity after the application of fairly low pressures. This phenomena is expected to be influenced by the stretchability, flexibility and stiffness of the polymer chains. As in Ecoflex 00-30 (Smooth-On), the chains are $\sim$ 5$\times$ more stretchable than Sylgard 184.

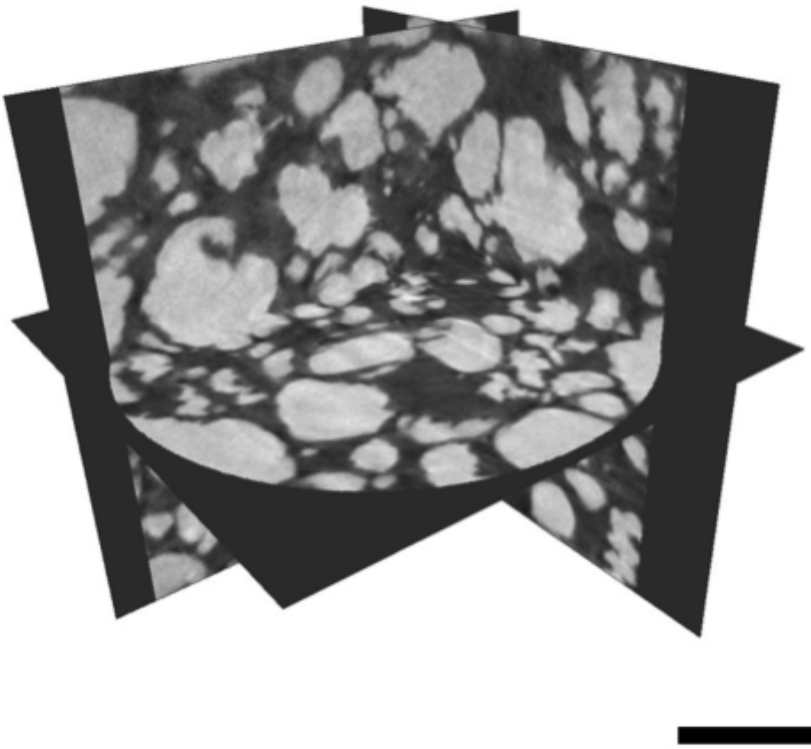

Figure 2.2: 3D microstructure of a silicone LMEE. The image presents an orthoview of a silicone LMEE with $\phi = 50\%$ acquired through 3D X-ray imaging using a nano-CT scanner. The image shows the absence of a percolating network that could result in electrical conductivity or shorting. The scale bar is 20 μm.

2.3 High-k Dielectric Properties

The electrical polarizability of the LMEEs is crucial for their use as soft, stretchable electronic components. Figure 2.6a presents a plot of effective relative permittivity ϵ_r^* versus ϕ for an EGaIn-silicone composite at a frequency of 100 kHz and 0% strain. The plot shows that as the concentration of LM is increased, the effective relative permittivity increases nonlinearly. For the silicone system, the effective relative permittivity of the sample with $\phi = 50\%$ increases to over 400% as compared to the unfilled system over the entire 1 - 200 kHz frequency range (Fig. 2.6b). In order to evaluate the ability of the dielectric to store charge, we measure its dissipation factor (D) for the same range of frequencies (Fig. 2.6c). Also called the loss tangent, D corresponds to the ratio of electrostatic energy dissipated to that stored in the dielectric.[133] For LMEEs, the dissipation factor is measured to be similar to or less than that of the unfilled elastomer ($D < 0.1$) and well within the threshold for

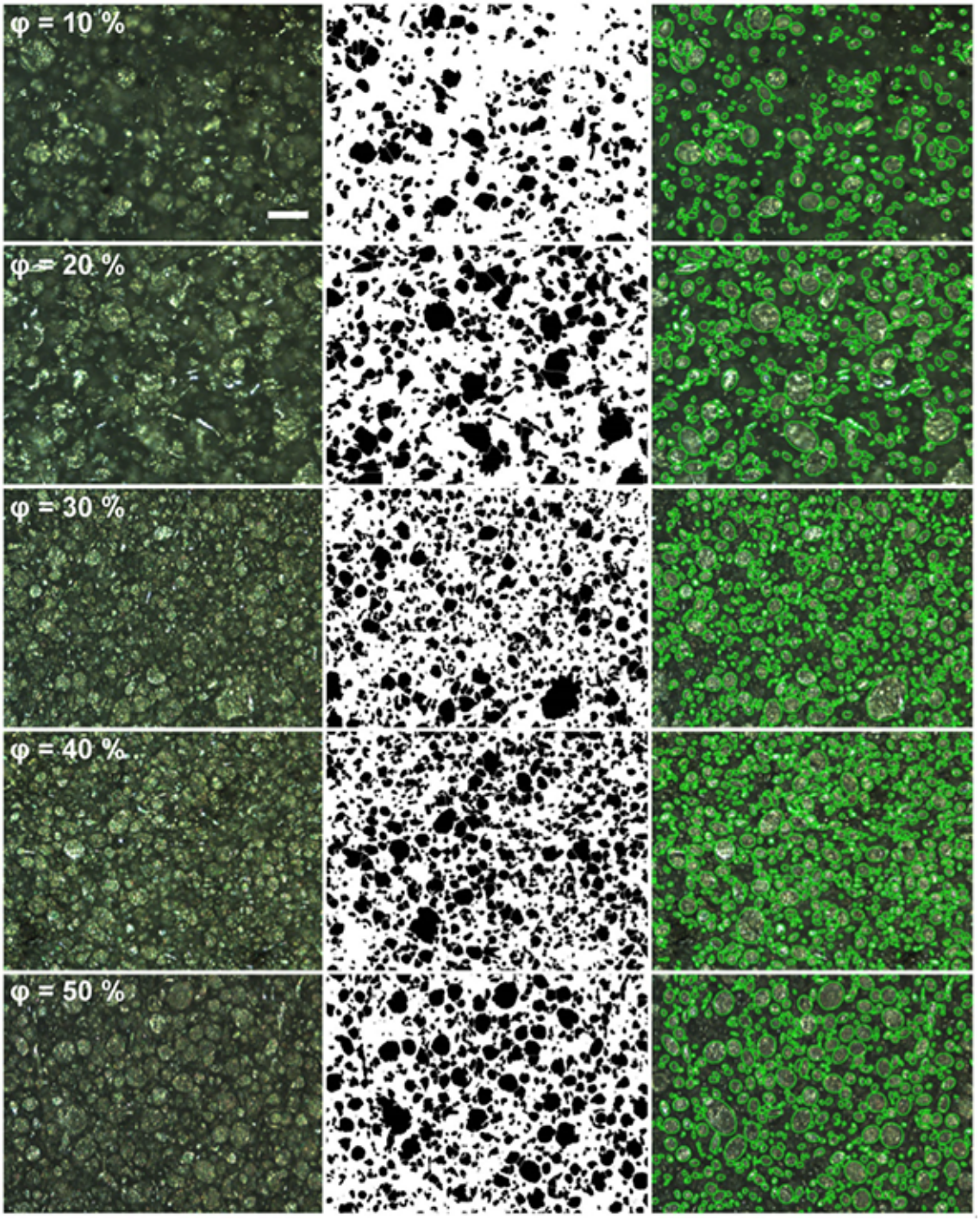

Figure 2.3: Particle analysis of silicone LMEE. Column 1, Optical micrographs of silicone (Ecoflex 00-30) LMEE ranging from ϕ = 10-50%. The scale bar is 50 μm. Column 2, Thresholded image. Column 3, Ellipses fit to the particles in the thresholded image overlaid on the optical micrographs. The size of the analyzed area is 400 $\times$ 300 μm.

dielectric functionality. In contrast, many high-k composites enhanced with conductive particulates (such as Ag, Al, and CB) become lossy and demonstrate large D values due to non-negligible electrical conductivity at volume fractions on the order of 30%.[128]

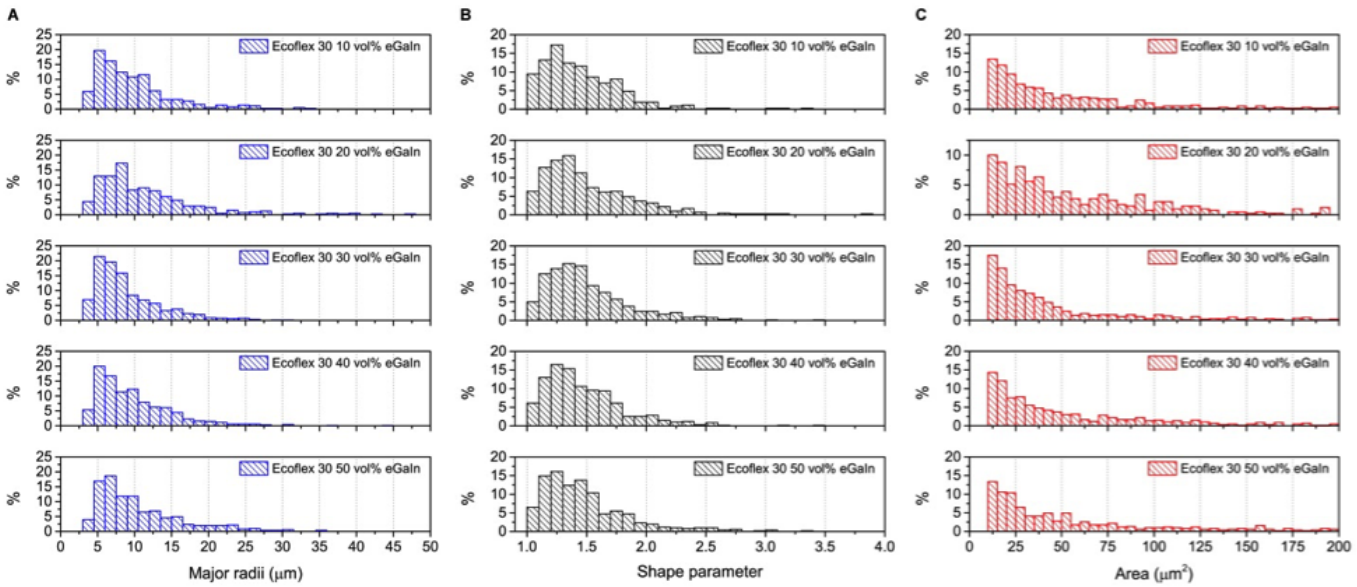

Figure 2.4: Particle analysis histograms of silicone LMEE. (a) Histogram of the percent of analyzed particles versus major radii for different loadings of liquid metal (eGaIn), ranging from $10 \leq \phi \leq 50$. (b) Histogram of the percent of analyzed particles versus the particle shape parameter ($p = r_3/r_1$). (c) Histogram of the percent of analyzed particles versus particle area. The size of the analyzed area is 400×300 μm.

2.4 Effective Medium Theory

To quantitatively understand the increase in relative permittivity, effective medium theory (EMT) can be used to understand the dependency of electro-elasto properties on composition and microstructure. Two of the most common EMT models for a two-phase material with a dilute suspension of spherical particles are the Maxwell-Garnett (MG) and Bruggeman formulations.[143,144] However, from microscopy the liquid metal inclusions have an ellipsoidal shape which is not captured in the MG or Bruggeman models. A more accurate prediction can be obtained by directly solving Maxwell's equations with Green's functions, however this approach is computationally intensive and especially challenging for poly-disperse heterogeneous systems.[143,145] Instead, we use a more general analytic theory by Nan et al.[146] that allows for inclusions with ellipsoidal shapes with principal dimensions $r_1 = r_2$ and r_3. Following Nan et al., the effective relative permittivity ϵ_r^* is predicted by:

$$\epsilon_r^* = \epsilon_{rm} \frac{1 + [\frac{1-L_{11}}{L_{11}}(1 - \langle\cos^2\theta\rangle) + \frac{1-L_{33}}{L_{33}}(\langle\cos^2\theta\rangle)]\phi}{1 - \phi} \tag{2.4.1}$$

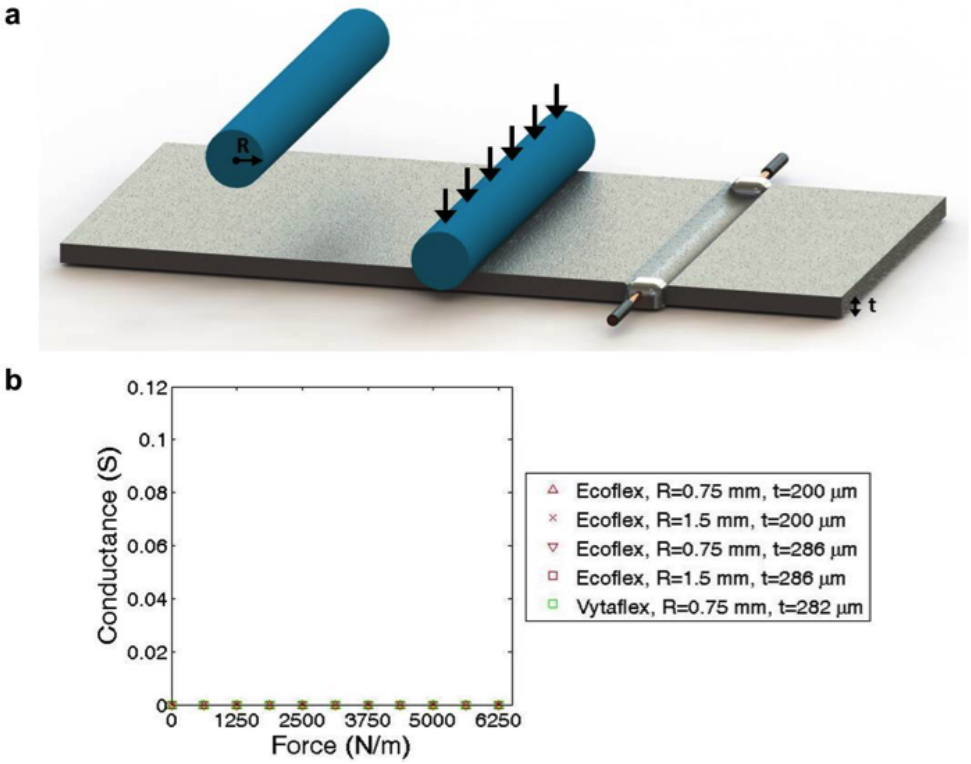

Figure 2.5: Indentation of LMEE and measurement of conductivity (a) Films of LMEE materials with $\phi = 50\%$ were indented with the side of a rigid cylinder to examine if this compression induced any electrical conductivity. EGaIn was applied to the edges of the indented area to improve electrical contact and ensure accurate measurement of resistance across the compressed area. (b) Indentation was not found to induce any conductivity in the silicone (Ecoflex 00-30) or polyurethane (Vytaflex 30) LMEEs, demonstrating their robust dielectric properties.

Here L_{11} and L_{33} are geometrical factors dependent on the particle shape and are given by

$$L_{11} = \frac{p^2}{2(p^2-1)} - \frac{p}{2(p^2-1)^{3/2}} \cosh^{-1} p \quad \text{for } p > 1, \tag{2.4.2}$$

$$L_{33} = 1 - 2L_{11}$$

where ϵ_{rm} is the matrix relative permittivity at $\phi = 0\%$, $p = r_3/r_1$ is the aspect ratio of the ellipsoids, and θ is the angle between the axis along which permittivity is being calculated and the principal axis corresponding to the dimension r_3. The Maxwell-Garnett formula can be recovered from the Nan model when p=1 and $\langle \cos^2 \theta \rangle = 1/3$. For our materials, the average aspect ratio of the LM inclusions measured through particle analysis is $p = 1.49 \pm 0.36$ and $\langle \cos^2 \theta \rangle = 1/3$ for randomly orientated ellipsoids. In Figure 2.6a, the solid curve is the effective relative permittivity, ϵ_r^*, as a function of ϕ as predicted by Equation (2.4.1) and the shaded region represents $\pm$ 1 s.d. to capture

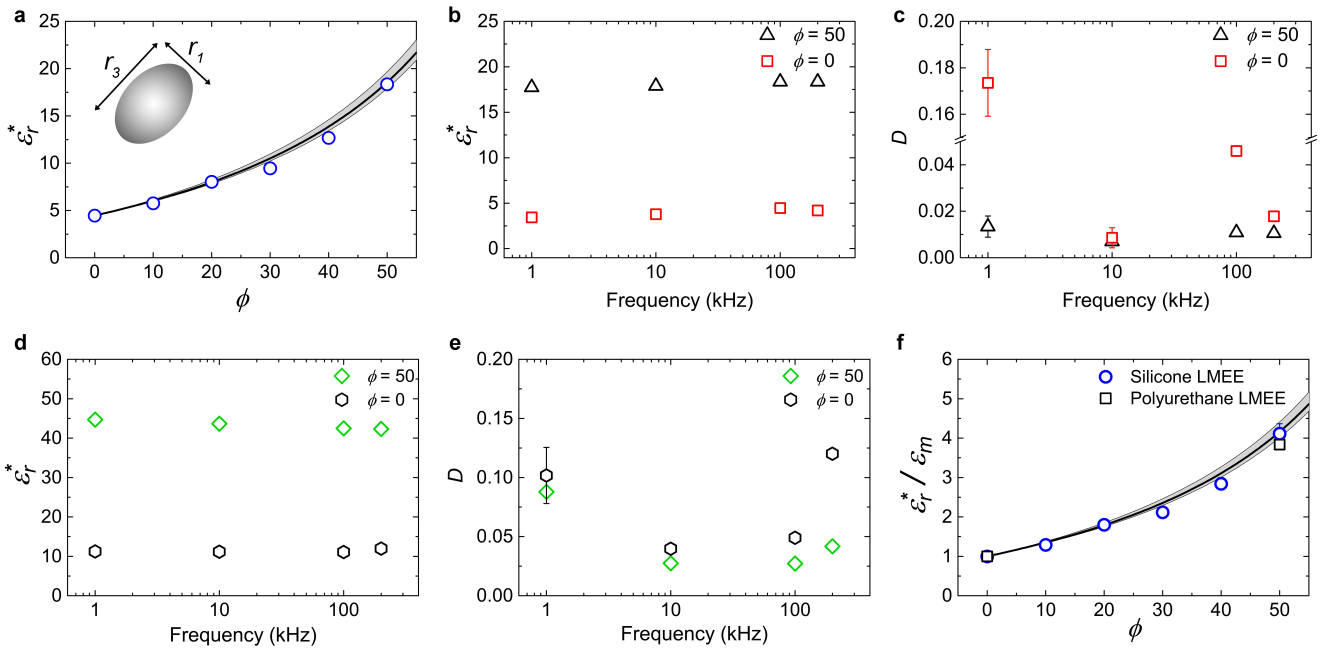

Figure 2.6: Design and evaluation of silicone LMEE dielectric properties. a) Plot of relative permittivity at 100 kHz frequency versus volume fraction loading of liquid metal (ϕ) in the elastomer, the line is the theoretical prediction of Equation (2.4.1) with p = 1.49 ± 0.36 and the shaded region is ±1 s.d. in p. b) Plot of dielectric constant as a function of testing frequency for $\phi = 0\%$ and $\phi = 50\%$ showing an increase of over 400% for the filled system relative to the unfilled system. c) Plot of dielectric dissipation factor as a function of testing frequency showing the low dissipation of the LMEEs. Error bars = ±1 s.d. and error bars smaller than the symbol size are omitted. d) Plot of effective relative permittivity versus testing frequency for polyurethane LMEEs at $\phi = 0\%$ and $\phi = 50\%$. b) Plot of dielectric dissipation factor (D) as a function of frequency for the polyurethane LMEEs, showing low dissipation. c) The dielectric performance of the LMEES is generalized by plotting effective normalized permittivity for both the silicone and polyurethane LMEEs, where the data collapse onto a single line described by Equation 2.4.1 with p = 1.49 ± 0.36. Error bars = ±1 s.d. and error bars smaller than the symbol size are omitted.

the polydispersity in particle aspect ratio. Although Nan et al. is based on multi scattering theory and neglects interparticle interactions, the theoretical prediction is still in very good agreement with the experimental data using only experimentally-measured parameters (i.e. no data fitting). Other potential EMT models for a binary composite with a dilute suspension of spherical particles include the Maxwell-Garnett (MG) and Bruggeman formulations (Fig. 2.7).[143,144,146] In particular, we also find good agreement between our data and the MG model (Fig. 2.7), even though the MG model assumes spherical particles. This suggests that the relatively low aspect ratio ($p = 1.49 \pm 0.36$) of the LM inclusions does not have a large influence on the dielectric response. The Maxwell-Garnett formula can be recovered from the Nan model when p=1 and $\langle \cos^2 \theta \rangle = 1/3$.

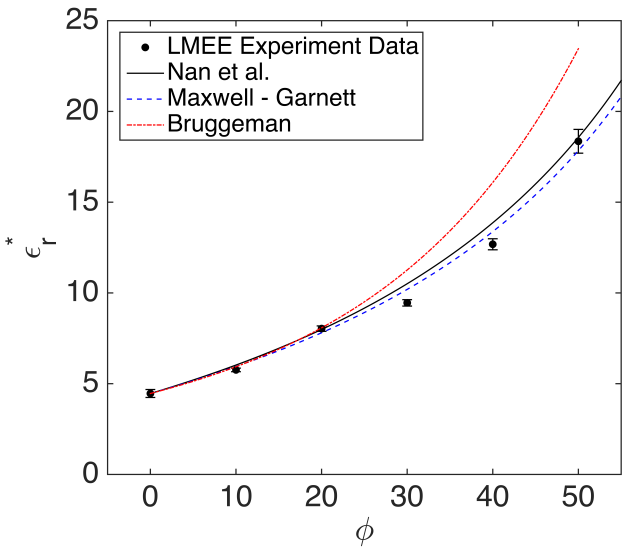

Figure 2.7: Different EMT Models for silicone LMEEs. Plot of effective relative permittivity ϵ_r^*, versus volume fraction of particles ϕ. Symbols with error bars are the silicone LMEE experimental data. Black solid curve is Nan et al.[145] formulation with aspect ratio of 1.49. Blue dashed curve is Maxwell-Garnett (MG), which can be recovered from the Nan model when p=1 and $\langle cos^2\theta \rangle = 1/3$, and the red dotted line curve is Bruggemann effective medium theory with the assumption of $\epsilon_p/\epsilon_m \to \infty$. The Bruggemann formula is known to overpredict the effective permittivity when the ratio of particle to matrix conductivity is assumed to be infinite, which is consistent with our experiments.[143,145]

In addition to exploring LMEEs in silicone elastomers, we also investigated their behavior in polyurethane elastomer matrixes at high volume loadings (ϕ = 50%). Compared to LM-silicone composites, the polyurethane-based LMEEs have a higher elastic modulus (E = 780 kPa) and a lower average strain to break of 182%. Moreover, the dielectric constant of the polyurethane elastomers is found to be considerably greater. Therefore, if extreme strains and moduli on the order of 100-200 kPa are not required, the general strategy developed for silicone LMEEs can be extended to polyurethane elastomers in order to achieve greater permittivity. As seen in Fig. 2.6d the dielectric constant across the frequency range from 1-200 kHz for the polyurethane LMEEs at ϕ = 50% is above 42. Additionally, the dissipation factor is below 0.1 (Fig. 2.6e). To connect the measurements from the silicone elastomers and the polyurethane elastomers and provide a general understanding of LMEEs as dielectric materials, we revisit Equation (2.4.1). When plotting the silicone and urethane LMEEs on a plot of effective normalized permittivity $\epsilon_r^*/\epsilon_{rm}$ versus ϕ at 0% strain, we see that the results collapse on a single line described by the theory (Fig. 2.6f). This clearly shows the applicability of EMT models and the significant influence of LM inclusions on the dielectric constant of hyperelastic media.

2.5 Mechanical Properties

The mechanical behavior of LMEEs is studied under tensile loading for volume ratios (ϕ) ranging from 0 to 50%. Three samples were evaluated at each concentration of LM. Figure 2.8a presents representative stress-strain curves for silicone composites with images of a $\phi = 50$ % LMEE sample stretching to 600% strain. From this data, the influence of stiffness of the liquid inclusions is studied by measuring the elastic modulus in the low strain regime (0 - 10% strain). These tests reveal the mechanical properties of virgin LMEE samples. As I will explain in the next paragraphs, similar to many particle filled elastomers, drastic changes happen to the composite after the first cycle. This phenomena is know as the Mullins effect or stress softening. Figure 2.8b shows that, for the virgin samples, as the amount of liquid metal increases from $\phi = 0$ to 50% the measured elastic modulus increases from 85 kPa to 235 kPa. As the elastomer and LM are virtually incompressible, the composite is expected to maintain an infinite bulk modulus, i.e. $K_e = K_{LM} = \infty \Rightarrow K^* = \infty \; \forall \phi$. Utilizing Eshelby's theory of composites and assuming incompressible elastic inclusions of modulus E_i dispersed in a solid of modulus E, the effective modulus E^* of the composite is expected to be approximately:[134,147]

$$E^* = E\frac{1 + \frac{2}{3}\frac{E_i}{E}}{(\frac{2}{3} - \frac{5\phi}{3})\frac{E_i}{E} + (1 + \frac{5\phi}{3})} \tag{2.5.1}$$

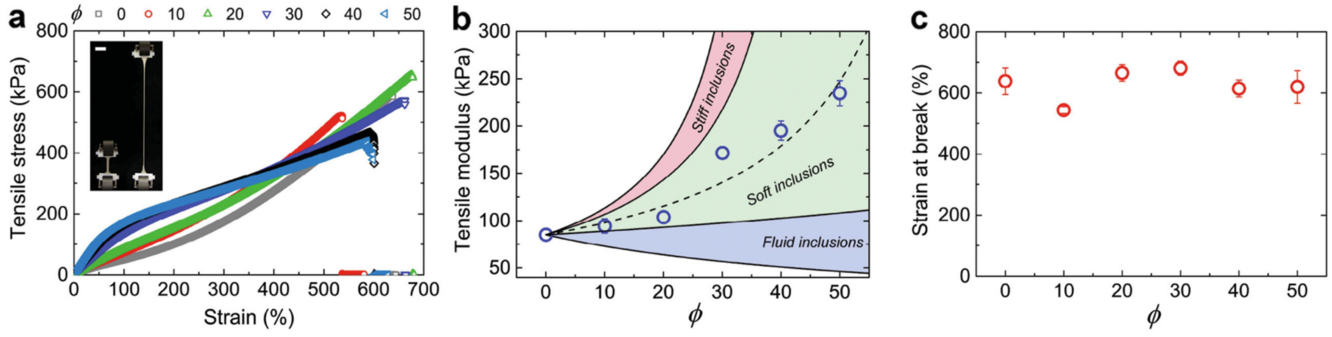

Figure 2.8: Mechanical characterization of LMEEs. (a) Stress versus strain plot for LMEEs from $\phi = 0 - 50\%$ tested until failure. The image shows the $\phi = 50\%$ at 0% and 600% strain, scale bar, 25 mm (b) Plot of elastic modulus (measured to 10% strain) as a function of the volume fraction loading of liquid metal (ϕ), the dashed line is the prediction of Equation 2.5.1 showing the increase in modulus due to the liquid metal inclusions ($E_i = 320$ kPa). (c) Strain at break for the LMEEs as a function of ϕ. Error bars = $\pm$ 1 s.d. and error bars smaller than symbol size are omitted.

Equation 2.5.1 is plotted as a function of ϕ in Figure 2.8b for different regimes of inclusion

stiffness. Three regimes are represented: stiff inclusions (1 MPa < E_i <1 TPa), soft inclusions (129 kPa < E_i < 1 MPa) and liquid inclusions with surface tension (0 kPa < E_i <129 kPa). The limit E_i = 129 kPa is based on recent observations by Style et al.[138] that liquid inclusions can stiffen solids and exhibit an effective modulus $E_i = E \times 24\alpha/(10 + 9\alpha)$, where E is the modulus of the surrounding elastomer, $\alpha = \gamma/ER$, γ is the surface tension of the liquid droplet, and R is the droplet diameter. For values of $\gamma = 620\, mJ/m^2$, E = 85 kPa, R = 5.0 μm, it follows that surface tension and surface stress can effectively make the liquid act as an elastic inclusion with modulus E_i = 129 kPa. However, as observed in Fig. 3b, the LMEE composites have stiffnesses above those predicted by this estimate but are well within the regime for soft inclusion. Specifically, good agreement between the experimental data and Equation 2.5.1 is found with an inclusion modulus value of 320 kPa. The larger inclusion modulus value used for fitting could be attributed to both the theory assuming that the particles are non-interacting, which is likely violated at higher volume fractions, and that the oxide skin on the LM drops can also act to stiffen the inclusions. Despite the stiffening effect in first cycle, the composites are similar in modulus to soft synthetic materials and biological tissue.[122,148] These LMEE composites are also able to undergo significant strain. Fig. 2.8c shows that the LMEE composites are able to stretch to strains on the order of 600%, similar to that of the unfilled elastomer.

2.5.1 Mullins Effect

LM-embedded elastomer show stress softening after initial loading cycle. This effect which is called the Mullins effect,[148,149] is a typical behavior of particle filled elastomer composites (Figure 2.9a) in which big energy dissipation occurs in the first cycle of a freshly prepared (virgin) sample, and vanishes with subsequent loading (unless the sample is stretched beyond its previous max strain). The composite exhibits very little hysteresis (Fig. 2.9a), after the first cycle, when comparing the loading and unloading curves. This suggests negligible internal friction and losses due to viscoelasticity. Hence, after cycling and training of LMEEs, the 10% tensile modulus remains less than 90 kPa (Figure 2.9b and c). The modest increase in elastic modulus (< 20%) for the LMEE composites can be attributed to surface tension at the liquid-solid interface.

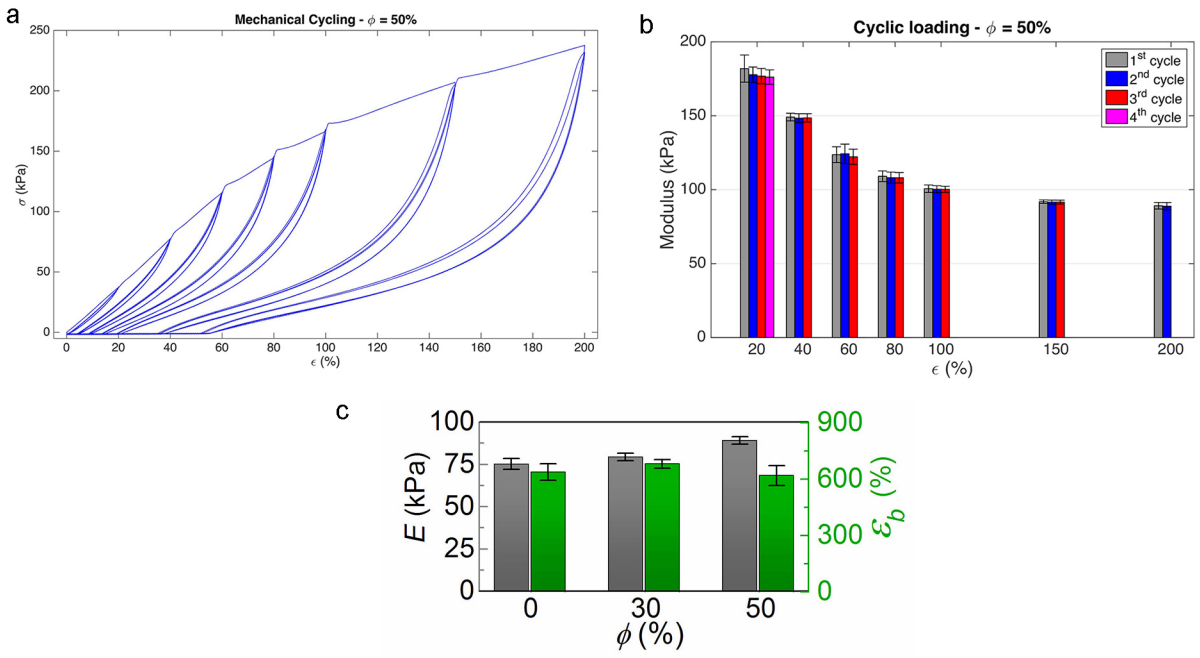

Figure 2.9: Mechanical cyclic tests of LMEE. a) Stress vs. strain curves for 50% volume ratio of LM. b) 10% elastic modulus after each strain step. c) converged values of 10% elastic modulus after cyclic test until 200% strain, with strain at break for $\phi = 0\%, 30\%$, and 50%.

2.5.2 High Cyclic Loading

The mechanical behavior of the composite at high cycles is crucial for many applications in electronic devices and wearable computing. Due to the high vibrational state, any material being used would undergo millions of cycles over the lifetime of the device. In order to understand long term behavior of LMEE, we are using a jig-saw mechanical test setup developed by my lab-mate Eric Markvicka, that can provide a low cost, high frequency and high cyclic tensile test. A sample of LMEE with $\phi = 50\%$, initial length of $L_0 = 51mm$ and thickness of $t = 2.6mm$, is stretched between 76% and 135% of strain, with frequency of 5Hz, for 1 million cycles. The stress vs strain plot for cycles 1, 1k and 1M is plotted in Fig 2.10. According to the preliminary results (Fig. 2.10), the maximum stress doesn't significantly change after 1M cycling. However, an increase in plastic deformation can be observed in the high cycles (1M), as the magnitude of stress goes to negative values.

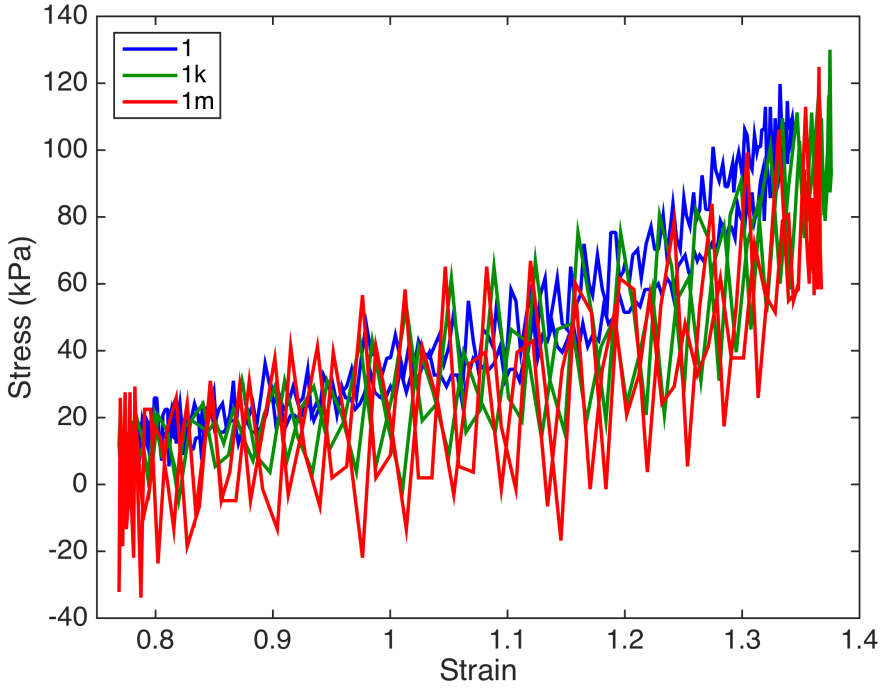

Figure 2.10: Stress vs strain curves of high cyclic mechanical tensile test for LMEE with $\phi = 50\%$. Blue is the first cycle, green is the cycle number 1000, and red is cycle number 1M.

2.6 Electro-Elasto Properties

The electrical response to mechanical deformation is a significant parameter for stretchable dielectrics. Fig. 2.11a and b presents results for the electrical permittivity and electromechanical coupling of EGaIn-silicone composites ($\phi = 50\%$). Measurements are performed on a stretchable parallel-plate capacitor composed of a LMEE dielectric and EGaIn electrodes sealed in an additional layer of silicone (Fig. 2.11a inset). The normalized capacitance, C/C_0, where C_0 is measured at 0% strain, increases under tensile loading until the dielectric fails at over 700% strain. For a parallel plate capacitor the initial capacitance can be calculated by $C_0 = \epsilon_r \epsilon_0 \frac{A_0}{t_0}$, where $\epsilon_0 = 8.85 \times 10^{-12}\ Fm^{-1}$ is the vacuum permittivity, and A_0 and t_0 are the initial planar area and thickness, respectively. Under the assumption of incompressibility the dielectric constant of the LMEEs during stretching from an initial length L_0 to the instantaneous length L can be calculated as:

$$\epsilon_r = \frac{C t_0}{\epsilon_0 A_0} \frac{1}{\lambda}, \tag{2.6.1}$$

where $\lambda = L/L_0$ is the extension ratio. Using Equation 2.6.1, the dielectric constant is plotted in Fig. 2.11a. It is observed that as the sample is loaded in tension, the capacitance increases by a factor of over 4.5 while the dielectric constant decreases from 18 to 9 when stretched from 0% to 700% strain. To further study the durability of the LMEEs as dielectric materials we performed cyclic testing experiments to 100% strain under tensile loading over 100 cycles (Fig. 2.11b). During the experiments the capacitance increased slightly at both 0 and 100% strain during the first 10 cycles, but then stayed constant until the test is completed at 100 cycles. The ability to undergo significant strain over 100 cycles without degradation of the electrical or mechanical properties further demonstrates LMEEs as stretchable dielectric materials.

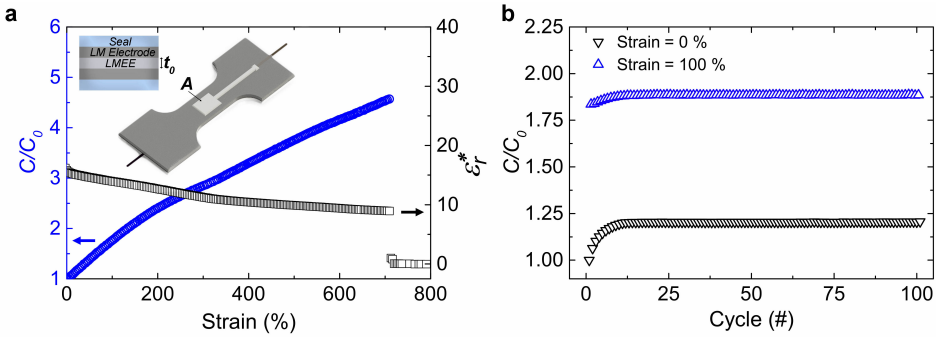

Figure 2.11: a) Electromechanical coupling strain to break curve showing the (left axis, blue circles) increase of capacitance (C) relative to the initial capacitance (C_0) and (right axis, black squares) dielectric constant calculated from Equation (2.6.1) as a function of stretch. b) Cyclic testing of the LMEE to 100% strain over 100 cycles.

2.7 Conclusion

Because of their robust mechanical properties and ease of fabrication, the LMEE composites introduced here are an excellent model system for examining the electro-elasticity of more general classes of soft-matter heterogeneous materials. From an application's perspective, these materials provide opportunities for integration into soft electronics including sensors and soft energy harvesting devices. In particular, hyperelastic capacitive strain sensors would be able to measure stretches well above double their initial length with significantly improved sensitivity.

In this chapter, I introduced a novel LM-embedded elastomer composite. An enhancement of

about 450% in dielectric constant of the composite over the base elastomer is observed. Due to similarities between field equations of relative permittivity and thermal conductivity, I expect to see similar enhancement in the heat conduction of LMEEs. Hence, in the next chapter I will look into measuring and characterizing the thermal conductivity of LMEE composites and in particular will take advantage of the ability of LMs to become highly elongated inside the elastomer. Subsequently, LMEEs with combination of high thermal conductivity and high compliance will be implemented in applications related to wearable computing and soft robotics.

Chapter 3

High Thermal Conductivity in LMEEs with Elongated Liquid Metal Inclusions

Reference:

N. Kazem*, M. D. Bartlett*, M. J. Powell-Palm*, X. Huang, W. Sun, J. A. Malen, and C. Majidi, "*High Thermal Conductivity in Soft Elastomers With Elongated Liquid Metal Inclusions*", Proceedings of the National Academy of Science, 2017.

3.1 Introduction

Materials with high thermal conductivity are typically rigid and elastically incompatible with soft and mechanically deformable systems.[17,150–154] In the general case of nonmetallic and electrically insulating solids, this limitation arises from kinetic theory and the Newton-Laplace equation, which imply that thermal conductivity (k) will increase with a material's elastic modulus (E) according to the approximation $k \approx (E/\rho)^{1/2}(C_V l/3)$, where C_V is the volumetric heat capacity, l is the average mean free path of phonons, and ρ is the density.[155,156] For polymers like polyethylene, thermal conductivity can be enhanced through macromolecular chain alignment (from k $\approx$ 0.3 W/mK to 100 W/mK), but this also leads to a dramatic increase in elastic modulus from $\sim$1 GPa to 200 GPa.[157] Likewise, glassy polymer blends have been engineered to increase thermal conductivity through interchain hydrogen bonding[17], and relatively higher thermal conductivity has been observed in amorphous polythiophene (k $\sim$ 4.4 W/mK)[150], but the high elastic modulus (E $\sim$ 3 GPa) and low strain at failure (<5% strain) of films make them unsuitable for soft functional materials.[151]

To overcome this fundamental tradeoff with thermal transport in soft materials, attempts have been made to engineer composites with various fillers,[158] including metals,[159,160] ceramics,[161] carbon fibers,[162] and nanomaterials such as carbon nanotubes and graphene.[152,163,164] Anisotropic thermal conductivity can arise in composite systems by using 1D fillers such as carbon fibers where thermal transport preferentially occurs along the major dimension of the filler.[162] Thermal anisotropy can also be induced in polymeric materials during drawing processes that increase chain alignment.[165] Although these composites exhibit increased thermal conductivity, they typically use rigid fillers that result in mechanically stiff materials that cannot support stretchable functionality[152,154], and in the case of carbon-based fillers, become electrically conductive even at low-volume loadings, which can

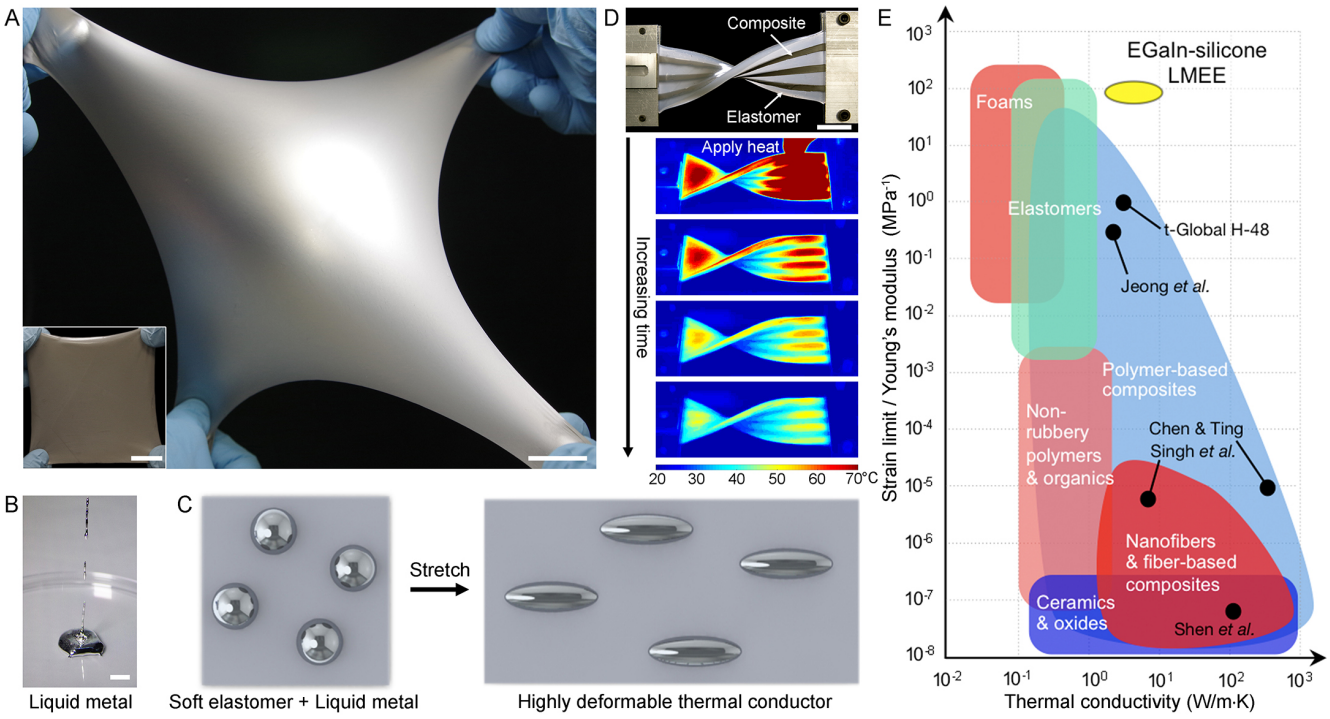

Figure 3.1: Soft, thermally conductive composite. a) Highly deformable LMEE. (scale bars, 25 mm.) b) EGaIn alloy is liquid at room temperature and shows fluid characteristics as demonstrated by falling droplets. (Scale bar, 10mm.) c) Schematic illustration of the LMEE composite where LM microdoplets are dispersed in an elastomer matrix and, upon deformation, the LM inclusions and elastomer elongate in the direction of stretching. d) Alternating strips of LMEE and unfilled elastomer are heated with a heat gun, and the IR photo time sequence shows the LMEE dissipating heat more rapidly than the elastomer (images correspond to t = 0, 5, 10, and 15 s after the heat source is removed). (Scale bar, 25mm.) e) The $\phi = 50\%$ LMEE composites described here occupy a unique region of the material properties space when comparing thermal conductivity with the ratio of strain limit to Young's modulus. (Data points are from refs.[150,157,159,162])

interfere with functionality.[166] To date, the combination of low elastic modulus on the order of biological tissue, large mechanical deformability, and high thermal conductivity remains elusive.

To examine thermal conductivity of LMEEs, I performed characterization studies in collaboration with Dr. Michael Bartlett (Majidi Group) and Matt Powell-Palm (Malen Group). We showed that LMEE composites consisting of elongated liquid metal (LM) microdroplets dispersed in a highly deformable silicone elastomer (Fig. 3.1 a-d) exhibit an unprecedented combination of high thermal conductivity (4.7 ± 0.2 W/mK under stress-free conditions; 9.8 ± 0.8 W/mK at 400% strain) with a low modulus (89 ± 2 kPa after 200% prestrain) and high strain limit (>600%). This approach overcomes the Newton-Laplace scaling because the inclusions have a thermal conductivity that is dominated by electrons, rather than phonons, and can deform with the surrounding matrix

to support strain and thermal-mechanical coupling. A subsequent effort by another group attempted to show enhanced thermal conductivity with a polydisperse suspensions of irregularly shaped LM inclusions[160]. Although an enhanced thermal conductivity of 2.2 W/mK was measured at high LM volume fraction (66% by vol.; 92.5% by weight), these samples exhibited an increased stiffness (Young's modulus increased from 0.65 MPa to 3.3 MPa) and reduced stretchability (strain limit decreased from 150 to 50%), which limits the ability to elongate LM droplets in situ. Comparing previous results with the exceptional performance reported here (Fig. 3.1e) highlights the critical importance of LM microstructure (and not just material composition) in enabling elastomers to exhibit metal-like thermal conductivity without altering their natural elasticity.

As shown in Fig. 3.1d, stretched and twisted strips of LMEE exhibit rapid thermal dissipation compared to adjacent strips of unfilled elastomer subject to the same initial heating. As compared to previous attempts with LM-filled elastomers[160], we have discovered that strain creates thermally conductive pathways through the in-situ elongation of the deformable liquid inclusions, which significantly enhances thermal conductivity in the stretching direction. For permanent (stress-free) and strain-controlled elongation of the LM inclusions, this enhanced thermal conductivity is nearly $25-50\times$ greater than the unfilled elastomer (0.20 ± 0.01 W/mK) and approaches the limit for the parallel rule of mixtures of an EGaIn-silicone composition[108] without the aid of percolating networks. Referring to Fig. 3.1e, the exceptional combination of thermal conductivity, low elastic modulus, and high strain limit allows the LMEE composites to occupy an uncharted region of the material properties space.

3.2 Hotwire Method

Thermal conductivity is measured using the transient hotwire (THW) method in which an embedded wire simultaneously acts as a resistive heat source and thermometer that measures the change in temperature (ΔT) as a function of time (t), which are related to thermal conductivity through the cylindrical heat diffusion equation: $k = q/4\pi\xi$.[167] Here, q is the volumetric heating of the wire per unit length, which is calculated using known current and resistance values and $\xi = d(\Delta T)/d[ln(t)]$.

3.2.1 Unstrained measurements

Test samples are prepared by first suspending a platinum wire (D = 25 μm, l = 40 mm) in a 3D-printed container with dimensions of 40 mm × 7mm × 7 mm. Next, uncured composite is poured around the wire to ensure conformal contact. The composite is cured with the Pt wire inside an oven at 50°C for 16 h. The electrical resistance across the wire is measured before and after curing to ensure that there is no mechanical interference in the wire due to thermal expansion or contraction. To administer the tests, each sample is connected to a Keithley 2700 Digital Multimeter and a Keithley 6221 DC/AC Current Source in a four-point measurement configuration. A Heavyside current input of I = 30 mA is applied, and 50 voltage values (V) are recorded over 0.9 s. With this voltage data and a known current, the resistance (R) is determined as a function of time following Ohm's Law: $R(t) = V(t)/I$. This is used to calculate the change in temperature $\Delta T(t) = [R(t)/R_0 - 1]/\beta$ and the volumetric heating of the wire per unit length $q = I^2 R_0/l$. Here, $R_0 = R(0)$ is the initial resistance of the wire, $\beta = 3.75 \times 10^{-3} K^{-1}$ is the coefficient of thermoresistance of platinum, and l is the length of the wire. Next, we plot ΔT versus time (t) and fit the curves using the following three-parameter model: $\Delta T = b_1 ln(t - b_2) + b_3$, where the constants b_1, b_2, and b_3 are the fitting parameters. The fit is performed in MATLAB R2015a (The Mathworks, Inc.) using a nonlinear regression "nlinfit" algorithm. The fitted coefficient b_1 corresponds to $\xi = d(\Delta T)/d[ln(t)]$, and the thermal conductivity is calculated as $k = q/4\pi\xi$. Our data acquisition has an arbitrary delay relative to initiation of the Heavyside function, and b_2 and b_3 represent the delay time and resultant temperature rise that occur during that period. The thermal conductivities measured for water and glycerol at room temperature are 0.60 ± 0.07 and 0.33 ± 0.02, respectively, and are in good agreement with reference data. The thermal conductivity is reported by taking the average k across all runs, and the error represents ±1 SD. Fig. 3.2 shows the ΔT versus t plots for these two validation measurements, where the data symbols represent the average and the shaded areas correspond to the SD for 50 measurements. Average ΔT vs. time for LMEE samples of varied LM volume fraction is shown in Fig. 3.3. Each measurement is repeated 100 times for each volume fraction of LM composite. The data symbols represent the average, and the shaded areas correspond to the SD for 100 measurements at each volume fraction.

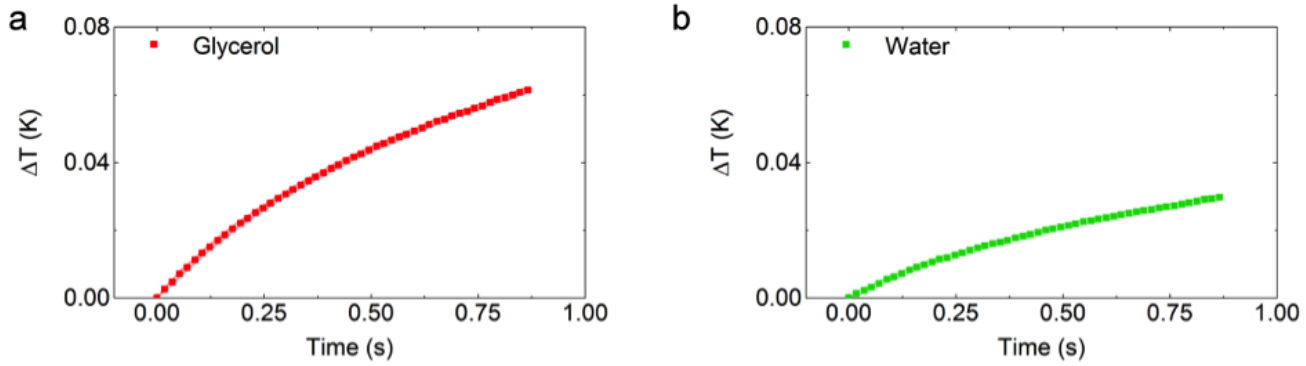

Figure 3.2: Change in temperature (ΔT) versus time for a) glycerol and b) water. Data symbols represent the average and the shaded areas correspond to the standard deviation for the 50 measurements at each condition.

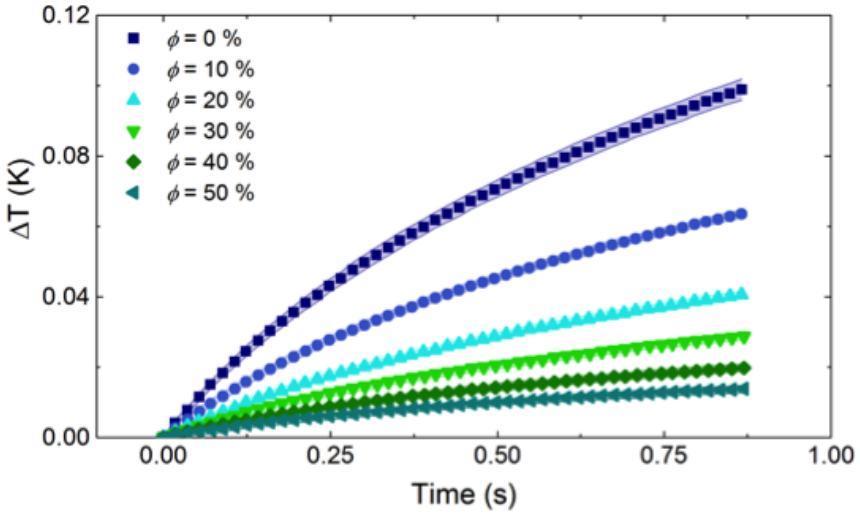

Figure 3.3: Change in temperature (ΔT) versus time for LMEE with $\Phi = 0 - 50\%$ volume fraction. Data symbols represent the average and the shaded areas correspond to the standard deviation for the 100 measurements for each condition.

3.2.2 Thermal-mechanical testing

The thermal conductivity as a function of stretch is measured with two Pt wire probes orientated parallel and perpendicular to the primary stretching direction (Fig. 3.6b). The probes are laminated between two layers of material, which each have dimensions of 60 mm wide, 40 mm long, and ~5 mm thick. Tests are performed with composites of $\phi = 0\%$, 30%, and 50% that are strained ($\epsilon = \Delta L/L0$) to 400% in 100% strain increments. A current of 30 mA is used for $\phi = 0\%$ and 30% (with the

exception $\phi = 30\%$ at 400% strain, where a 60mA current is applied to improve signal to noise), and 100mA is used for $\phi = 50\%$. At each strain increment, five measurements are taken on each wire at 2-min intervals. After each strain increment, the two layers of material are delaminated, freeing the wire probes to prevent damage during stretching, then stretched equally in both directions using linear actuators. At the next position, the layers of composite are relaminated around the wires, with a clamping force applied to ensure conformal contact. Fig. 3.4 demonstrates the good agreement with the three-parameter fit for the $\phi = 50\%$ LMEE measured on the axial wire at $\epsilon = 0\%$ and 400%. The symbols are the data points for each run, and the lines represent the corresponding three-parameter fit. Fig. 3.5 presents ΔT vs. t curves for the axial and transverse wires in the $\phi = 0\%$, 30%, and 50% LMEE. At $\epsilon = 0\%$, the measured thermal conductivity for both the laminated parallel and transverse sensors are in good agreement with the embedded sensors described in unstrained measurements, proving that the wire is in intimate contact with the LMEE samples.

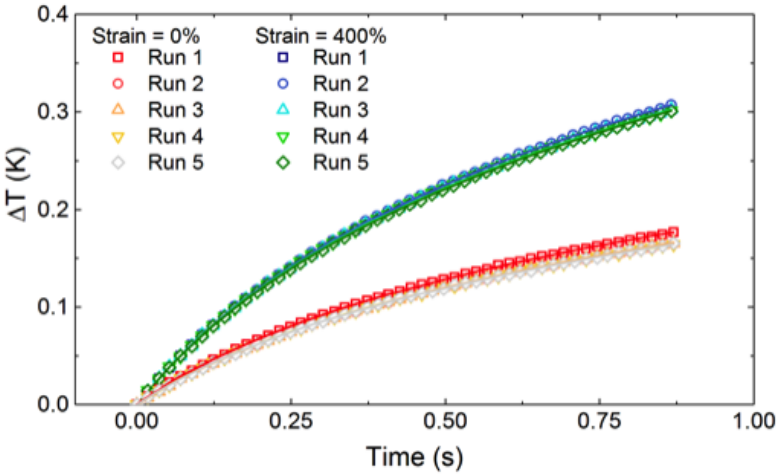

Figure 3.4: ΔT versus time for $\Phi = 50\%$ for the axial wire at $\epsilon = 0\%$ and 400%, which demonstrates good agreement with the three parameter fit explained in the supplementary information. The symbols are the data points for each run and the lines represent the corresponding three parameter fit.

3.3 Results

Experimental measurements are presented in Fig. 3.6a, which show that as LM volume fraction (ϕ) increases thermal conductivity increases. These values are in good agreement with theoretical

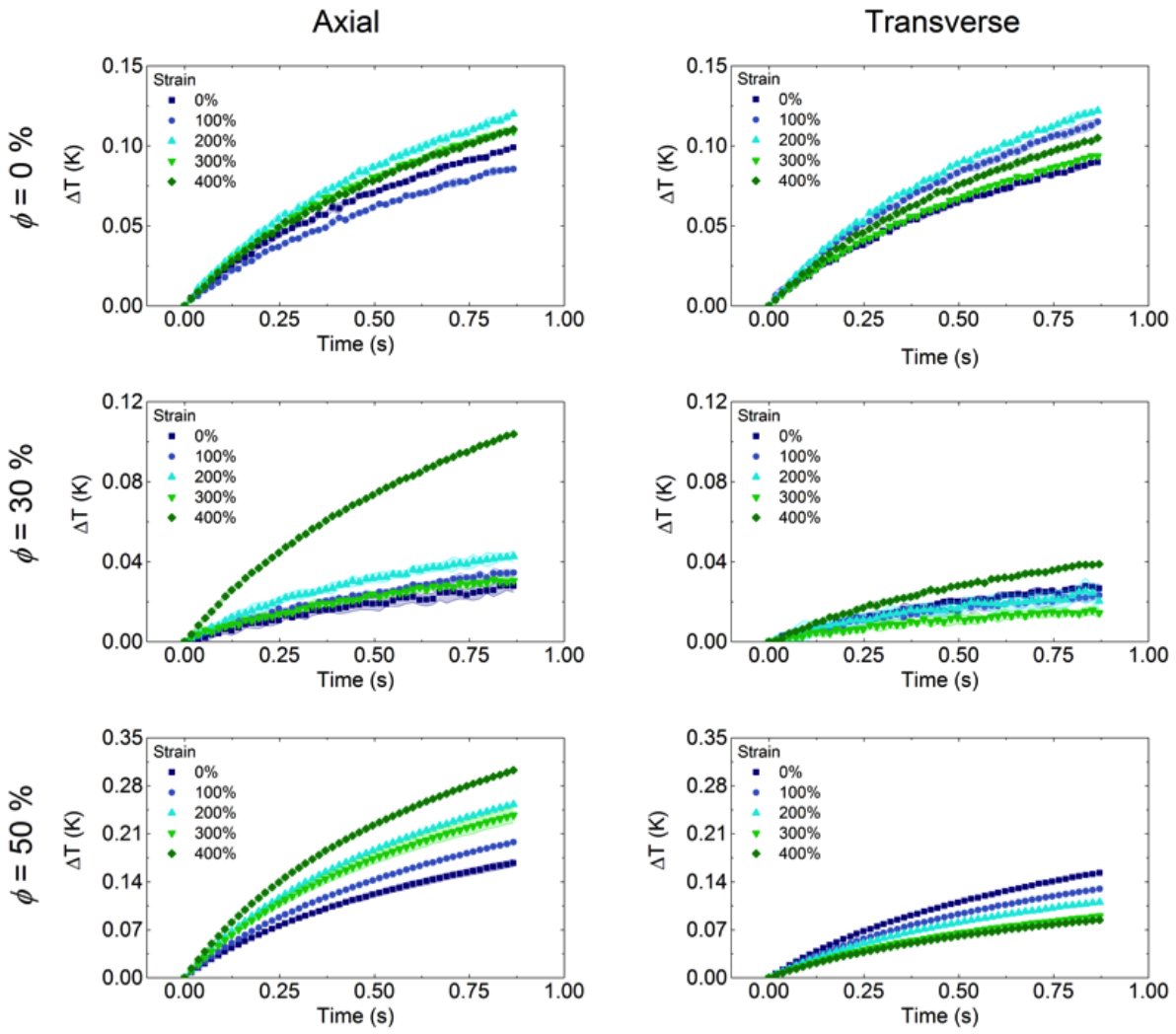

Figure 3.5: ΔT versus time of $\phi = 0\%$, 30% and 50% for the axial and transverse wire up to 400% strain in 100% strain steps. Data symbols represent the average and the shaded areas correspond to the standard deviation for the 5 measurements for each condition. Hotwire lengths can vary between tests resulting in a non-monotonic temperature change across strain steps. This is accounted for by q, the volumetric heating of the wire per unit length, when calculating thermal conductivity.

predictions obtained from the Bruggeman effective medium theory (EMT) formulation[143] (see Sec. 3.4) for a uniform dispersion of spherical EGaIn inclusions (k = 26.4 W/mK[108]) in a silicone matrix (k = 0.20 W/mK).

We further configure the THW method to enable directional measurements of thermal conductivity upon deformation by laminating LMEE strips around wires that are parallel (axial) and perpendicular (transverse) to stretch, as shown in Fig. 3.6b. Ellipsoidal heat spreading yields effective anisotropic thermal conductivities in the axial and transverse directions that can be transformed to measure the orthotropic (k_x, k_y, k_z) bulk values.[168,169] This configuration enables examination of

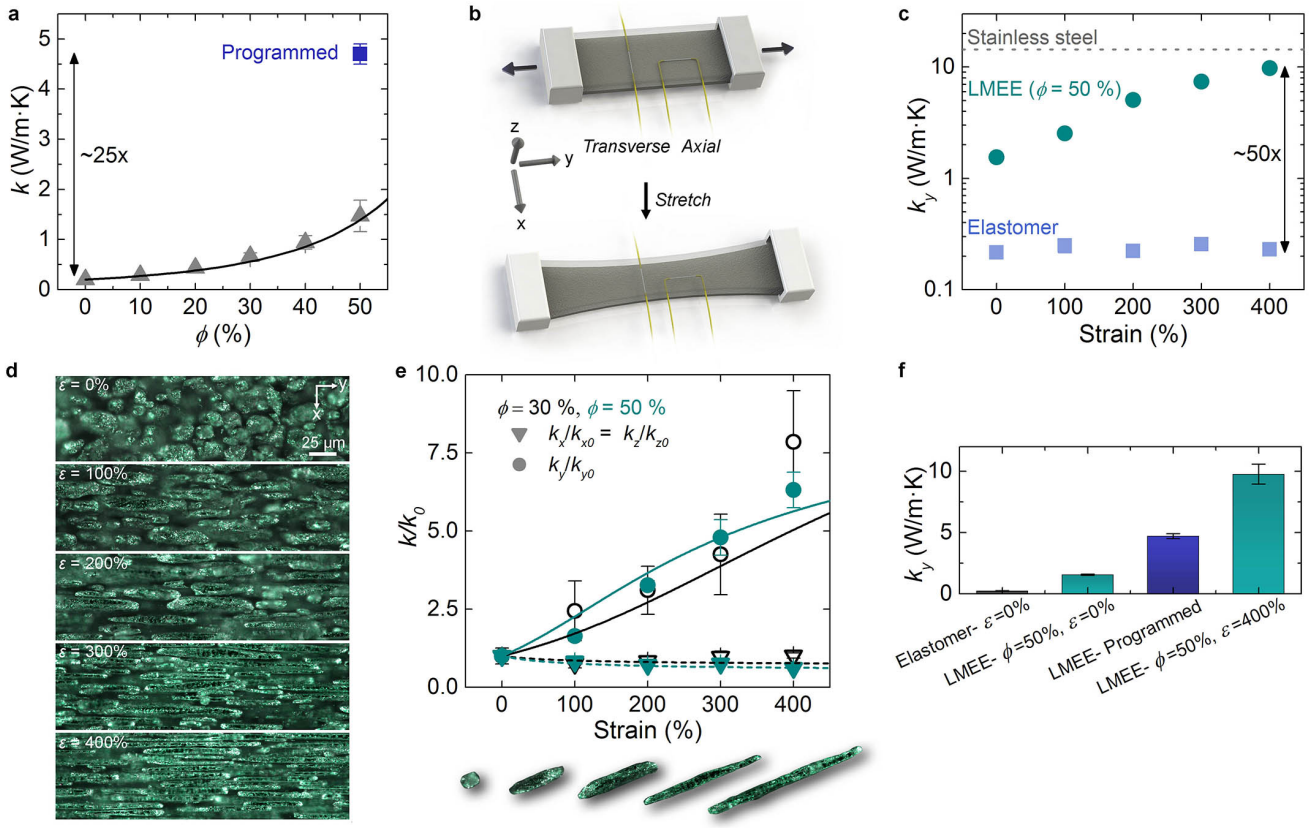

Figure 3.6: Thermal-mechanical behavior of the LMEE composite. a) Thermal conductivity versus LM volume fraction (ϕ) in the stress-free state. The programmed sample refers to a composite that has been stretched to 600% strain and then relaxed to an unloaded state. Here the symbols are the experimental measurements, and the solid curve represents the theoretical prediction from the Bruggeman EMT formulation (n = 100 volume fraction dependence, n = 5 programmed samples). b) Schematic of the THW method to measure anisotropic thermal conductivity under deformation. c) Plot of thermal conductivity in the stretch direction versus strain for the elastomer and the LMEE composites. Upon stretching, the LMEE approaches the thermal conductivity of stainless steel and is 50× greater than the unfilled elastomer. (n = 5). d) Optical micrographs of the 30% LMEE microstructure during stretching, with the images corresponding to 0 to 400% strain in 100% increments (from top to bottom). e) Normalized thermal conductivity as a function of strain (black open symbols are $\phi = 30\%$, and cyan closed symbols are $\phi = 50\%$; n = 5). The solid line represents the predicted behavior for the y direction, and the dashed line is the prediction for the x and z direction from our model. The images are representative images of the LM inclusions during the deformation process. f) Thermal conductivity comparison for different LM volume fractions (ϕ) and stress states (n = 5).

the thermal-mechanical coupling between thermal conductivity and deformation. We find that upon stretching the unfilled ($\phi = 0\%$) homogenous elastomer, the thermal conductivity in the direction of stretch ($k_y \sim 0.20$ W/mK) remains largely unchanged (Figure 3.6c). However, when stretching the $\phi = 50\%$ LMEE, the thermal conductivity in the longitudinal direction (k_y) dramatically increases and reaches a value of 9.8 ± 0.8 W/mK at 400% strain. This represents an increase of ~50× relative

to the unfilled material and a value that approaches the thermal conductivity of some metals like bismuth and stainless steel. Furthermore, we can "program" the material to achieve permanently elongated LM inclusions in a stress-free state by stretching a virgin sample of LMEE to 600% strain and then unloading to zero stress. An unrecoverable plastic strain of 210% is induced, enabling elongated inclusions in an un-loaded (stress-free) state (Fig. 3.7). As shown in Figure 3.6a, thermal conductivity of the programmed LMEE sample in the longitudinal direction (k_y) is 4.7 ± 0.2 W/mK, which is ~25× greater than that of the base elastomer (Figure 3.6f). It is important to note that when unstrained, both the $\phi = 0$ and 50% samples exhibit values of k that are typically observed in other polymeric composites.[163,170]

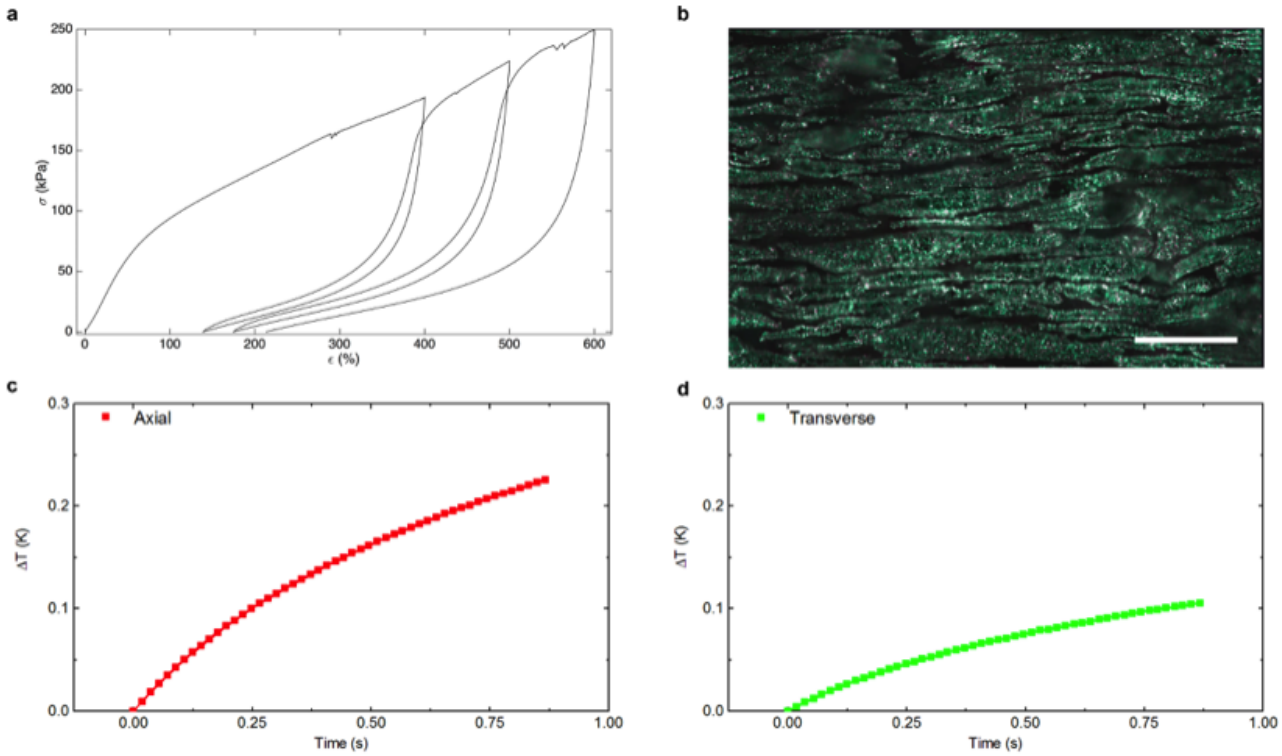

Figure 3.7: Programmed material. a) Stress vs strain curve for fabrication of shape programmable LMEE with 50% volume ration of LM. b) Optical micrograph of programmed LMEE with 50% volume ratio of liquid metal. Scale bar is 50 μm. Change in temperature (ΔT) versus time for c), axial and d), transverse wire for the programmed LMEE samples.

Such an unprecedented enhancement in k arises from a unique thermal-mechanical coupling in which the deformable LM inclusions elongate into needle-like microstructures along the pre-strained or mechanically loaded direction to create enhanced thermally conductive pathways (Figure 3.6e). This is further demonstrated in Figure 3.6d, in which compositions with $\phi = 30\%$ and 50% EGaIn

(by vol.) are subject to strains ranging from 0% to 400% in increments of 100%. As shown, the thermal conductivity in the y (stretching) direction increases by greater than a factor of five beyond 300% strain. To theoretically capture this behavior we create an EMT model (see chapter 3.4) based on the Bruggeman formulation to explain the relative increase in directional thermal conductivity as a function of axial strain (ϵ). As seen in Figure 3.6e, we find good agreement between the experimentally-measured values (markers) and our theoretical predictions (curves), which capture the large increase in thermal conductivity in the stretching direction (k_y) and the slight decrease in the orthogonal directions (k_z, k_x). The agreement with theory is achieved without data fitting and supports the claim that the observed anisotropic thermal-mechanical response is controlled by the directional change in aspect ratio of the LM inclusions.

Strain-dependent thermal conductivity is also evaluated at elevated (60 $\pm$ 3C) and reduced (0 $\pm$ 3 C) temperatures. A thermocouple embedded in the LMEE is used to monitor temperature, and measurements are conducted when a variance of no more than 0.1 °C is observed over a 1-min period. Thermal conductivity measurements are then performed as described above. In between each strain increment, the LMEE is allowed to reach room temperature and then stretched. The LMEE is then reheated or cooled for the next measurement. These measurements, which were taken at room temperature, are in good agreement with tests performed on samples that were either cooled or heated.

In addition, we performed cyclic loading experiments where the composite is stretched to 200% strain over 1000 cycles. In Fig. 3.11a, we show the thermal conductivity measurements in x and y direction, before starting cyclic test, after 1 cycle, and after 1000 cycles. The material is robust to cyclical loading, with only a slight increase in thermal conductivity measured after 1000 cycles of 200% strain. As shown in Fig. 3.11b and c, the modulus slightly drops (from 182 kPa to 176kPa) and plastic deformation slightly increases (by $\sim$ 4%) with number of cycles. The slight increase in the thermal conductivity k_y could be attributed to the Mullins effect and permanently increasing aspect ratio of LM particles.

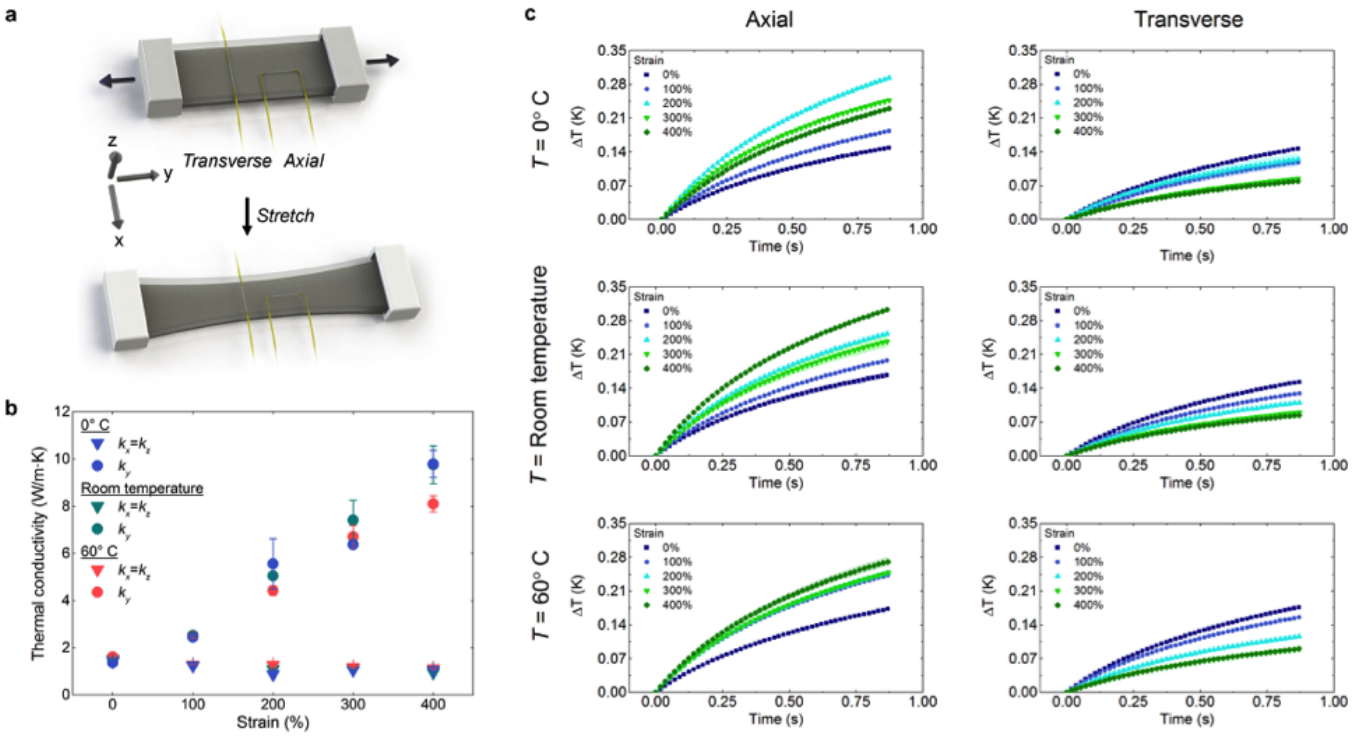

Figure 3.8: Temperature dependence. a) Schematic of the testing setup. b) Compiled data showing the $\Phi = 50\%$ thermal conductivity stretch dependence for 0°C, room temperature, and 60°C (n=5, error bars represent $\pm$ 1 s.d.). Good agreement is observed between the three temperatures, with k_y varying by an average of 8.3% from the room temperature measurement over all strains (maximum variation of 17% at 400% strain and 60°C). c) ΔT versus time of $\phi = 50\%$ for the axial and transverse wire up to 400% strain in 100% strain steps. Data symbols represent the average and the shaded areas correspond to the standard deviation for the 5 measurements for each condition. Hotwire lengths can vary between tests resulting in a non-monotonic temperature change across strain steps. This is accounted for by q, the volumetric heating of the wire per unit length, when calculating thermal conductivity.

3.4 Effective Medium Theory

As discussed in the result section, the experimental measurements of thermal conductivity are in good agreement with predictions obtained from effective medium theory (EMT). The EMT model is based on a Bruggeman formulation that has been adapted to predict the orthotropic bulk values of the thermal conductivity (k_x, k_y, k_z) as a function of both LM volume fraction and stretch. The principal directions are parallel to the sample's orthogonal surfaces, with the y-direction corresponding to the axis along which the sample is stretched.

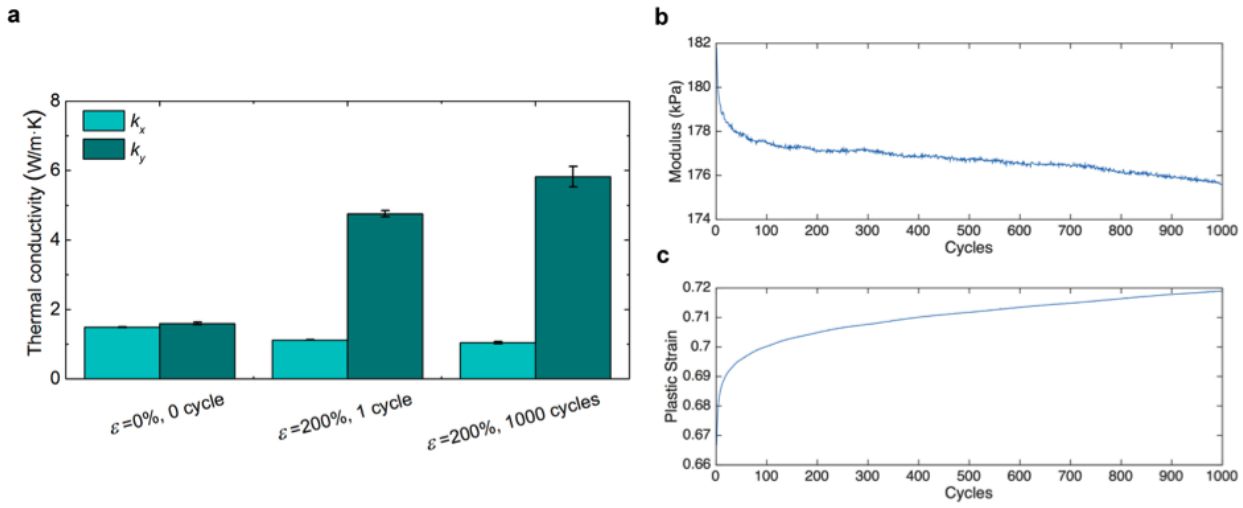

Figure 3.9: Cyclic testing. a) Thermal conductivity for a $\phi = 50\%$ composite tested at a strain (ϵ) of 0% and then stretched to 200%. The sample is then cycled 1000 times up to a strain of 200%. Thermal conductivity is then evaluated after the 1000 cycles at a strain of 200% (n=5, error bars represent $\pm$ 1 s.d.). b) 10% modulus and c) induced plastic deformation as a function of number of cycles.

3.4.1 Modified Bruggeman Formulation

In order to explain this experimentally-observed thermo-elastic coupling, we modify the Bruggeman formulation to account for the stretch-induced deformation of the ellipsoidal LM inclusions. For simplicity, we assume that all particles initially have a spherical shape (initial aspect ratio, $p_0 = 1$) and that the composite is incompressible. During uniaxial stretch in the y-direction ($\lambda_y = \lambda$), the inclusions will become elongated in the direction of loading and have an aspect ratio of $p = p_0\lambda^{(3/2)}$. The change in the shape of particles leads to anisotropic thermal conductivity of the effective medium. Following Sen et al.[171] I use a self consistent EMT that takes into account the shape of the ellipsoidal particles. I start from a Coherent Potential Approximation with depolarization factor L:

$$\frac{k_c - k_m}{Lk_c + (1-L)k_m} = \phi\frac{k_p - k_m}{Lk_m}. \tag{3.4.1}$$

This equation does not include particle-particle interactions and is more appropriate for a dilute composite. In order to account for interparticle interactions with the surrounding medium, I use differential effective medium theory.[143] In this scheme, I incrementally introduce an infinitesimal

suspension of particles to the dispersion medium (step s) and then use this mixture as the reference matrix for evaluating the influence of the next increment (step $s+1$). At each incremental step, I assume that the dispersion phase and medium share the same anisotropy in thermal conductivity. This implies the following relationship between thermal conductivity at steps s (k_s) and $s+1$ (k_{s+1}):

$$\frac{k_{s+1}-k_s}{Lk_{s+1}+(1-L)k_s}=(\frac{\Delta v_p}{v_m+v_p})\{\frac{k_p-k_s}{Lk_p+(1-L)k_s}\} \tag{3.4.2}$$

The differential equation is:

$$\frac{dk}{k}=(\frac{dv_p}{v_m+v_p})\{\frac{k_p-k}{Lk_p+(1-L)k}\} \tag{3.4.3}$$

Defining $\Phi=V_p/(V_m+V_p)$, it follows that $d\Phi/dV_p=(1-\Phi)/(V_m+V_p)$. Taking the integral from k_m to k_c for thermal conductivity and from 0 to ϕ for Φ,

$$\int_{k_m}^{k_c}\frac{Lk_p+(1-L)k}{(k_p-k)k}\,dk=\int_0^{\phi}\frac{1}{1-\Phi}\,d\Phi \tag{3.4.4}$$

$$(\frac{k_p-k_c}{k_p-k_m})(\frac{k_m}{k_c})^L=1-\phi \tag{3.4.5}$$

Here, I modify L to predict the effective thermal conductivity as a function of stretch. For an incompressible material under uniaxial extension ($\lambda_y=\lambda$) the deformations orthogonal to the primary stretching direction are equal, i.e. $\lambda_x=\lambda_z$. Therefore, the aspect ratio of an incompressible particle as a function of λ_y is $p=\lambda_y^{3/2}$.

$$L_y=\frac{1-e_p^2}{2e_p^3}\{ln(\frac{1+e_p}{1-e_p})-2e_p\} \tag{3.4.6}$$

$$e_p=\sqrt{1-1/\lambda^{3/2}} \tag{3.4.7}$$

$$L_x=L_z=(1-L_y)/2 \tag{3.4.8}$$

For spherical particles with p=1, it follows that L=1/3, which recovers the original Bruggeman formula. Using this formula I was able to find a good agreement between experimental data for the increase in thermal conductivity of LMEEs with two different volume fraction of LMs and the theoretical prediction (Fig. 3.6e), without any data fit. Furthermore, using effective medium theories

(modified Bruggeman), I can now select the aspect ratio of embedded conductive particles in order to achieve a desired design criteria. As an example, this could be used to determine the extent of deformation required to get the necessary through-plane heat conduction for application of a thermal interface material in electronic devices.

3.5 Selected Applications

Because the LMEE composites are intrinsically soft and deformable, they can be incorporated as thermal interface materials into wearable computing[6] or thermally activated shape-programmable structures[172] and soft robotic systems[173,174] without altering the natural mechanics of the host. For such applications, high thermal conductivity is not enough; the material must be sufficiently soft to limit mechanical resistance to deformation. We demonstrate this functionality through a thermally activated soft "artificial muscle" that is actuated with embedded wires of Ni-Ti shape memory alloy (SMA) and used for caudal fin locomotion of a silent, soft swimming robot (Fig. 3.10 a and b). Compared with thermally insulating silicone and relatively stiff thermal tapes, sealing the SMA wires in LMEE allows for significant enhancements in actuation frequency, deflection, and duration (Fig. 3.10 c and d). Specifically, the LMEE is able to actuate for more than 10,000 cycles at a frequency of 5 Hz (33.3 min) with no observed degradation in amplitude (14 $\pm$ 1 degrees). In contrast, the unfilled silicone elastomer becomes saturated with heat and ceases to actuate after 2 s. Although the commercial tape can support cyclical loading, its relatively high mechanical stiffness results in a low steady-state amplitude of $\sim$3 degrees. When incorporated into the robotic fish, the LMEE-sealed SMA enables forward swimming at $\sim$0.15 body lengths per second (Fig. 3.10e). Furthermore, we demonstrate the LMEE's potential as an exceptional material for thermal management in stretchable electronics and wearable computing by comparing infrared temperature maps of an extreme high power (XHP) LED lamp on stretched LMEE and unfilled silicone elastomer membranes. The poor thermal conductivity of the unfilled silicone elastomer results in excessive heat accumulation that leads to thermal degradation and dramatic mechanical failure. In contrast, the LMEE effectively dissipates heat and allows continuous operation of the LED (Fig. 3.10 f-h). To demonstrate the

potential use of LMEEs as heat spreaders for low-profile wearable applications, an XHP LED lamp is mounted to a strip of LMEE that is wrapped around the thigh. This wearable lamp can operate during running, hiking, and cycling to provide exceptional visibility at night without the need for a socket mount (Fig. 3.10 i-k). It runs at power outputs greater than 1W and produces substantially more light and heat than standard indicator LEDs, which run on milliwatts of power. The XHP LED is representative of a broader range of heat-generating devices (e.g., processors, transformers, power supplies) that could potentially be used in wearable computing and stretchable electronic circuits.

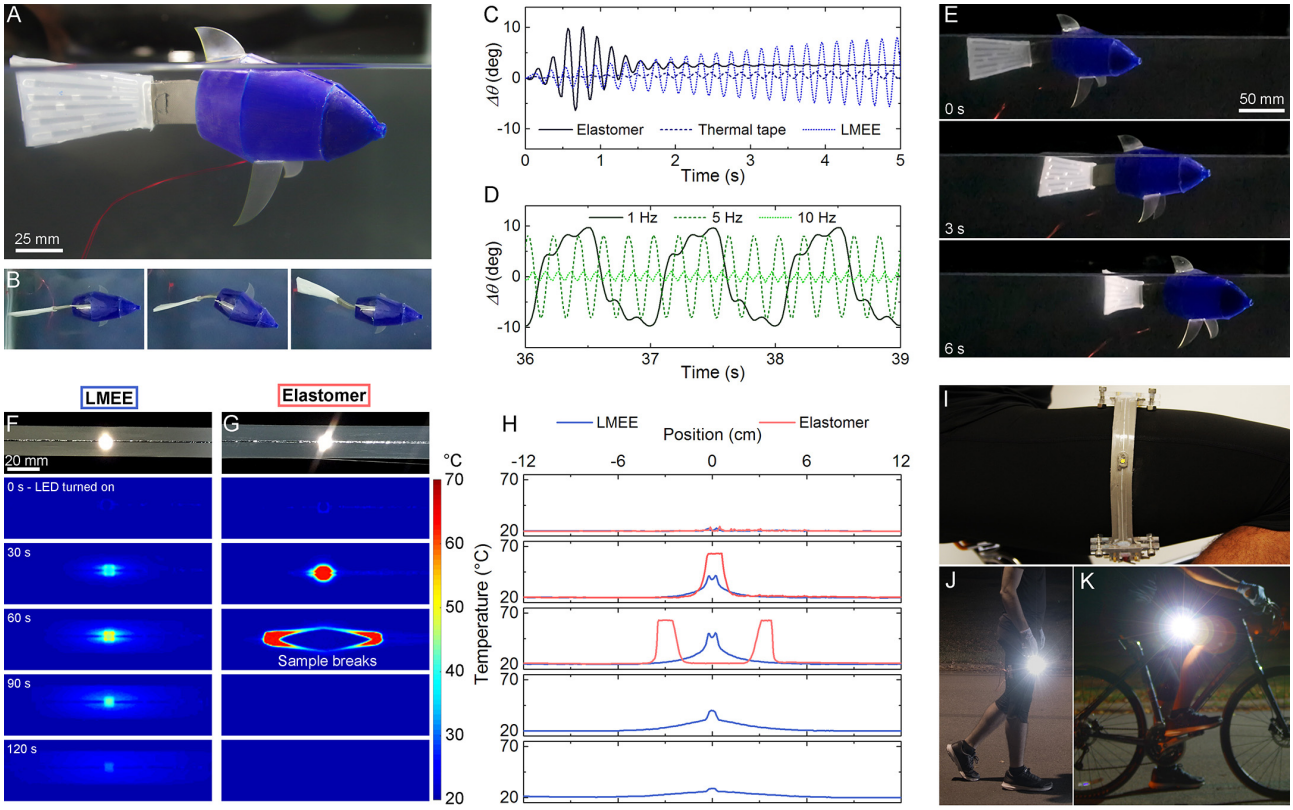

Figure 3.10: Soft robot and stretchable electronics implementation of the LMEE composite. a) Soft robotic fish composed of a silicone body and caudal fin connected by an LMEE-sealed SMA actuator. b) Top-down view during forward caudal fin locomotion. c) LMEE, unfilled silicone elastomer, and commercial thermal tape actuated at a frequency of 5 Hz. d) LMEE actuated at 1-, 5-, and 10-Hz signal. e) Time sequence images of the soft robotic fish swimming with a stroke frequency of 0.7 Hz. f) XHP LED lamp mounted on an LMEE composite stretched to 400% strain with a sequence of IR images during LED operation. g) The same experiment on an elastomer sample where the sample breaks at 60 s due to significant localized heating. h) Temperature versus time plots for the IR image sequence, where the temperature is measured across the sample's length. LED is turned on and off at t = 0 s and t = 70 s, respectively. i) An XHP LED is mounted to a strip of LMEE that is wrapped around the leg and shows high brightness during j) running and k) cycling.

3.6 Conclusions

Electrically insulating solids with high thermal conductivity are typically rigid due to the dynamics of phonon transport within an elastic medium. In this Chapter, I reported a soft elastomer composite that overcomes this constraint and exhibits the highest-ever combined values of thermal conductivity and stretchability (Fig. 13.1e). This high performance is accomplished by exploiting the unique thermal-mechanical interactions of LM microdroplets that are suspended within a silicone elastomer. The composite achieves an exceptional combination of low elastic modulus (<100 kPa; i.e., softer than human skin), high strain limit (>600%), and high thermal conductivity (k), which ranges from 4.7 W/mK (stress-free state) to nearly 10W/mK (when stretched). This represents a 25× to 50× increase in thermal conductivity compared with soft rubbers, i.e., similar in magnitude to some metals (e.g., bismuth, manganese, stainless steel) while having a 10^5 to 10^6 lower elastic modulus.

The ability to achieve high thermal conductivity with an elastomer without altering its elastic properties is enabled through LM microstructure and the distinctive thermal-mechanical coupling in which the deformation of an elastomer matrix creates needle-like LM inclusions in situ. Previous studies of LM suspensions in elastomer did not explore such critical factors and hence failed to capture the breakthrough performance presented here. These experimentally measured values are also found to be in strong agreement with predictions from a theoretical model that I derived based on Bruggeman EMT. Such agreement is achieved without the aid of data fitting and provides further evidence for the critical role of in situ elongation of LM inclusions. As previously shown by Style et al.,[175] altering the size of liquid inclusions in a compliant matrix can result in changes to the elastic modulus of the composite. However, according to my EMT model, inclusion size has little influence on thermal conductivity (which is instead largely dependent on LM volume loading and inclusion aspect ratio). This difference in dependency can be used for matching the elastic properties of composites without altering the thermal properties.

The combination of high thermal conductivity and elasticity is especially critical for rapid heat dissipation in applications such as wearable computing and soft robotics, which rely on soft and stretchable functionality. I show that LMEE composites can be used to manage heat within an

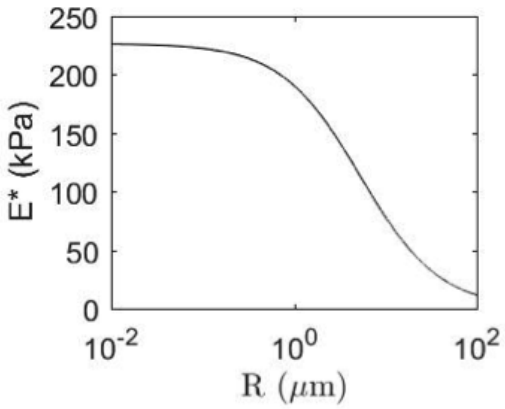

Figure 3.11: Theoretical prediction for dependence of effective modulus of inclusions (E^*) on droplet radius (R) for E = 85 kPa and γ = 0.5 N/m. The prediction is based on a theory reported in Style et al.[175]

SMA-powered swimming robot and stretchable, body-mounted circuits for high-power illumination. Together, these examples show the potential for LMEEs to dramatically improve thermal management in applications that require electrically insulating materials with both rapid heat conduction and soft elastic functionality. In particular, I anticipate that this class of materials will be enabling for soft robotics, shape-changing programmable matter, stretchable electronics, and soft-matter technologies designed for physical interaction with humans.

Until now, I have presented the mechanical, dielectric and thermal properties of LMEEs. During the mechanical tensile experiments, I occasionally (in about 30-40% of tested samples) observed premature failure of unfilled elastomer samples at deformation less than 50% of maximum strain at break that was measured for other samples. The premature failures were due to propagation of small cracks that was introduced inside the tensile samples during fabrication procedure. On the other hand, all of the LMEE tensile samples with 50% volume fraction of LM were able reach the maximum strain at break without experiencing pre-mature failure. This behavior made me think about the influence of microscale LMs on the tear resistance of elastomers. Hence, in the next chapter, I systematically investigate the fracture toughness of LMEE composites and compare them with other synthetic soft and tough materials.

Chapter 4

Extreme Toughening of Soft Materials with Liquid Metal

Reference:

N. Kazem, M. D. Bartlett, and C. Majidi, "*Extreme Toughening of Soft Materials with Liquid Metal*", Advanced Materials, 2018, Accepted.

4.1 Introduction

Soft and tough materials are critical for engineering applications in medical devices[176], stretchable and wearable electronics[177], and soft robotics[1]. Toughness in synthetic materials is mostly accomplished by increasing energy dissipation near the crack tip with various techniques from mesoscale approaches like particle-filled composites to molecular scale techniques including hybrid and double network gels and polymers[61,178–181]. However, bio-materials exhibit extreme toughness by combining multi-scale energy dissipation with the ability to deflect[182,183] and blunt an advancing crack tip[184]. In this Chapter, I demonstrate a synthetic materials architecture that also exhibits multi-modal toughening, where by embedding a suspension of micron sized and highly deformable liquid metal (LM) droplets inside a soft elastomer, the fracture energy dramatically increases by up to 50x (from $250 \pm 50\, J/m^2$ to $11,900 \pm 2,600\, J/m^2$) over an unfilled polymer. For some LM-embedded elastomer (LMEE) compositions, the toughness is measured to be as high as $33,500 \pm 4,300\, J/m^2$, which far exceeds the highest value previously reported for a soft elastic material. This extreme toughening is achieved by means of (i) increasing energy dissipation, (ii) adaptive crack movement, and (iii) effective elimination of the crack tip. Such properties arise from the deformability and dynamic rearrangement of the LM inclusions during loading, providing a new mechanism to not only prevent crack initiation, but also resist the propagation of existing tears for ultra tough, highly functional soft materials.

Natural materials like skin and bone have extreme toughness because of their ability to dissipate mechanical energy at multiple length scales and deflect or blunt the tip of an advancing crack[183,184]. In bone, for example, it requires far more energy ($\Gamma \sim 31,000\, J/m^2$) to extend a short crack ($500\, \mu m$) through the cross section than to split it along the length ($\Gamma \sim 50 - 200\, J/m^2$), which results in crack deflection/twist and an increase in the resistance to crack propagation[183]. Additionally, soft bi-

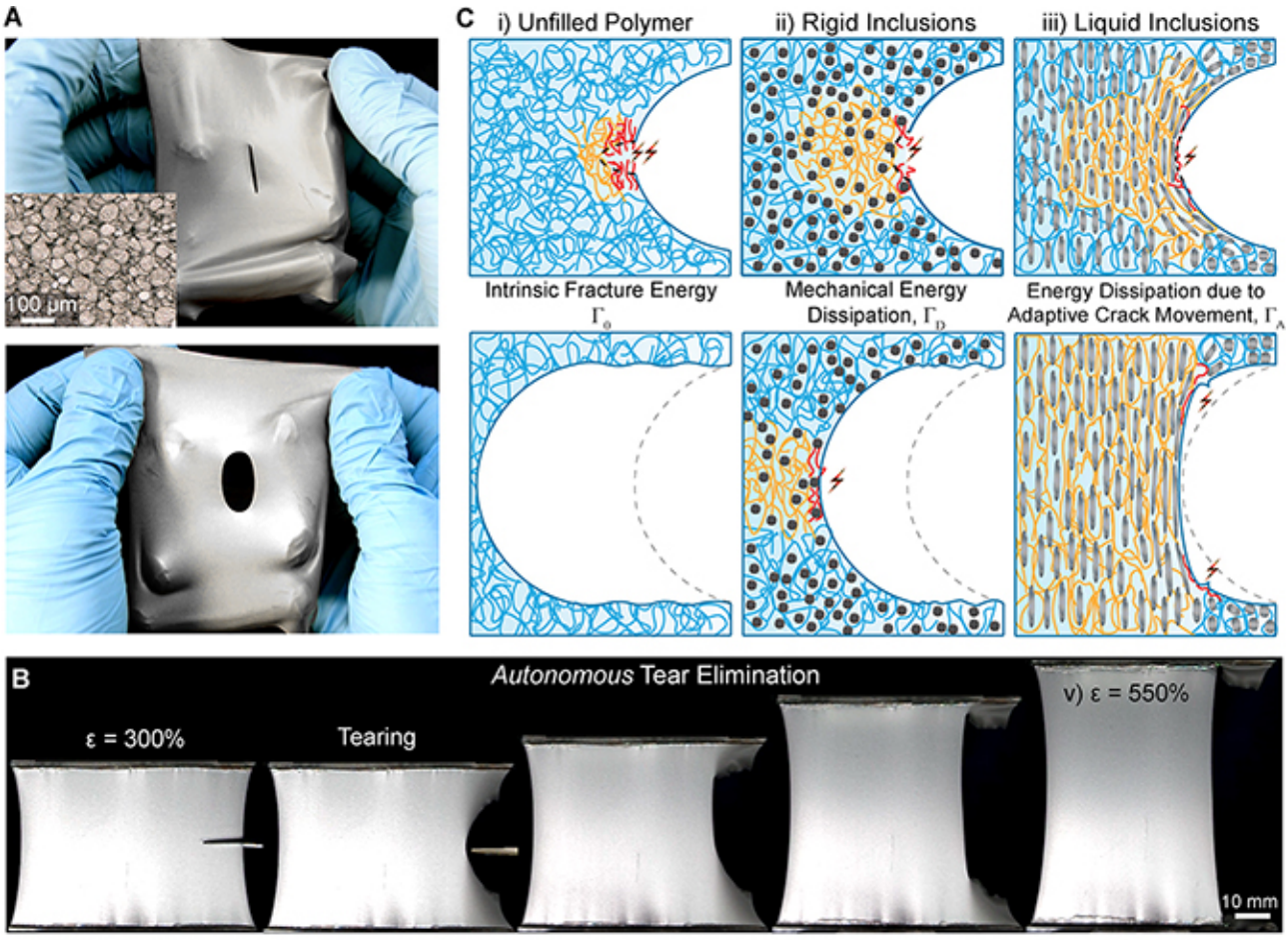

Figure 4.1: A) A soft and tough LMEE film is notched and easily deformed without crack propagation. The inset is an optical micrography of LMEE in an undeformed state. B) The extreme tear resistance of LMEE is demonstrated by adding a notch to a 50% LM volume ratio sample stretched to 300% strain. As stretching continues, the notch is completely blunted through an autonomous tear elimination mechanism. C) Schematic of different mechanisms of dissipating external mechanical work in a notched sample. i) In an unfilled polymer, energy dissipation arises from intrinsic dissipation as polymer chains break, Γ_0. ii) Addition of rigid inclusions increases the size of the process zone and enhances the fracture energy by increasing the mechanical dissipation, Γ_D. iii) Elongation of liquid droplets creates preferential and adaptive crack deformation that eliminates the notch and increases mechanical dissipation by an amount Γ_A.

ological tissues like rabbit skin are extremely difficult to tear because they are composed of fibril networks that adapt their microstructure by means of straightening, reorienting, stretching, and sliding to redistribute internal load and dissipate energy.[184] However, whereas natural materials use multi-scale, multi-modal mechanisms for toughening, most existing synthetic materials only exploit energy dissipation in the proximity of a crack through molecular and mesoscale dissipative mechanisms.[185,186] In the case of traditional, particle-filled polymers and elastomers[187–190], energy dissipation and reinforcing effects have been designed through the bonding and composition of the

polymer and filler.[178,191,192] Moreover, fiber-reinforced gels and elastomers have shown an increase in critical fracture energy[184,193] due to the dissipation of energy during fiber pull out. In addition to increasing fracture toughness, however, these approaches alter the bulk mechanical response of the material, typically observed as a dramatic increase in stiffness or tensile modulus relative to the unfilled gel or elastomer. This stiffness increase is typical for rigid filler systems and is limiting for emerging applications in wearable computing, medical devices, and soft robotics that require high mechanical compliance, high deformability and toughness. Recently, many studies have also focused on fabricating soft and tough hydrogels.[186] One of the most successful approaches is to create double networks (DN) of interpenetrated polymers. In DN hydrogels, one of the networks breaks upon stretching and dissipates most of the applied mechanical work while the other network maintains structural integrity and provides stretchability.[61,181] While extensive developments in DN hydrogel engineering have resulted in materials with 0.1-1 MPa stiffness and fracture energies of $10^2 - 10^4\, J/m^2$, the synthesis is highly specialized and only a few polymers (PAAM, alginate and agar) have been used to achieve DN architectures.[194] Progress in this field depends on discovering new architectures to enhance fracture toughness by combining energy dissipating mechanisms with the ability to deflect crack tip efficiently without introducing extreme stiffness in composites, and that are compatible with a broader range of soft materials.

4.2 Experimental Results

Here, I introduce an approach to dramatically increase the fracture energy of soft materials through a combination of energy dissipation, crack deflection, and crack blunting. I accomplish this by embedding elastomers with microscale droplets of liquid metal (LM) alloys (Fig. 4.1A). Recently, it has been shown that liquid droplets dispersed in a soft material can alter its mechanical stiffness[175,195–197]. LM alloys like eutectic gallium-indium (EGaIn),[140,198] are of particular interest, because their high conductivity can also be used to tailor the thermal and electrical properties of a wide variety of polymers including silicones, urethanes and other conventional rubbers.[199] EGaIn is additionally non-toxic[112] and is known to form a thin (0.5-3 nm) oxide shell in the presence of oxygen.[115] One

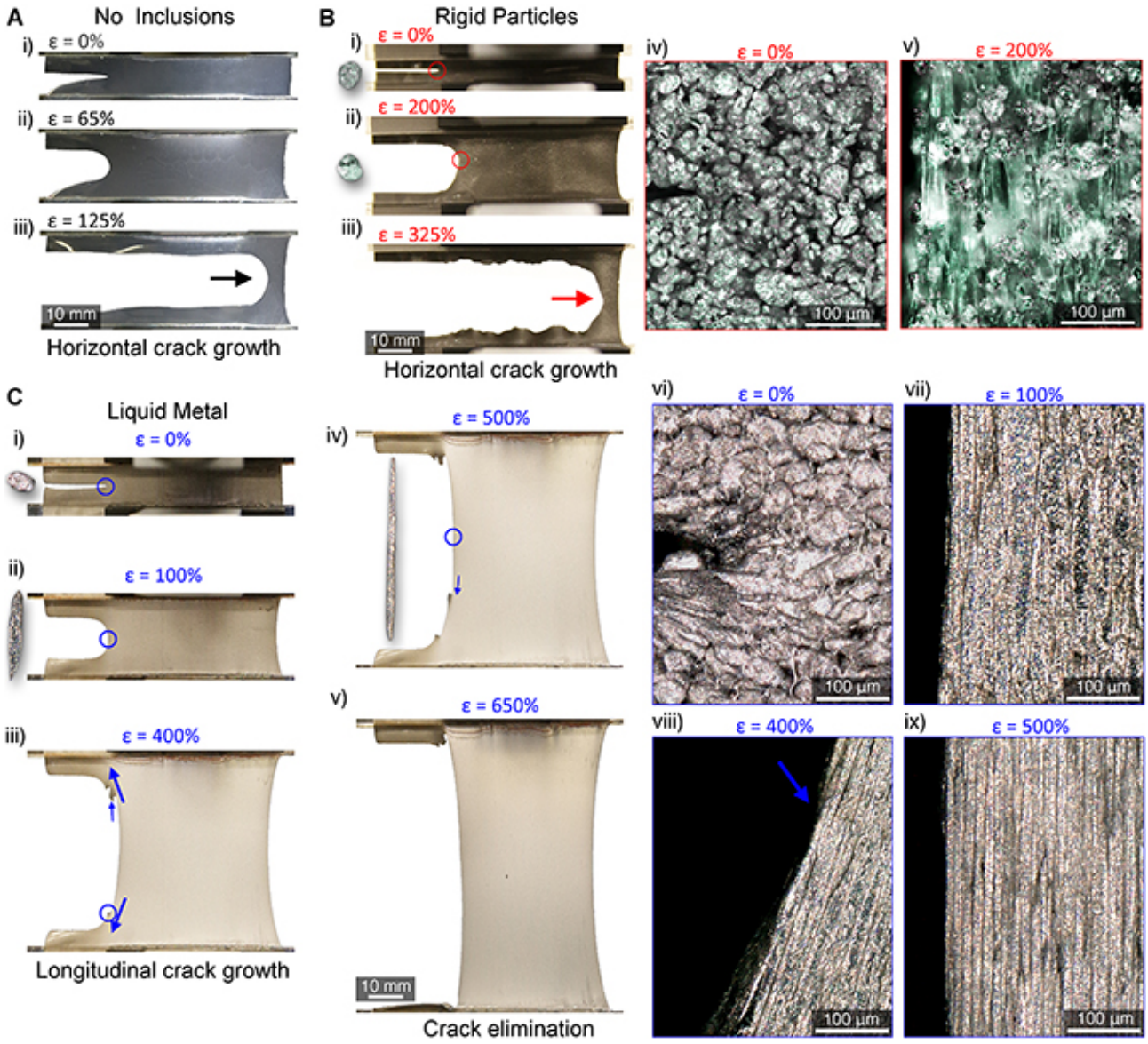

Figure 4.2: A) Horizontal crack movement in a notched experiment of an unfilled polysiloxane with a sample at i) unstretched state, ii) 65%, and iii) 125% strain. B) Similar horizontal crack movement in 30% volume fraction rigid particles at i) unstretched state with a representative inclusion morphology shown, ii) 200% strain where the representative rigid inclusion is undeformed, and iii) 325% strain. Representative optical micrographs during stretching are shown at (iv-v). C) Longitudinal crack movement and crack elimination in 50% volume fraction liquid metal inclusions, with the LMEE sample at i) unstretched state with a representative inclusion morphology shown, ii) at 100% strain where the representative liquid inclusion is elongated, iii, iv) with 400% and 500% and vertical tear movement, and at v) 650% where the tear is completely eliminated. The optical micrographs (vi-x) represent the circled regions in the photographs at the corresponding strains.

especially important attribute of these soft heterogeneous systems is that the liquid droplets deform with the matrix and elongate along the direction of loading.[200] This is in contrast to rigid particles, which induce an internal mechanical mismatch that results in a non-uniform deformation with stress

concentrations at the particle/matrix interfaces. To demonstrate the extreme resistance of LMEE to tearing, I stretched a sample with 50% volume ratio of LM to 300% strain and cut a notch with a pair of scissors inside the material (Fig. 4.1B). By stretching the sample further, the crack becomes blunt and eventually disappears. This autonomous tear elimination allows notched samples with 50% LM volume fraction to approach the same strain limit ($\sim 600\%$) as un-notched samples. Traditionally, observations of longitudinal tear movement, referred to as knotty tearing, have been reported in carbon-black-filled elastomers[201,202], and more recently in a bi-continuous hydrogel[203]. According to Gent et. al.[204], knotty tearing happens only over certain temperature ranges and strongly depends on the type of carbon black and specific elastomer being used. Although the toughening mechanisms of rigid particle-filled composites have been extensively studied and implemented in a variety of material systems, the fracture behavior and toughness of a liquid-filled composite has not been thoroughly investigated. Here, I show that embedding a polydisperse suspension of randomly distributed droplets of LM alloy can increase fracture energy of the base elastomer by up to 50×. This toughening effect is examined in soft polysiloxane elastomers and composites by performing notch fracture experiments with *in-situ* microscopy techniques to observe micro-structural evolution during crack propagation. This allows for the investigation of crack deflection and crack elimination mechanisms that are not typically observed in soft and tough synthetic materials.

Since low melting point alloys can be embedded inside elastomers in either liquid or solid phases at room temperature (depending on the alloy) with similar microstructure and morphology, they are an ideal model material to study different mechanisms to enhance fracture energy. I shear-mix Field's metal (eutectic of bismuth, indium and tin with melting point at $\sim 62°C$) and the elastomers in an oven at temperatures above 70°C while the metal is in a liquid state. Field's metal is mixed into part A and B of the elastomers separately using a pestle and mortar, for 5-7 minutes, until the desired particle size ($\sim 15\,\mu m$, Fig. 4.3) is achieved. The pestle and mortar are placed inside the oven before mixing, to avoid solidification of the liquid Field's metals during shear mixing. After mixing inside the oven, the Field's metal emulsions are cooled for 30 minutes inside a freezer ($T \sim -15°C$) and then equilibrated at room temperature for 10 minutes. Component A and B are then mixed and molded into samples using mask deposition. The Field's metal inclusions inside the elastomer become rigid at room temperature and stay undeformed inside the soft elastomer during elongation

experiments at ambient temperature.

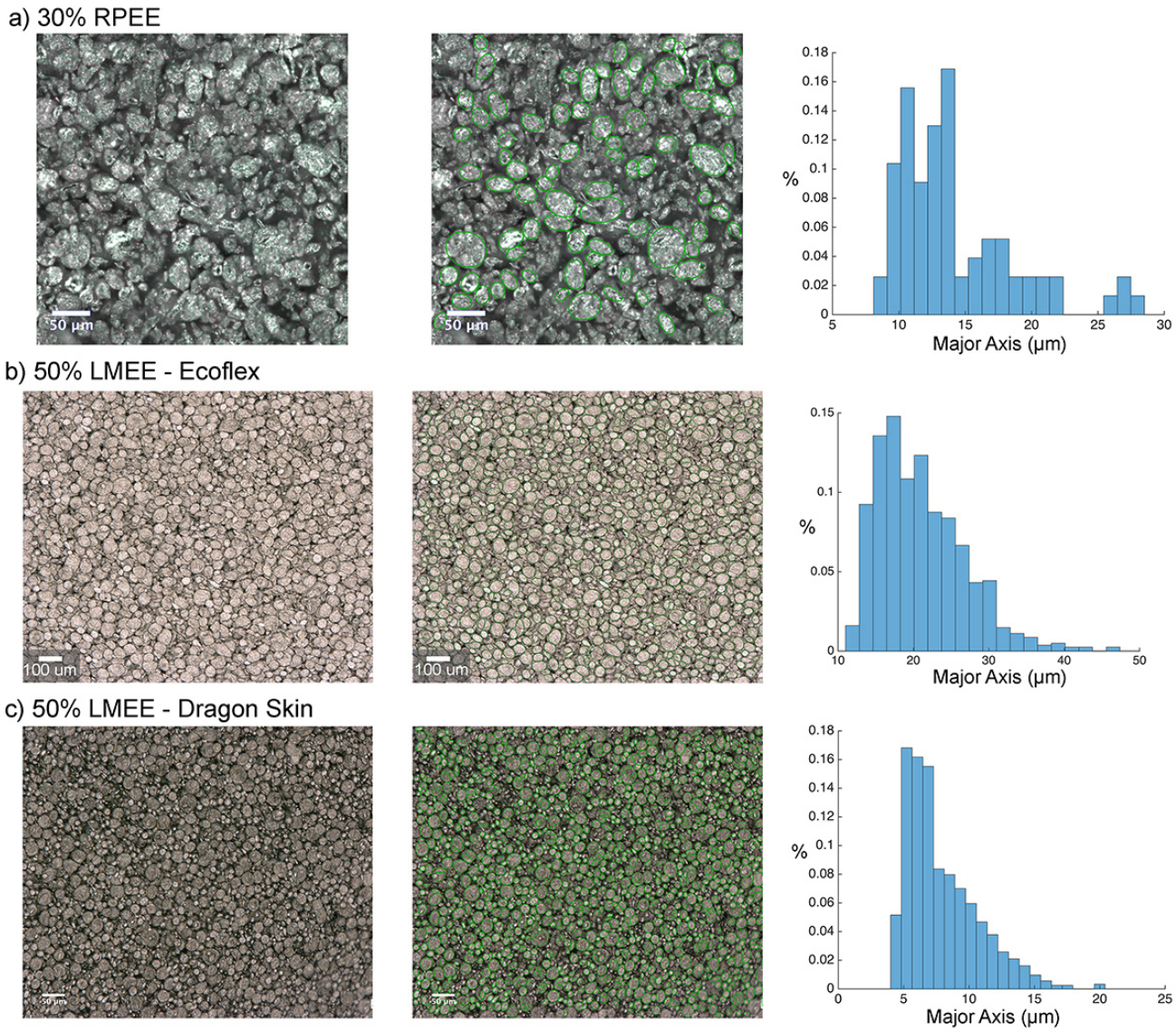

Figure 4.3: Particle size distribution of a) 30% volume ratio of rigid Fields metal inside Ecoflex 00-30, b) 50% volume ratio of liquid metals inside Ecoflex 00-30, and c) 50% volume ratio of liquid metals inside Dragon Skin 10 Slow, using image analysis[205].

I show that the inclusion of liquid droplets can provide similar energy dissipation methods that already exist in unfilled polymers and rigid-filler composites, as well as additional dissipative modes, due to tear deflection and elimination. In an unfilled polymer, according to Lake and Thomas,[186,206] the fracture energy, Γ_0, is due to the release of energy in a polymer chain after a failure in one of the atomic bonds (Fig. 4.1C i). In order to enhance critical fracture energy of a material, the necessity to engineer dissipating mechanisms to absorb the external work is well established.[207,208] Accordingly, the inclusion of rigid fillers inside a polymer allows the microstructure to dissipate more energy (Γ_D)

through a variety of mechanisms, including load sharing between multiple molecules and one filler particle[209], slipping of molecular chains from surface of fillers[207], and detaching polymers from fillers[210] (Fig. 4.1C ii). In contrast to rigid fillers, liquid inclusions can be stretched and elongate with the background strain field and deform into needle-like ellipsoids as the composite is stretched (Fig. 4.1C iii). Such elongation causes the tear to bifurcate and redirect along the direction of stretch. This is in stark contrast to crack propagation in other soft materials, where tears typically propagate in the transverse rather than longitudinal direction (Fig. 4.1C i-ii). When the tear reaches the top and bottom edges of the LMEE sample, it vanishes and the composite can be stretched to its natural (intrinsic) strain limit. This adaptable crack movement can allow the composite to dissipate an additional energy associated with autonomous tear elimination Γ_A (Fig. 4.1C iii), and increase the total energy dissipation to $\Gamma_T = \Gamma_0 + \Gamma_D + \Gamma_A$. This new mode of crack deflection/elimination, extends energy dissipation (Γ_A) throughout the whole area of the composite and activates significantly larger area compared to the smaller area of process zone inside particle-filled composite. This increase in active dissipation area can dramatically enhances the total energy dissipation (Γ_T).

4.2.1 Pure Shear Test

To measure fracture energy, I use a pure-shear fracture test method that had previously been adopted for soft materials.[61,211] In this method, a notch is cut into a sample and then the sample is stretched to determine the onset of failure (maximum force). The fracture energy Γ corresponds to the energy required to stretch an un-notched sample to the same displacement, divided by the cross-sectional area. As shown in Fig. 4.2A, a sheet of homogenous (unfilled) silicone (Ecoflex 00-30, Smooth-On) with a notch is stretched. The tensile force reaches a maximum at ~100% of strain, at which point the notch continuously propagates horizontally to complete failure. In order to compare the effects of liquid inclusions with rigid inclusions, I embedded micro droplets of rigid, indium-based low melting point alloy (Bi-In-Sn; Field's metal) inside the same silicone matrix. With the addition of rigid inclusions, energy dissipation increases near the crack tip. Fig. 4.2B shows a sample of rigid particle embedded elastomer (RPEE) with 30% volume ratio of rigid inclusions. The optical image at 0% strain shows the morphology of polydispersed rigid inclusions, with major axes of $14.2 \pm 4.4\,\mu m$

close to the crack tip (Fig. 4.3). As the sample is stretched, the rigid inclusions do not deform and are observed to slip and tear from the surrounding rubber. This is due to the stiffness mismatch between the host elastomer and the particles and results in an increase in the overall stiffness of the composite. As shown in the optical image of crack tip at 200% strain, the debonding of rigid inclusions create many voids, around which the surrounding polymer is highly stretched (Fig. 4.2B iv-v). This delamination and localized stretching greatly increases the dissipation of energy and the resistance against the propagation of tear. The crack eventually unzips horizontally through the sample (similar to the unfilled elastomer) and causes complete failure at a strain of ∼320%.

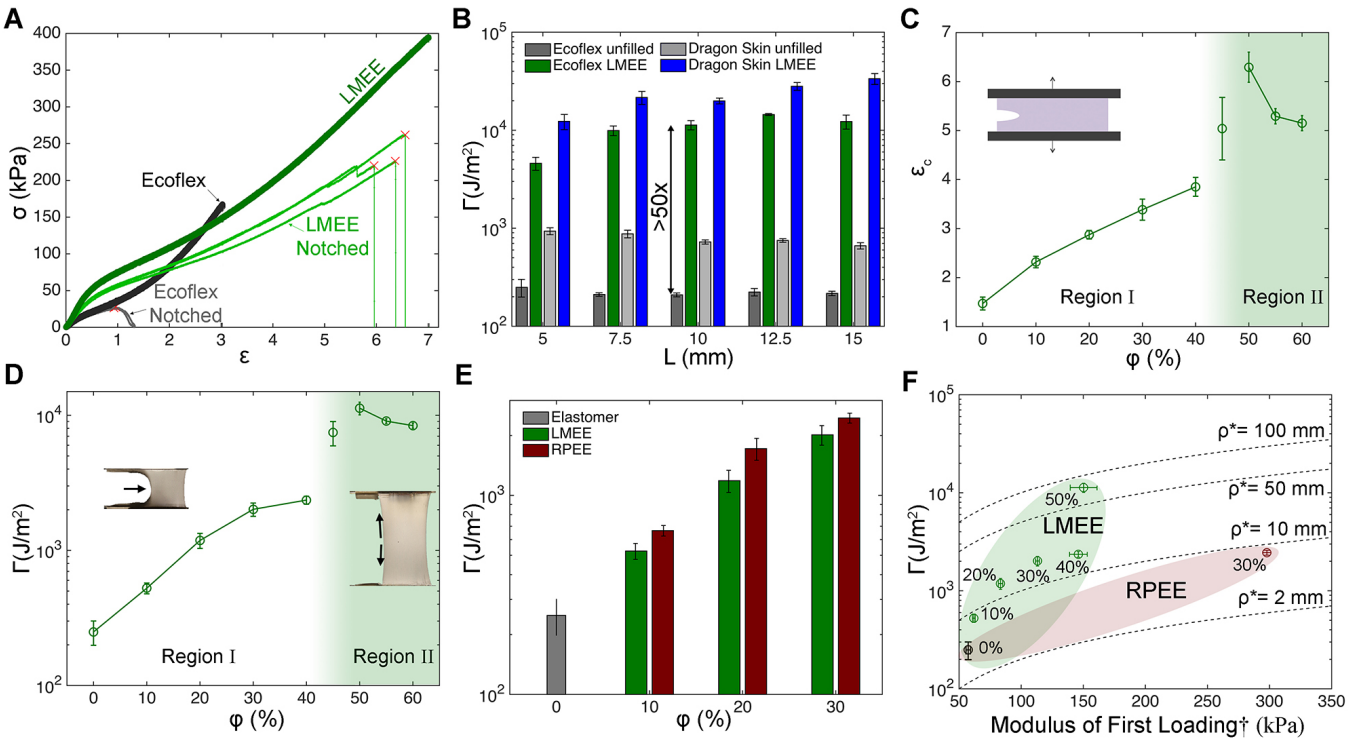

Figure 4.4: A) Stress vs strain curve for pure shear tests performed on 70 mm × 10 mm samples of unfilled Ecoflex and LMEE with 50% LM volume ratio. Black and dark green are un-notched Ecoflex and LMEE. Brown and light green are Notched Ecoflex and Notched LMEE. B) Comparison between the fracture energy Γ of unfilled Ecoflex (dark grey), 50% volume fraction of LM inside Ecoflex (green), unfilled Dragon Skin (light grey) and 50% volume fraction of LM inside Dragon Skin with higher intrinsic fracture energy (blue). C) Plot of critical strain ϵ_c (strain at the maximum force), as a function of LM volume fraction. D) The increase in fracture energy as a function of LM volume fraction. In region I, the fracture energy enhancement is due to the increase in mechanical dissipation in a similar manner to rigid inclusions. In contrast, for region II, large enhancement is due to a crack deflection and elimination mechanism. E) Comparison between fracture energy of LMEE and RPEE in region I. F) Relation between enhancing the fracture energy and (†)tensile modulus at the first loading cycle of LMEE and RPEE composites. Dashed lines are curves corresponding to different values of the elasto-adhesive length scale, ρ^*.

The mechanical response of the LM-embedded elastomer (LMEE) composite is significantly different from those with RPEEs and unfilled silicone. As can be seen in Fig. 4.5, in contrast to rigid inclusions, liquid droplets can deform with the surrounding elastic medium. In Fig. 4.2C, I show different snapshots of a notched LMEE sample with 10 mm initial length and 50% volume ratio of LM. The major axis of an inclusion at 0% strain (Fig. 4.2C vi) is $21 \pm 6\,\mu m$ (Fig. 4.3), similar to what is measured in an RPEE. As the notched sample is stretched, the liquid inclusions elongate with the background strain field. Subsequently, close to the crack edge, the high local strain field results in higher droplet elongation compared to those that are far from the tear. The length scale of the process zone is around 650 μm (Fig. 4.5). A new mechanism of toughening emerges for LMEE composites with a high volume fraction of liquid metal ($\phi \geq 50\%$). As shown in Fig 4.2C-iii, a small step-like crack located in the process zone starts moving longitudinally along the direction of stretch. During this longitudinal movement, the tear moves along the interface of elongated liquid inclusions and elastomer. It occasionally ruptures a liquid droplet or transmits to the neighboring inclusion and moves vertically (Fig. 4.2C iii, iv and viii). This adaptive movement of the tear leads to a complete elimination of the initial notch (Fig. 4.2C v and ix). Eventually, the tensile strain limit of the LMEE sample with a notch approaches that measured for ultimate strain at break of an un-notched sample (Fig. 4.4A).

In the pure shear test, it is assumed that the process zone in the front of the crack tip is small relative to the overall dimensions of the sample such that the boundaries (clamps) don't have any influence. However, this assumption is not valid for the case of vertical crack movement where the crack travels along the applied load. For the case of LMEE samples ($\phi = 50\%$) with shorter sample length (L = 5 mm), the longitudinal crack reflects from the walls, and the boundary interference leads to premature failure. In order to remove the boundary effects, I have performed the pure-shear fracture test with longer sample lengths. My experimental results show an increase in fracture energy of LMEE ($\phi = 50\%$) as the length increases from L = 5 mm to L=7.5 mm (green bars in Fig. 4.4B). However, for L $\geq$ 7.5 mm, Γ is invariant to sample length and reaches its peak value. Hence, all the values for fracture energy of LMEEs with vertical crack movement ($\phi \geq 45\%$) are reported for L=10 mm. As shown with grey bars in Fig. 4.4B, such a length dependency on fracture energy is not observed for the case of unfilled elastomer, which only exhibits horizontal crack movement for all

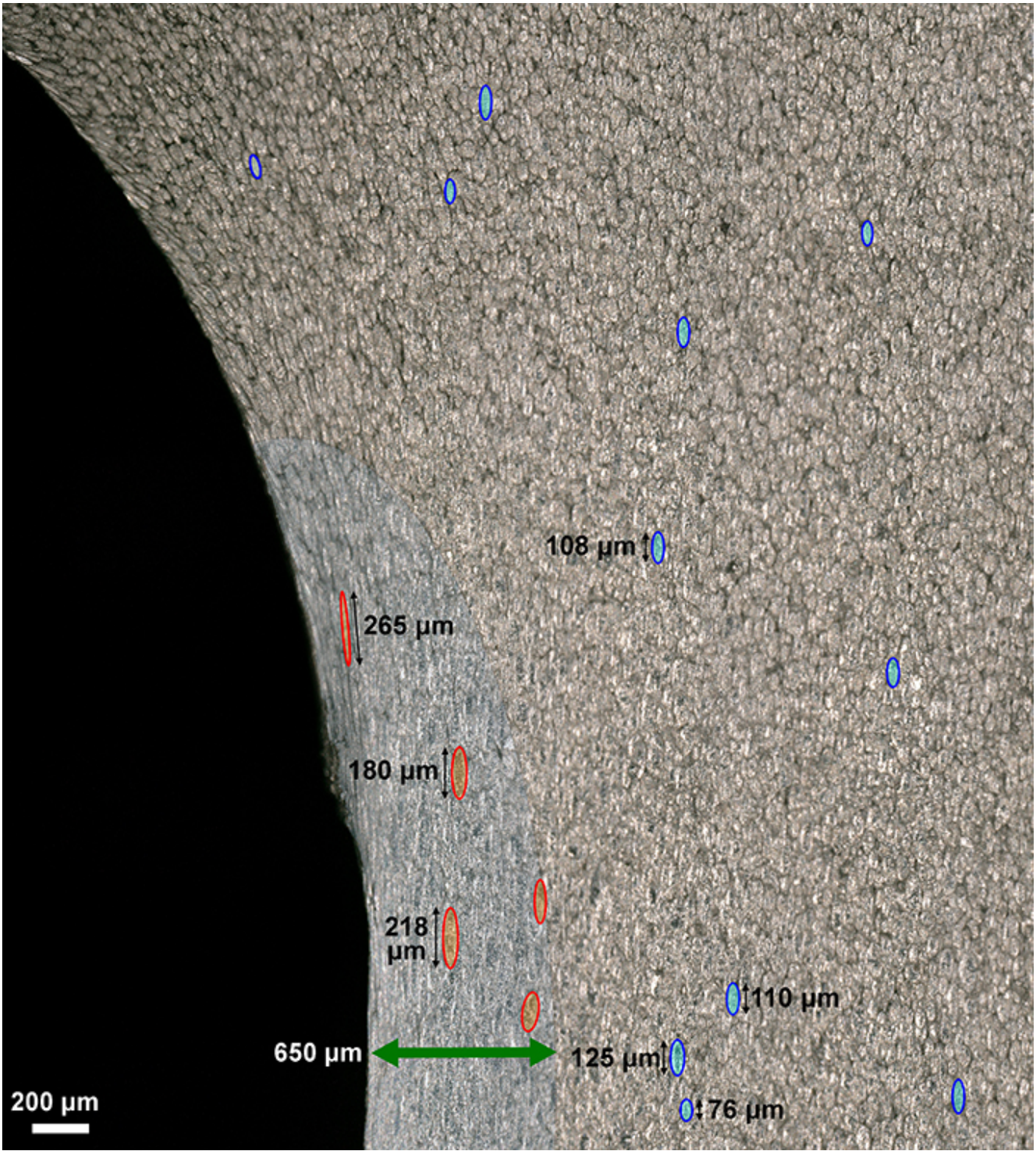

Figure 4.5: High resolution optical image of LMEE with $\phi = 50\%$, at strain of 100%. As a few representative droplets are highlighted, inside the process zone the droplets are highly elongated while outside of this zone the deformation is smaller and fairly uniform.

sample lengths. Moreover in Fig. 4.6, I show that by changing the crack length of LMEE samples with $\phi = 50\%$, from 10 mm to 30 mm, the critical strain (ϵ_c) remains similar. Depending on the volume fraction of LM (ϕ), I observe two distinct regions. Fracture behavior in region I ($\phi \leq 40\%$) is dominated by energy dissipation of inclusions, while in region II ($\phi \geq 45\%$) it is dominated by longitudinal crack movement and notch elimination. Fig. 4.4C and 4.7 show the increase in strain at maximum tensile force for notched samples with different liquid metal loadings. The increase in critical strain is smooth and monotonic up to $\phi = 40\%$. In this region, the fracture energy increases steadily from $\Gamma = 250 \pm 50\, J/m^2$ for the unfilled elastomer to $\Gamma = 2,360 \pm 160\, J/m^2$ for a 40% volume ratio LMEE (Fig. 4.4D). In region I, the RPEE shows a similar trend and slightly higher fracture energy compared to LMEE (with 95% confidence bound[212]), which could be attributed to more energy dissipation due to slipping and friction between rigid particles and the polymer (Fig. 4.4E and Fig. 4.8). However, in region II ($\phi \geq 45\%$), the LMEE shows a sharp increase in critical strain as well as fracture energy. For these materials, the crack moves longitudinally and enhances the fracture energy significantly. However, by increasing volume fraction of LM even higher than 50%, the critical strain decreases (Fig 4.4C, region II) and our experimental data shows a slight decrease in the fracture energy (Fig. 4.4D, region II).[213] Additionally, Fig. 4.4F, shows the enhancement in fracture energy as a function of tensile modulus (the slope of stress vs strain curves between 10% and 20% of strain) measured during the initial loading cycle (before the effect of strain softening, i.e. Mullins effect, appears). The dashed lines are the curves for different values of the elasto-adhesive length scale, $\rho^* = \Gamma/E$, which is indicative of the length in front of crack tip where the material experiences large strain.[186] As shown here, LMEE increases the length of active energy dissipation from ~3 mm to more than 50 mm, in contrast to RPEE where the increase in ρ^* is modest (ρ^* <10 mm). Hence, I observe that liquid inclusions are much more effective in increasing tear resistance while maintaining greater compliance and stretchability when compared to composites with rigid inclusions.

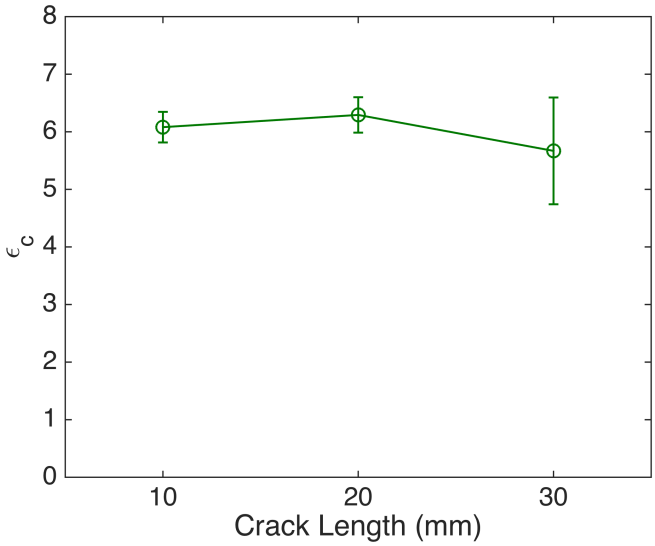

Figure 4.6: Notch sensitivity of LMEE with 50% volume fraction of liquid metal. This is the plot of critical strain (corresponding to a maximum force) as a function of crack length.

4.3 Discussions

In both composites with rigid and liquid inclusions, the presence of filler increases the size of the process zone and delocalizes the strain energy in front of a crack tip, thereby increasing the total energy dissipation.[214] Recently, Zhang et. al[215] showed that high energy dissipation can be attributed to the Mullins effect. In their theory, $\Gamma/\Gamma_0 = 1/(1 - \alpha h_{max})$, where h_{max} is the ratio between the energy dissipated and maximum mechanical work being done on the material, and $0 < \alpha < 1$ is a non-dimensional number depending on the stress-strain hysteresis. The maximum enhancement predicted by this theory is around 10×, which is generally in agreement with our results for $\phi \leq$ 40%. However, it severely underpredicts the toughening enhancement of the sample with adaptable crack movement observed at high volume fractions of LM ($\geq$ 50%), which is on the order of 50×. This discrepancy is due to the special role of the elongated liquid inclusions, which guide the crack to move vertically and prevent propagation of the tear across the whole sample. This mechanism is analogous to that in tough bones, where a micro crack starts moving perpendicularly to the loading direction and then twists.[183] Based on the theory by Cook and Gordon, if the interfacial binding energy of LM and polymer is comparable to the cohesion energy, a vertical crack will be initiated that moves perpendicular to the direction of original crack.[216] Accordingly, this secondary crack

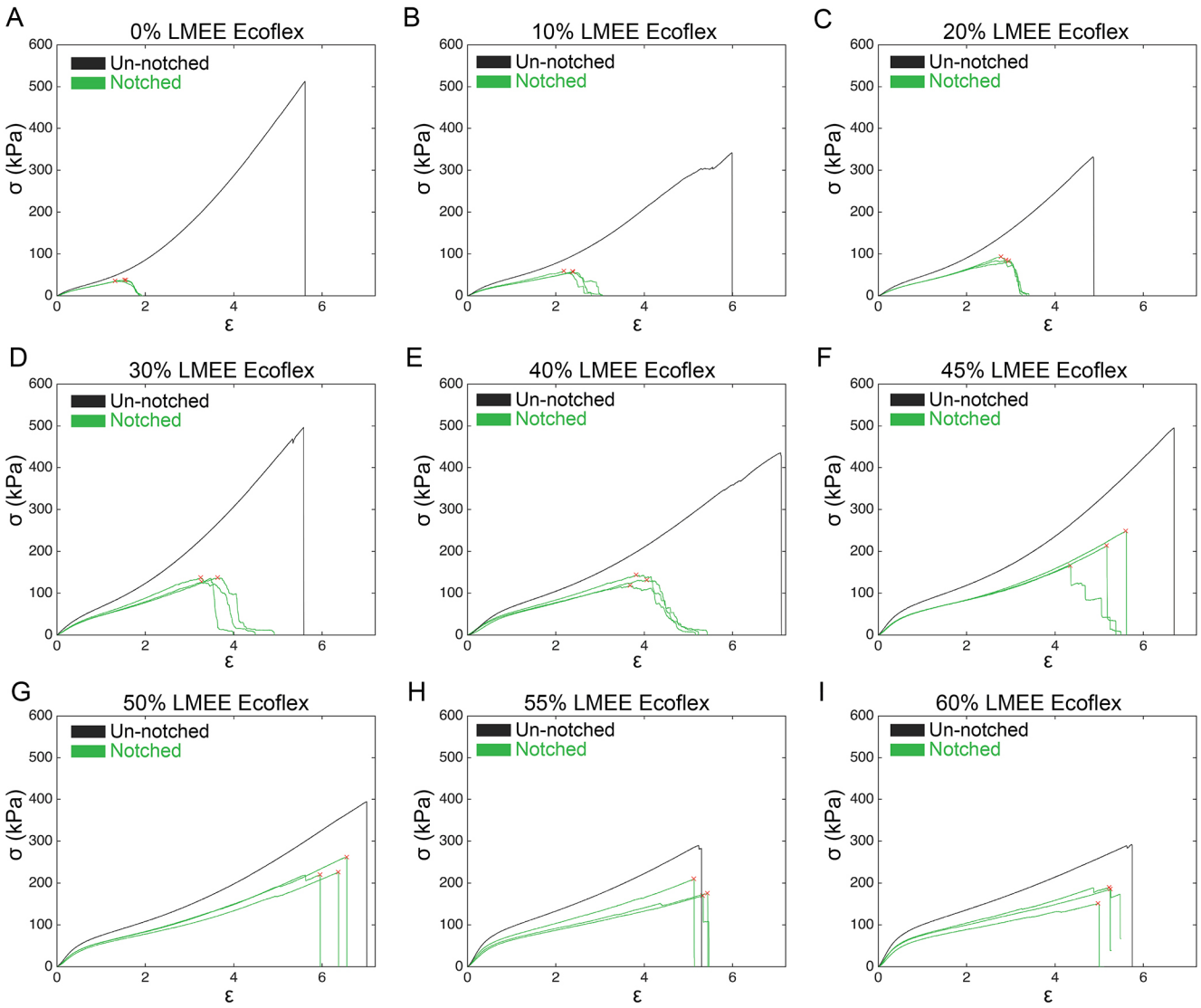

Figure 4.7: Stress vs strain plots for pure shear experiments of LMEE Ecoflex samples with different volume fraction of liquid metal. As mentioned in the manuscript, the sample lengths are 5mm and 10mm for region I ($\phi \leq 40\%$) and region II ($\phi \geq 45\%$), respectively.

greatly decreases the stress concentration in front of the existing crack and results in an increase in the energy dissipation and toughness of the composite. As shown in Fig. 4.4B, I observe an enhancement in fracture energy Γ of up to 50× compared to the host silicone elastomer for Ecoflex LMEE with 50% volume ratio of LM. This additional toughening behavior is not only a result of higher energy dissipation of filler inclusions, but also arises from the geometrical effect of adaptable crack movement. Using a silicone elastomer composite with 50% LM loading and a higher base fracture energy (Dragon Skin 10 slow, $\Gamma_0 = 930 \pm 80\, J/m^2$) I was able to enhance the fracture energy of the composite to $\Gamma = 33,500 \pm 4,300\, J/m^2$ (Fig. 4.4B blue bars and Fig. 4.3). In addition

to achieving ultra toughness, the resistance to tearing is omni-directional in LMEE composites as the inclusions adapt their orientation to the loading direction. This is in contrast to most other engineered or biological tough materials (e.g. fiber reinforced composites and bones), which have anisotropic toughness and resistance against tearing only along certain loading directions. For these materials, the relative angle of the initial crack can have a significant influence on fracture strength. This can be of critical importance in applications where cracks are initiated in random directions.

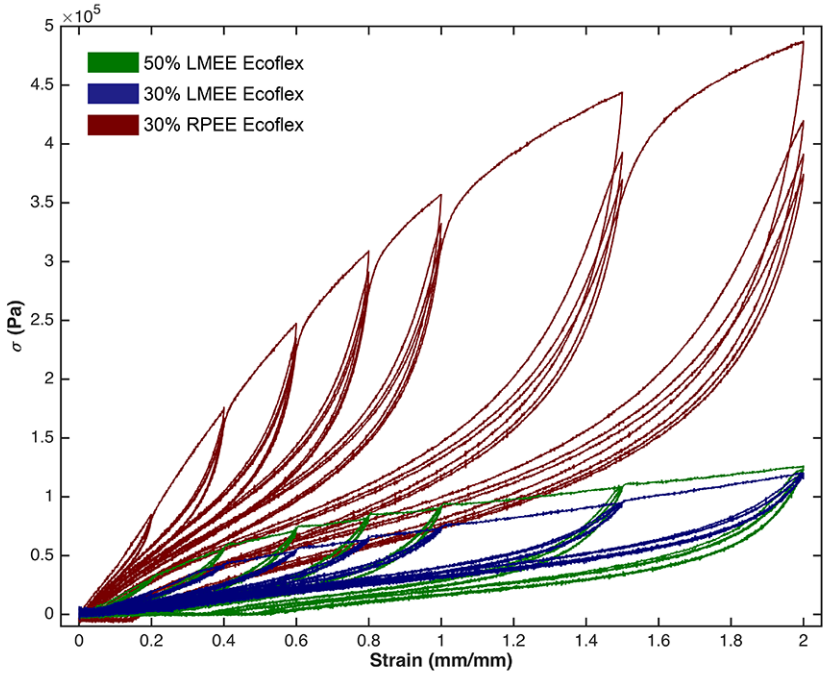

Figure 4.8: Mechanical cyclic (3 cycles) tests with strain steps at 20%, 40%, 60%, 80%, 100%, 150% and 200%. Mullins effect is observable in all three samples of 50% volume fraction LMEE (green), 30% volume fraction LMEE (blue), and 30% volume fraction RPEE.

4.4 Conclusion

In closing, I showed that embedding microscale droplets of liquid metal within a soft elastomer can increase fracture energy by up to 50×. I attribute this significant enhancement to a two-fold mechanism. First, enhancement comes from the conventional mechanical dissipation and Mullins effect that have also been observed in rigid particle-filled elastomers and gels. Based on the theory by Zhang et. al[215], up to 10× increase can be expected for this type of mechanism. The second contribution

to this enhancement comes from the longitudinal crack deflection due to highly dense and elongated LM droplets embedded in a soft elastomer. This Cook-Gordon mechanism for enhancing fracture toughness has been observed previously for tough and hard materials like bones and here, for the first time, I introduce it in soft materials (nearly six orders of magnitude softer than bone). Although previous work in soft DN hydrogels[217] has shown high fracture energies of up to $16,000\, J/m^2$, I am able to achieve even higher toughnesses with LMEE composites (Γ up to 33,000 J/m^2). Significantly, LMEEs also display superior thermal and electrical properties through the functional properties of the liquid metal phase.[137,195,200] This extraordinary combination of properties allows soft elastomers to have a more central role in emerging applications. These include improving the biomechanical compatibility of electronic devices by replacing rigid and brittle materials with soft, stretchable and tear resistant elastomers for applications in wearable computing and soft robotics, where robustness of the device is highly dependent on the tear resistance of the elastomeric materials.

One important question is the extent of temperature that gallium alloys can remain liquid. All of the functionalities that I characterized previously, have been at room temperature; and high deformability of LMs played a crucial role. So, as a natural extension of this work, In the next chapter, I investigate the extent of temperatures in which droplets of low melting point alloys (LMPAs) remain liquid.

Chapter 5

Temperature and Supercooling Effects on Functionality of LMEEs

In the previous chapters, I showed that adding LM inclusions to elastomers significantly enhances dielectric permittivity, thermal conductivity and fracture toughness of soft elastomers without significantly increasing stiffness of the composite. All of these behaviors are characteristics of suspensions of liquid metals inside elastomer. The liquid inclusions can deform and adapt to large background strain field without inducing much resistance against deformation. This is in contrast to rigid inclusions where the mismatch in the modulus of particles and host elastomer creates high stress concentrations and results in large deduction in strain at failure and an increase in the modulus of the composite. However, the extent of temperature in which the micron-sized inclusions' phase remains liquid is not fully understood. In this chapter, I experimentally investigate and characterize the phase change of low melting point alloy (LMPA) droplets inside an elastomer.

It is often challenging to freeze liquid metals at their absolute melting temperature. This is due to the supercooling effect, in which the liquid can be cooled down to temperatures way lower than absolute melting temperature while still remaining liquid. For the solidification to happen, an initial crystal needs to be formed and propagate. The solidification in supercooled liquids can be catalyzed by initiating the crystallization from introducing a defect or embedding another crystalline object (like a piece of metal) as a starting point for crystallization.[218,219] One method of reducing the probability of crystallization in the supercooled metals is to cover the surface of inclusions by a smooth polymer layer. Tevis et. al.[220] reported on a shear mixing technique (Shearing Liquids Into Complex Particles, i.e. SLICE) to produce nano to micron scale droplets of LMPAs inside different solutions and polymers. SLICE is a multi step method in which LMPAs are first segregated into small scale droplets inside a solution with control over its temperature. After washing and filtering the inclusions, they can be embedded into elastomers following another mixing step. Using this technique, inclusions of Field's metals ($T_m \sim 62°C$) can remain liquid at room temperature with a solid shell surrounding them.[221] The room temperature supercooled liquid inclusions of Field's metals have applications in heat-free soldering and stiffness tuning materials.[197,221]

Gallium-rich alloys are also known to experience this supercooling effect,[222]. The droplet sizes can have significant impact on the supercooling temperature as well. As reported by Turnbull[218], the supercooling temperature observed in small droplets with the particle size of $50\mu m$ to absolute

melting temperature is of the order of $\Delta T_{s,max}/T_m \sim 0.2$ (in Kelvin), while in larger droplets this ratio is generally < 0.05. Further reduction in size reduces the supercooling temperature. In the most extreme case reported, Parravicini et. al., studied the crystallization temperature of Ga droplets with particle size of 3-15nm. They reported that these nano-droplets can remain liquid at $T = 90K$ for several days ($\Delta T_{s,max}/T_m \sim 0.7$).[223] These experimental data are consistent with the hypothesis that the probability of finding accidental nucleation points to promote crystallization is much lower in small droplets than larger droplets.[218]

LMEEs can be a model system to investigate many different aspect of supercooling in metals. Similar to SLICE technique, a layer of elastomer covers each liquid droplet (due to high bonding affinity of the oxide skin and polymers) and provides a smooth boundary that further prevents the nucleation of crystallization. Additionally, the simplicity of the fabrication technique allows different types of host matrix to be investigated rapidly. In order to understand different contributions to the supercooled temperature, I use two sets of experiments. First, I perform Differential Scanning Calorimeter (DSC) experiment to identify the supercooling effects of LMPA-embedded elastomers with micron to nanometer particle sizes, in a static state. Next, I use a Dynamic Mechanical Analyzer (RSA-G2) to perform oscillatory tension at a wide temperature range, to identify crystallization and melting point and its influence on mechanical properties of the composites in a dynamical system. These investigations are done for Eutectic gallium indium and Field's metal embedded inside elastomers. In order to understand size dependency of supercooling temperature of LM inside elastomers I perform the experiments for different sizes of inclusions from $\sim$20 μm to hundreds of nanometer.

5.1 Differential Scanning Calorimetry

Differential Scanning Calorimetry (DSC) can be used to identify critical temperatures like melting, crystallization, and glass transition. In DSC, the difference of heat flow (W) required to keep the temperature between a sample pan and a reference pan is measured. The points of crystallization and melting are characterized by exothermal and endothermal peaks in plots of heat flow vs temperature. All tests are performed with samples between 5-16 mg inside of an Al pan and lid (Tzero, TA

Instrument) and temperature ramp of $5°C$/min.

5.1.1 LM and Unfilled Elastomer

In Fig. 5.1a, I plot a representative DSC curves for the Eutectic Gallium Indium (EGaIn). The bulk EGaIn has melting temperature of $T_m = 16.9°C$ which is close with reported values in literature.[106,222] However during the cooling ramp, the bulk EGaIn experiences supercooling effect and an exothermic peak, which is observable at a lower temperature ($T_c \sim -6°C$ for this sample) than T_m. Due to the nature of random nucleation of the crystallization, the supercooling temperature varies for different samples with average and standard deviation of $-26.6 \pm 13°C$ (for 3 samples).

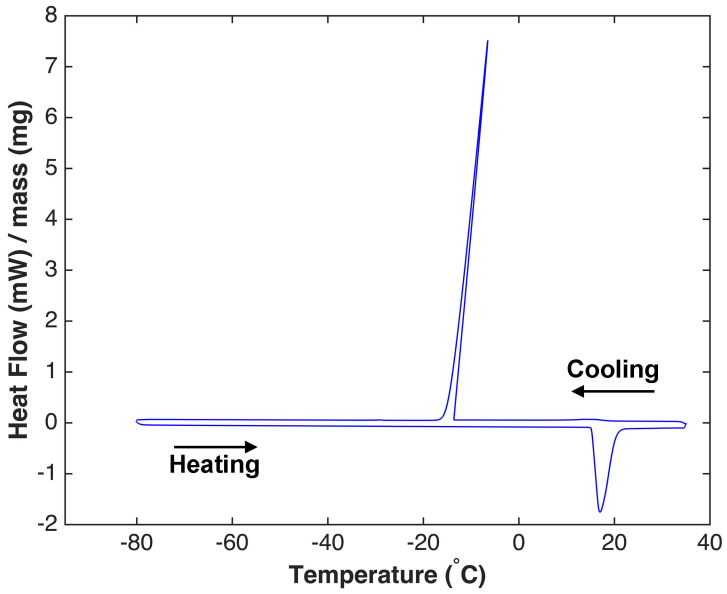

Figure 5.1: A representative plot of Differential Scanning Calorimeter measurement for EGaIn.

I perform DSC measurements on two samples of unfilled Ecoflex 00-30 and plot the curves in Fig. 5.2. As shown, In the cooling ramp I can detect a crystallization point at $T_c \sim -66°C$ for the Ecoflex. Silicone elastomers, like polydimethylsiloxane (PDMS, Ecoflex 00-30), have shown semi-crystallinity behavior where the polymers structure consists of crystalline and amorphous parts. DSC measurements of end-linked polydimethylsiloxane (PDMS) in the literature,[224,225] have shown crystallization points at temperature of $T_c \sim -80°C$ and glass transition of $T_g < -120°C$. Consistent with literature, I observed a crystallization peak at higher temperature than glass transition. I expect

to see the glass transition at lower temperatures, however, temperatures lower than $-90°C$ are not accessible with our current DSC setup. Subsequently in heating ramp, the Ecoflex00-30 melts at $T_m = -41°C$.

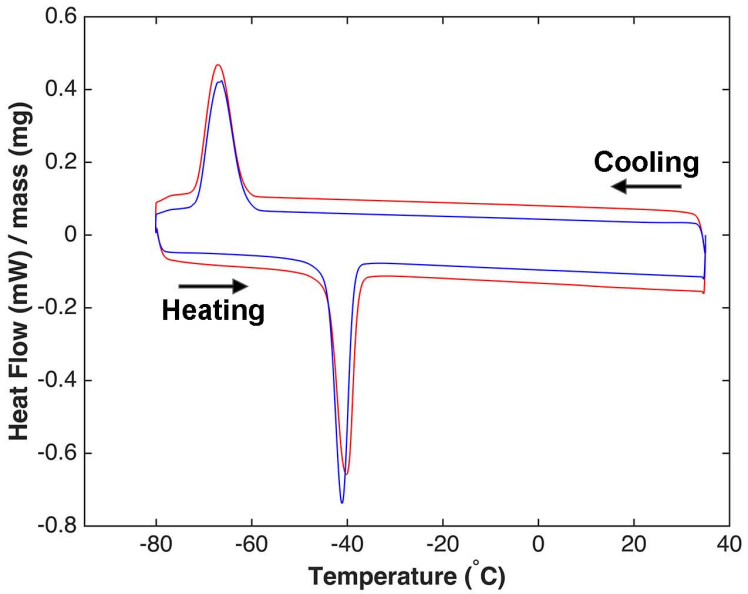

Figure 5.2: Differential Scanning Calorimetry for unfilled Elastomer, Ecoflex 00-30

5.1.2 Liquid Metal Embedded Elstomers

The influence of adding rigid particles on glass transition and crystallization kinetics of silicone elastomer have been investigated before. Bosq et. al.[224] reported that addition of silica nanoparticles inside PDMS does not significantly influence the glass transition of the polymer but does promote initiation of crystallization in the elastomer. Here, I study the crystallization behavior of composites of low melting point alloys embedded inside elastomers. I embed micron size droplets of LM inside ecoflex using shear centrifugal technique. Fig. 5.3 shows the DSC measurement on LMEE composite (red curve) with using Ecoflex 00-30 as the host elastomer and EGaIn as the fillers. Additionally, the DSC curve for unfilled Ecoflex 00-30 (scaled to have similar elastomer mass used in the LMEE sample) is plotted with red line. I see dramatic changes in both crystallization and melting temperature of EGaIn microdroplets. Interestingly, both crystallization and melting temperatures of EGaIn shift to lower temperatures. Since the majority of the microdroplets remain in liquid state (until temperatures

close to the crystallization point of elastomer), their presence do not alter the crystallization point of the elastomer. The onset of exothermic peak starts close to the crystallization temperature of the elastomer at $T_{c,LMEE} = -65°C$. This shows the extreme resistance of micro droplets of liquid metals inside the elastomer against freezing and crystallization.

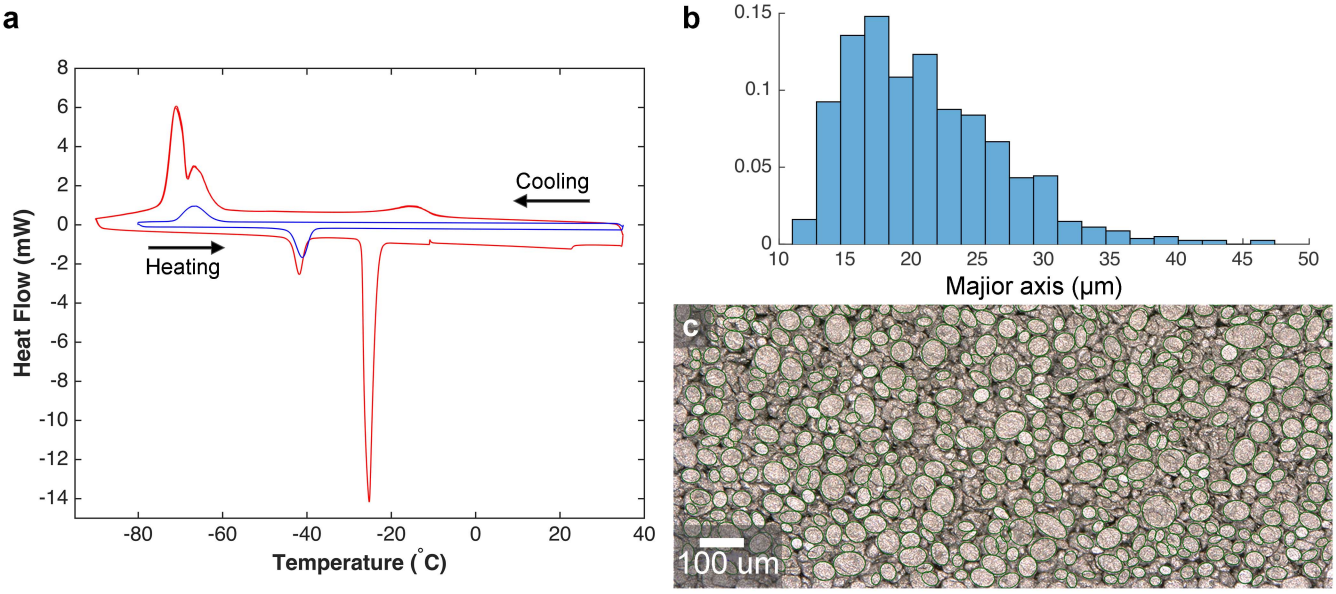

Figure 5.3: a) Differential scanning calorimetry for LMEE with $\phi = 50\%$ in red, and Ecoflex 00-30 in blue. b) Size distribution of LM particles inside the elastomer, and c) optical micrograph of the LMEE composite.

Additionally, the exothermic heat flow has two distinct peaks that show lagging between crystallization of LM droplets. This double peak behavior of crystallization point can be a result overlapping crystallization peaks of the elastomer and LMs microdroplets. Furthermore, during the heating ramp, I see one endothermic peak at $T_{m1} = -41°C$, and another one at $T_{m2} = -25°C$. The first melting peak corresponds to melting of the elastomer, and it is consistent with DSC curve for unfilled Ecoflex 00-30. However, the second melting peak that should be corresponded to melting of EGaIn microparticles occurs at much lower temperatures compared to known melting point of bulk EGaIn which is at $T_{m-EGaIn} = 15.5°C$.

5.1.3 LM Droplets, no Elastomer

To further investigate the supercooling effect of EGaIn, I fabricate the liquid metal droplets using sonication. With the help of my lab-mate Dr. Malakooti, we use a fabrication method suggested by Lt. Col. Carl Thrasher to functionalize the surface of EGaIn particles by polymer brush of 11-phosphonoundecyl acrylate (PUAc, Sigma Aldrich). In this method, we add 200mg EGaIn, 10mg PUAc and 10 mL of EtOH to a 20mL vial. We then bath sonicate the solution for 2 hr at $50°C$ followed by a centrifuging step and replacing the EtOH three times in order to remove any excess PUAc away. Fig 5.4b shows the SEM image of the LM particles. This SEM image shows a wide range of particle sizes ranging from $5\,\mu m$ to $300\,nm$. Most of the particles are spherical with some larger particles that show some irregular shapes. The surface of those particles with irregular shapes are more rough, indicating not a full coverage by the polymer brush. In order to understand the supercooling temperature of these micro-nano particles assembly, I perform DSC measurements with 2 cycles of cooling and heating for this system. As shown in Fig 5.4a, in the cooling curve I first observe a continuous exothermic bump starting from $T \sim -45°C$ followed by a peak at $-60°C$. I subsequently observe additional exothermic crystallization peak with higher magnitude at -85$°C$. During the heating ramp, I see melting peak at $T = -26.5°C$, similar to what was also observed in previous LMEE samples, with the addition of another small peak at $T = -10.7°C$.

5.1.4 LM Droplets, with PPBMA

The droplets that were fabricated with sonication (in the previous section) consist of LMs with wide range of sizes from a few microns to hundreds of nanometer. I hypothesize that the appearance of another crystallization peak at lower temperature ($T = -85°C$) is corresponding to droplets with nanometer scale size ($\sim$ hundreds of nanometer). In order to test this hypothesis, I use a technique to embed highly uniform droplet size of EGaIn inside a polymer brush. By using Atom Transfer Radical Polymerization technique,[226] (with help from Jiajun Yan, Matyjaszewski lab), polymer brush of PBMA are grown on the surface of NPs in which stabilizes them in a gel. As shown in the TEM image (Fig. 5.5), the size of nano-particles are very uniform with average of $125\,nm$. Fig. 5.5c,

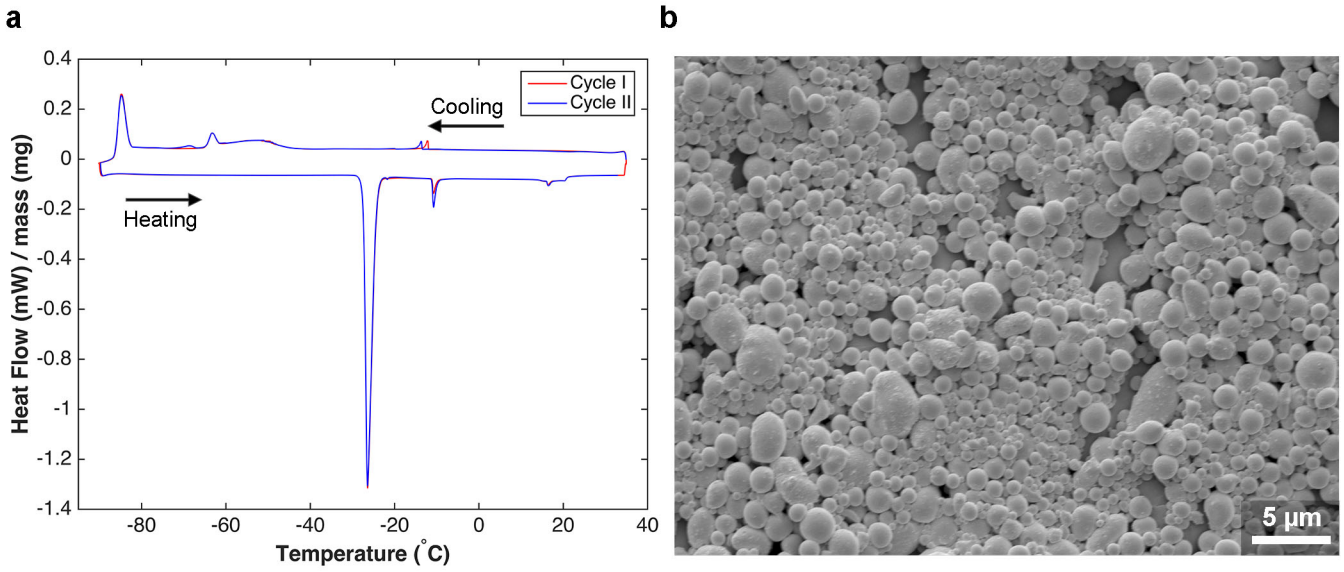

Figure 5.4: a) DSC curves for EGaIn micro-nano droplets (first cycle red and second cycle blue). b) SEM image of the EGaIn droplets

shows the DSC curve of the NP-PBMA and the unfilled PBMA for 2 cycles. The volume fraction of LMs is estimated by TGA to be 8.2 % in this system. In the cooling ramp, the crystallization happens at $T_{c_{NP-gels}} = -85°C$, which is in excellent agreement with second peak of samples with Thrasher's method. Furthermore, the peak previously seen at $T = -65°C$ for systems with larger particle sizes disappears here, indicating the influence of monodispersity of nano-droplets. In the heating ramp, similar to the LMEE sample and LM droplets with Thrasher's methods, I see melting peak at $T = -26.6°C$.

5.1.5 Field's Metals Embedded in Elastomers

As an extension of this work, I replace EGaIn fillers with Field's metals which has higher melting temperature. Since Field's metals also have relatively low melting point, I could use similar shear mixing techniques (mortar and pestle) to get similar morphology with using Field's metals instead of EGaIn. In Fig. 5.6, I have shown DSC measurements for the bulk Field's metals and the composite of Ecoflex and Field's metal with 30% volume fraction of fillers. The Field's metal melts at $T_m = 62°C$ (consistent with literature) and shows a super cooling temperature at $T_c = 58°C$. Furthermore, the DSC curves for 30% volume fraction of Field's metal embedded in Ecoflex shows a decrease in

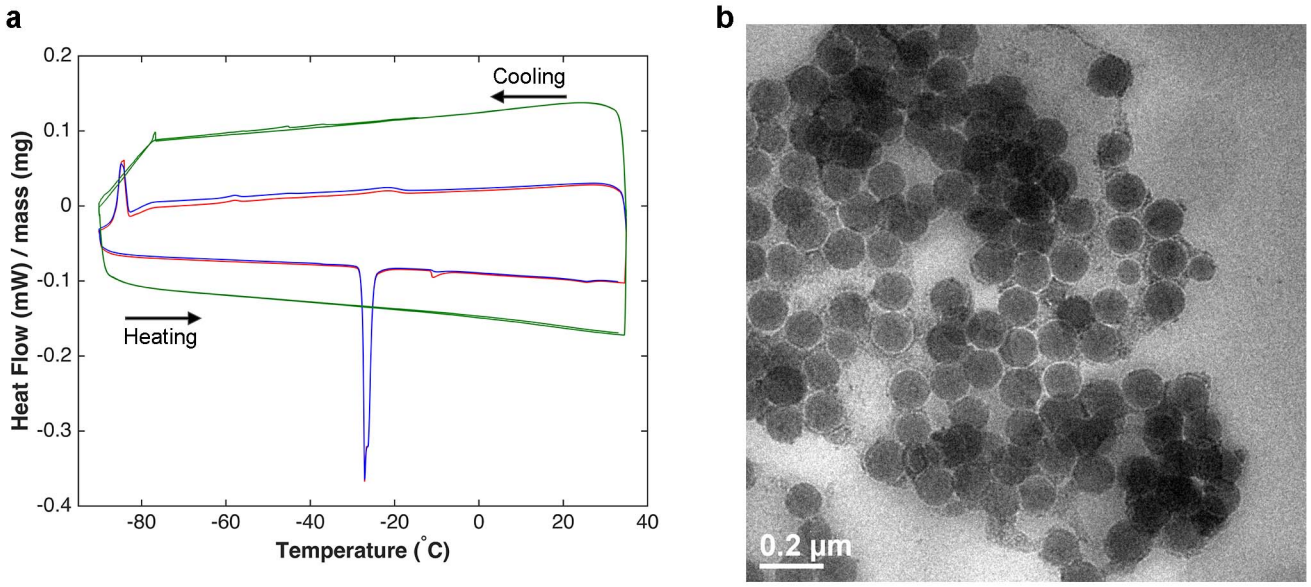

Figure 5.5: EGaIn nano-droplets embedded inside PBMA. a) DSC curves for unfilled PBMA in green and LM-embedded droplets inside PBMA (first cycle red and second cycle blue). b) TEM image of EGaIn nano droplets

crystallization temperature. The crystallization of micro droplets of Field's metals happen at a temperatures between $36°C < T_{c_{RPEE}} < 42°C$. Here, I see emergent of a shoulder in the crystallization peak of RPEEs with Field's metal.

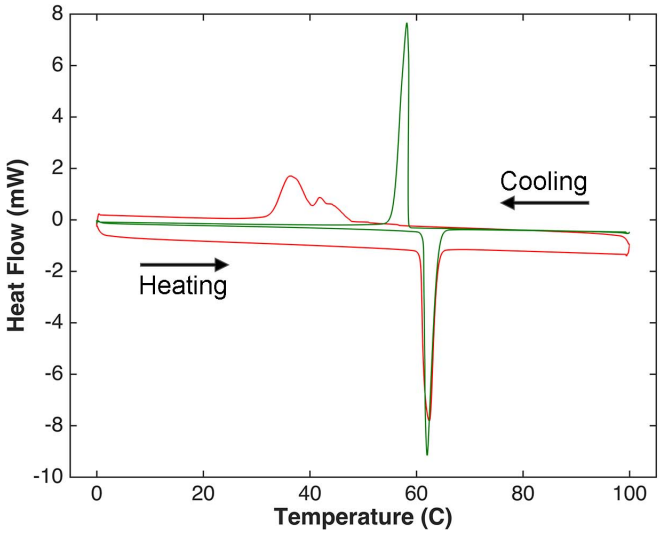

Figure 5.6: Differential scanning calorimetry for Field's metal (in green) and 30% volume fraction of Filed's metal embedded in Ecoflex 00-30 (in red).

In this section, I studied the crystallization of micro and nano scale size droplets of EGaIn and

Field's metals. I showed that at LMEEs, the crystallization occurs at temperatures lower than $-65°C$. This reduction in crystallization temperature comes mainly from the reduction in size of liquid metals. Embedding the micron size droplets inside elastomer would isolate the particles from each other and reduces the chance of crystal nucleation in them. Furthermore by reducing the size of droplets to nano scale with a narrow size distribution, the crystallization peak was pushed further to lower temperatures of $-85°C$. As an important step, in the next section, I study the influence and onset of crystallization of liquid fillers inside elastomers on the mechanical properties of the composites.

5.2 Dynamic Mechanical Analyzer

In order to investigate the mechanical behavior and supercooling transition of LMEEs in a dynamic state, I perform oscillatory tensile test using a Dynamic Mechanical Analyzer (DMA RSA-G2) over a wide temperature range. Using DMA, I obtain storage and loss modulus from dynamic measurements that involve applying sinusoidal deformation and recording corresponding force response. While elastomers can store energy in terms of storage modulus, liquids mostly dissipate energy by turning it into heat.[227] For a general oscillatory compression/tension, the deformation rate tensor becomes:[228]

$$K_{xx} = \dot{\gamma} = \gamma_0 cos(\omega t) \tag{5.2.1}$$

where γ_0 is the strain amplitude, and ω is the frequency of oscillation. The corresponding stress would be a harmonic oscillation with some phase lag ϕ. Taking the Fourier Transform of stress component, we have:

$$\sigma_{xx}^{FT} = \sum_{N}^{\infty} I'_N \, sin(N\omega t) + \sum_{N}^{\infty} I''_N \, cos(N\omega t) \tag{5.2.2}$$

Where the Fourier coefficients, I'_N and I''_N are:

$$I'_N = \frac{\omega}{\pi} \int_{-\frac{\pi}{\omega}}^{\frac{\pi}{\omega}} \sigma_{xx} \, sin(N\omega t) dt \, , \quad I''_N = \frac{\omega}{\pi} \int_{-\frac{\pi}{\omega}}^{\frac{\pi}{\omega}} \sigma_{xx} \, cos(N\omega t) dt \tag{5.2.3}$$

and finally the storage modulus, loss modulus, and phase angle will be:

$$G'_N = \frac{I'_N}{\gamma_0}, \quad G''_N = \frac{I''_N}{\gamma_0}, \quad tan(\phi_N) = \frac{G'_N}{G''_N}. \tag{5.2.4}$$

For linear viscoelastic materials the first mode, $N = 1$, is the dominant mode. However, by going beyond the linear regimes, other modes appear to become more significant. To identify the onset of solidification of LM droplets, I run small strain DMA experiments (linear regime) with strain oscillation of 1%, and a temperature sweep ranging between $-70°C < T < 20°C$ for composites with EGaIn ($T_m = 15.5°C$), and $-40°C < T < 80°C$ for the composites with Field's metals ($T_m = 62°C$) fillers. I chose $T_{min} = -70°C$ due the lowest useful temperature that is recommended for Ecoflex 00-30 (Smooth On). The sample dimensions are $5mm \times 5mm$, with a thickness ranging between 250-300μm.

5.2.1 Results and Discussion

The DMA and DSC measurements can be complimentary to each other, since they can identify similar transitioning points. Peaks in $tan\,\delta$ measurements can be used to identify phase change in DMA measurements. When the sample undergoes internal transitioning and readjustment in arrangement between particles, $tan\,\delta$ (which is the ratio between loss and storage moduli, $tan\,\delta = E''/E'$) becomes maximum.[229] In Fig. 5.7, I plot DMA measurements for LMEE 50% (5.7a), and Ecoflex 30 (5.7b). The storage modulus of LMEE with 50% volume fraction of liquid metals remains constant until temperature drops to $T_{c,LMEE} \sim -65°C$, where I see a sharp increase in the modulus. Consequently in the heating ramp, there are two transitional points. First, the elastomer melts and the storage modulus drops to $\sim 700kPa$. In between melting of Ecoflex and melting of the LM, a portion of the inclusions are rigid and the modulus of the composite is 5× higher than the composite with liquid fillers. This can be used as a direct comparison between the stiffness of a composite with liquid and rigid fillers (even though only $\sim$ 40% of the fillers are rigid according to DSC analysis). Increasing the temperature will initiate melting of EGaIn inclusions and the storage modulus becomes similar to the original values. The phase changes can be identified from the peaks in $tan\,\delta$ measurements. I

identified onset of freezing of LMEE, melting of Ecoflex and melting of EGaIN at $T_{c_{LMEE}} \sim -69°C$, $T_{m_{Ecoflex}} \sim -42°C$, and $T_{m_{EGaIn}} \sim -25°C$, respectively. They are in excellent agreement with DSC data presented in previous section. As a control sample I perform DMA test on the Ecoflex 30. The plot in Fig. 5.7 shows an increase in storage modulus of Ecoflex30 at $\sim -65°C$ in the cooling ramp. Since the modulus of Ecoflex is very low, the measurements for loss modulus is in the range of tens of kPa and hence the $tan\,\delta$ values are noisy, as a consequence, the crystallization of Ecoflex can not be clearly identified in this test. In the heating ramp, storage modulus decreases and $tan\,\delta$ reaches a maximum at $T_{m_{Ecoflex}} = -42°C$. Above the melting point, the storage modulus goes back on top of the the original value before crystallization point and remains similar until room temperature.

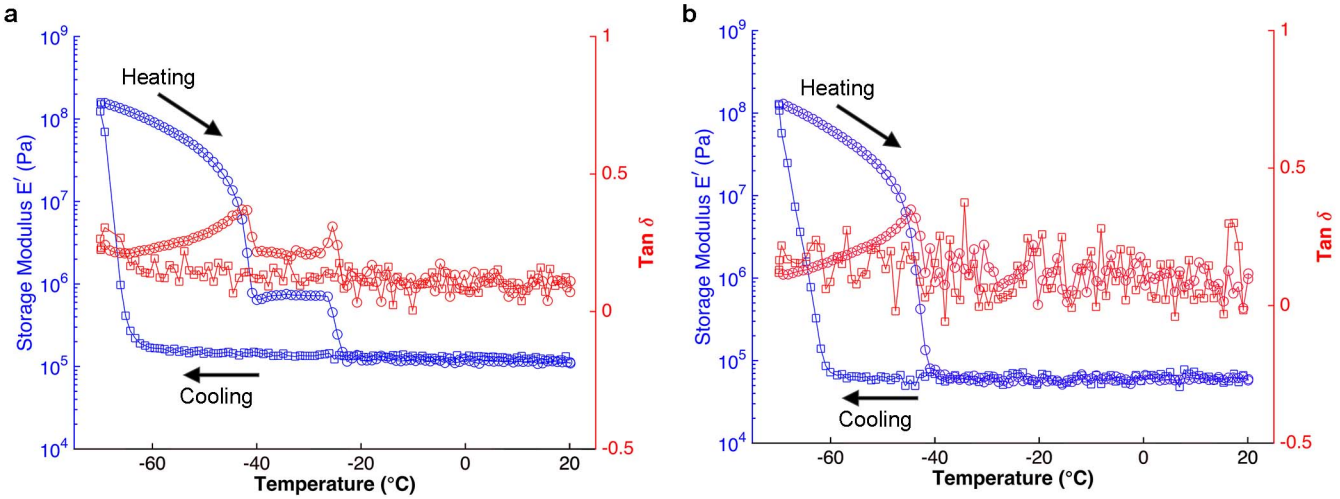

Figure 5.7: Dynamic Mechanical Analyzer measurement for a) a sample with 50% volume fraction of EGaIn embedded inside ecoflex at temperature between $20°C$ and $-70°C$, and b) ecoflex 00-30 at similar temperature range.

By using Field's metal I could decouple the freezing of the fillers from the elastomer. Based on DSC measurements, the melting of Field's metals inside Ecoflex happens at a temperature around $40°C$. In Fig. 5.9, I showed the DMA curves for RPEE and Ecoflex at temperature between -40°C and 80°C. As can be seen in Fig. 5.9b, in this temperature range the Ecoflex doesn't undergo a phase change and the storage modulus and loss modulus remain fairly uniform with a slight increase in storage modulus with increasing temperature. On the other hand, in the first cycle for RPEE, the storage modulus decreases from 3 MPa at $T = -40°C$ to 800 kPa before the melting of Field's metal. This rapid decrease in the storage modulus with increasing temperature could be attributed to the softening of Field's metal inclusions during the heating ramp. At $T = 60°C$, the tan δ reaches

a maximum and storage modulus drops significantly. At this point, the Field's metal inclusions melt and the composite becomes 4× softer. Since the DMA sample is at 40% of initial strain, after the inclusions melt they turn into ellipsoidal shapes (As shown in Fig. 5.8). In the cooling ramp, the storage modulus increases at a temperature of around $40°C$. This increase in the storage modulus could be explained by the crystallization of the Field's metal inclusions. However, the inclusions solidify in the ellipsoidal shapes and the storage modulus doesn't become as high as the first cycle. Mullins effect as well of the influence of ellipsoidal inclusions on the storage modulus of the composite could explain this behavior.

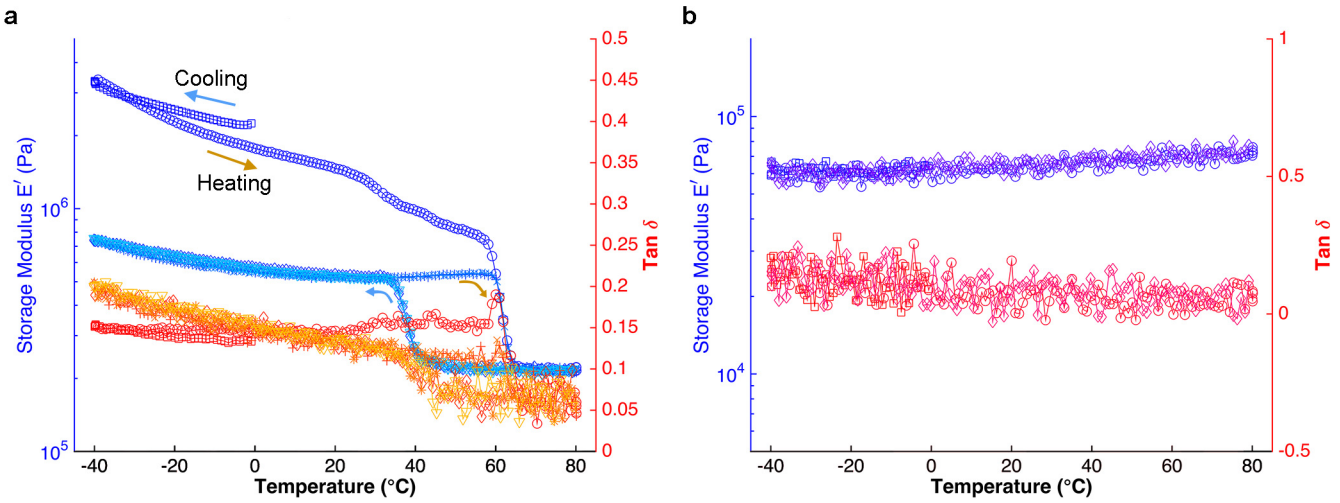

Figure 5.8: Dynamic Mechanical Analyzer measurement for a) a sample with 30% volume fraction of Field's metals embedded inside ecoflex at temperature between $-40°C$ and $80°C$, and b) ecoflex 30 at similar temperature range.

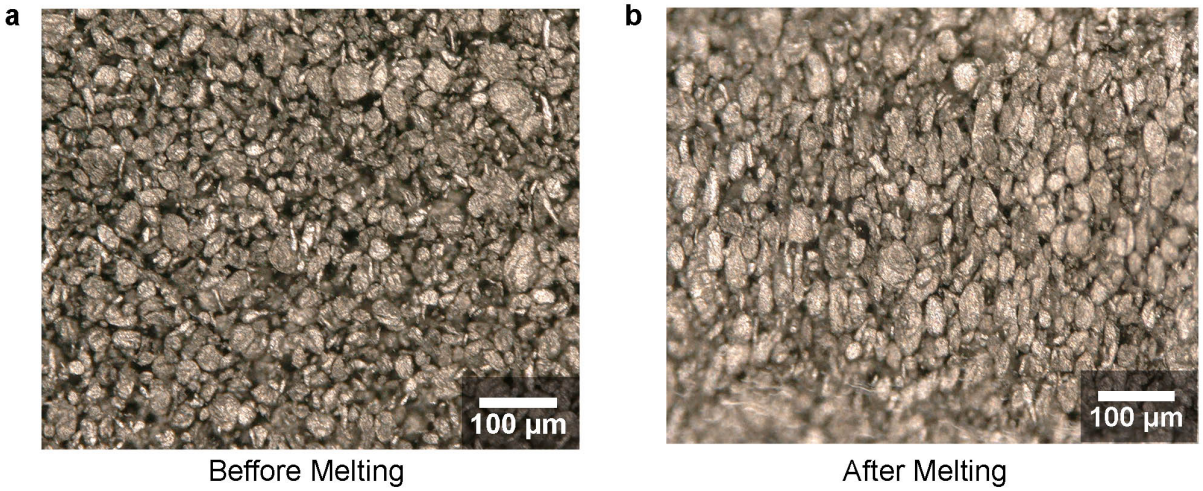

Figure 5.9: Optical image of an RPEE sample with 30% volume fraction of Field's metals a) before and b) after oscillatory tensile test.

5.3 Conclusion

In this chapter, I investigated the extent of temperatures in which micro and nano scale liquid fillers stay in liquid phase inside elastomers. Surprisingly, micro droplets of EGaIn inside elastomer remain liquid above $T = -65°C$. This reduction in freezing of EGaIn particles is due to i) supercooling of the liquid metal ii) micron scale size of the inclusions, and iii) existence of smooth layer of elastomer isolating each liquid inclusion from others. At $T = -65°C$, the crystallization of Ecoflex 30 nucleates crystallization in only about 40% of the droplets. Furthermore, I showed that reduction in size of inclusions will result in further reduction in super cooling temperatures. I observed a melting peak at $T = -85°C$ for EGaIn droplets with 125nm size inside a polymer brush. Similar to EGaIn fillers, I observed a reduction in the crystallization temperature of microdroplets of Field's metals (melting temperature $T_m = 62°C$) inside ecoflex by $25°C$.

Accordingly, the increase in modulus of the composite due to freezing of 40% of inclusions is about $5\times$. Most of the functionalities of LMEEs shown in the previous chapters depends on high deformability of liquid inclusions inside elastomers. Now I have experimental observation of a wide range of temperatures (as low as $-65°C$) in which the composite maintains its material properties. This wide temperature range of functionality can open up new possibilities and applications of LMEEs in extreme environments like space applications.

Chapter 6

Conclusions and Future Research

In closing, for elastomers to play a more active and functional role in the development of machines and devices in the emerging fields of soft robotics, stretchable electronics and human-machine interaction, they must acquire high thermal and electrical functionalities and high toughness without sacrificing their mechanical compliance and stretchability. As summarized in Fig. 6.1, carbon, metals and ceramic oxide have been traditionally used due to their high electric and thermal properties but they lack the compliance and flexibility desired for soft matter applications. Rigid-filled polymer composites can increase the functionality of elastomers but with a deterioration of mechanical performances due to extreme elastic mismatch between fillers and polymers. However, as I showed in this thesis, LMEEs can be engineered to have compliance and stretchability similar to elastomers (Fig 6.1a and b) with an elastic modulus of less than 100 kPa and stretchability of $\sim 600\%$. The high compliance in LMEEs is achieved while at the same time exhibiting a $4\times$ increase in relative permittivity ($\epsilon = 20 - 45$), $\sim 25\times$ increase in thermal conductivity (4.7 ± 0.2 W/mK) under stress-free conditions and a $\sim 50\times$ increase in thermal conductivity (9.8 ± 0.8 W/mK) when strained, over the base polymer.

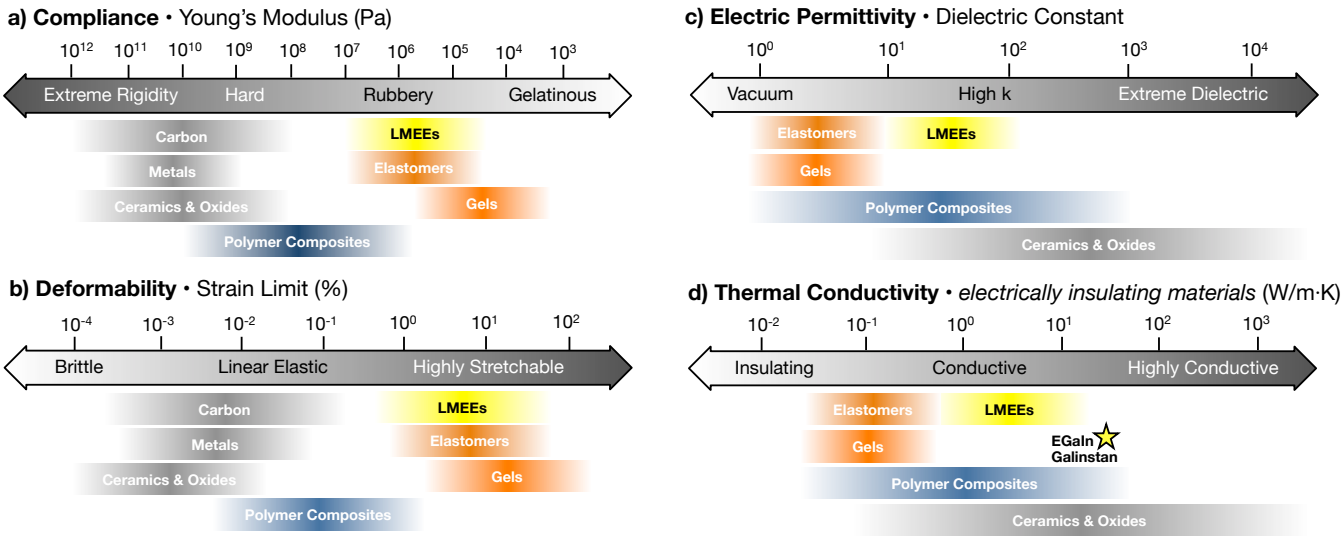

Figure 6.1: Comparison of LMEE composites with other materials' properties

To quantitively understand the increase in dielectric and thermal properties of the composites, I used Effective Medium Theories. With the use of Maxwell-Garnett or Nan et al (for ellipsoidal inclusions) I was able to capture the dielectric behavior of composites. Bruggeman approximation made a significant improvement over Maxwell-Garnett to capture the behavior at larger concentrations. Following Sen et al. (35), I use a self-consistent EMT that takes into account the shape of the ellip-

soidal particles. Using this equation $\frac{k_c - k_m}{Lk_c + (1-L)k_m} = \phi \frac{k_p - k_m}{Lk_m}$, I was able to capture thermo-mechanical coupling in LMEEs with no data fitting.

In addition to increasing the electrical and thermal properties of elastomer, I showed that embedding micro-droplets of liquid metals increases the fracture energy of silicone elastomers by up to 50x (from $250 \pm 50\, J/m^2$ to $11,900 \pm 2,600\, J/m^2$) over an unfilled polymer. For some LM-embedded elastomer (LMEE) compositions, the toughness is measured to be as high as $33,500 \pm 4,300\, J/m^2$, which far exceeds the highest value previously reported for a soft elastic material. This enhancement in toughness is possible due to i) increase in dissipation energy, ii) adaptive crack movement and iii) effective elimination of the crack tip. Micro droplets of EGaIn in their elongated state, can provide a preferred crack movement along the LM and elastomer interface. This results in tear movement along the loading direction and virtual elimination of crack, hencem causing a significant energy dissipation before a catastrophic failure.

The adaptive deformation of liquid metals inside elastomers is the key advantage of them in comparison with embedding rigid fillers. I showed that micro droplets of eutectic gallium indium (EGaIn) inside elastomers can remain in liquid state about $80°C$ lower than their melting temperature ($T_m = 15.5°C$). The LMEE with Ecoflex 30 has a crystallization point at $\sim -65°C$, makes it suitable for applications in extreme temperatures like space suits and ETC.

6.1 Recommendation For Future Research

LMEEs have shown very promising properties and are poised to have huge impact not only in emerging fields like soft robotics and flexible electronics, but also on the traditional electronics and automotive industries. They can be used as thermal interface materials between the heat sink and high heat generating chips (i.e CPUs, GPUs and etc.) where high compliance and high thermal conductivity is highly desired to have low heat resistance interfaces. However, there are still remaining questions to be answered that can make LMEEs suitable for industrial applications. Additionally, other research directions are proposed here to understand LMEEs in more details and improve the current design. Furthermore LMEEs can be used as a model system to make future discoveries in

material science and chemistry.

6.1.1 Influences of Oxide Skin and Surface Tension on Mechanical Properties of LMEEs

In Fig. 6.2, Equation 2.5.1 from Style et. al.[138] is plotted (in blue) and compared with experimentally measured values for elastic modulus of LMEEs after the training steps described in Sec. 2.5.1. In the Style et. al. formulation the influence of surface tension of liquid inclusions is included in the overall mechanical properties of soft solids with liquid inclusions. Here, the surface tension of the inclusions is assumed to be $\gamma = 620\,mN/m$, and the elastic modulus of the unfilled elastomer is $E_0 = 75\,kPa$. As shown here, droplet size have a significant influence on the predicted elastic modulus in Style et. al. formulation. Our experimental data falls in between predicted values from Style et. al for droplet radii between $5 - 10\,\mu m$. This model is representative of liquid inclusions without taking into account the oxide skin. However, during the shear mixing of LMEEs in an oxygenated environment, oxide layer Ga_2O_3 forms on the LMs. Khan et. al.[83] reported that formation of oxide skin reduces the surface tension of liquid metal to virtually zero value. Hence, assuming that the oxide skin significantly reduces the surface tension, application of the Style et. al. formulation becomes less relevant in this system. Alternatively, using Eshelby theory for liquid inclusions with infinite bulk modulus and zero shear modulus will result into reduction in the elastic modulus, as shown in Fig. 6.2 (in red). As shown in the figure, Style et. al. and Eshelby theory could be two limiting cases for the LMEE composites. The elastic oxide layer with a surface yield stress of $\sigma_s = 500\,mN/m$[106] can be an important factor that must be considered in future research projects to better understand the influence of LMs on mechanical properties of LMEEs. Furthermore, in future research projects, the influence of oxide skin on fracture toughness of LMEEs can be further investigated by performing fracture experiments in an oxygen-free environment. Experimentally this influence can be investigated by preparing LMEE samples inside a glove-box and subsequently performing the pure shear test without existence of oxygen in the chamber.

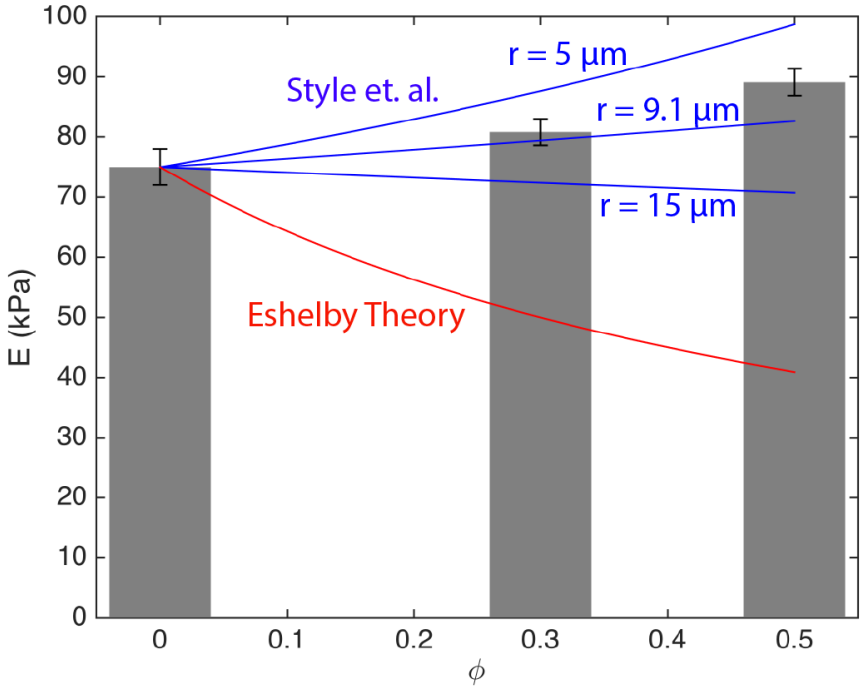

Figure 6.2: Comparison between experimental measurements for elastic modulus of LMEEs (in grey), prediction of Style et. al. for a composite of soft solids and liquid inclusions with high surface tension ($\gamma = 620\,mN/m$ and $E_0 = 75\,kPa$, in blue), and Eshelby Theory (in red)

6.1.2 Programmable LMEE for High Thermal Conductivity Through Thickness

The shape programmability of liquid metals inside elastomers offers a wide range of possibilities for tuning anisotropic behaviors in elastomers. I showed that by stretching LMEEs up to 600% strain and inducing plastic deformation I was able to elongate liquid inclusions in stress-free state. However, there is more that can be done to program the geometry of liquid inclusions inside LMEEs.

In order to achieve high thermal conductivity through thickness, I could attempt to elongate the inclusions along the thickness. In order to get the highest elongation of liquid inclusions, the stretching of LMEEs should be done while the elastomer is curing. The elongation should be done in between the cross linking process where elastomers have just enough integrity to elongate the inclusion but still large portion of cross linking would happen in the later stages where the inclusions have already formed ellipsoidal shape. This procedure could significantly increase the elongation of particles in stress-free state. By using an Instron with an environmental chamber (as sketched in

Fig. 6.3), one could optimize the temperature profile, rate of elongation and maximum displacement to achieve highest elongation of LMs inside elastomers.

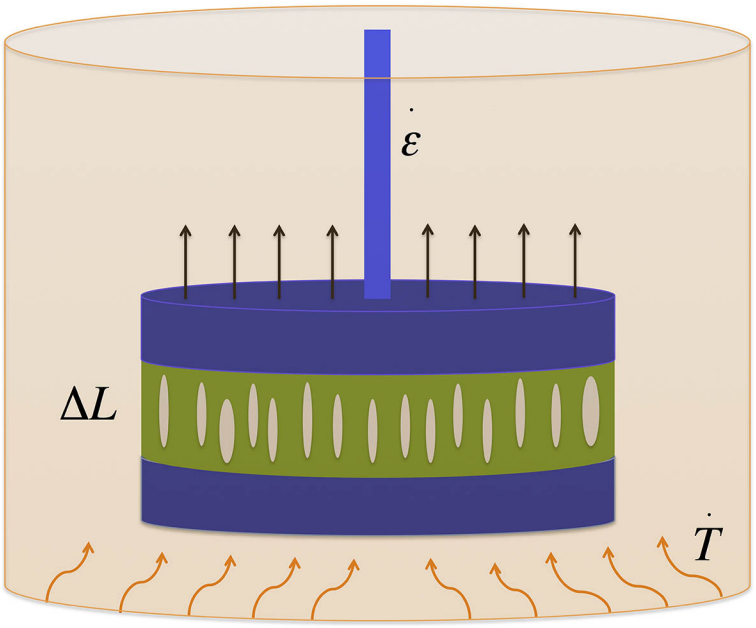

Figure 6.3: A method to program LM shapes inside elastomer, by tuning temperature ramp, strain rate and maximum deformation.

6.1.3 Embedding Nanoparticles of EGaIn Inside Elastomers and Its Implications

A current limitation in fabrication of LMEEs is how to reliably achieving small particle size of the liquid metals embedded inside elastomers. I have achieved up to $\sim 5\mu m$ particles size with a distribution of a few tens of μm. A future research could be on developing fabrication techniques in order to achieve mono-dispersed LM particles with small radius (hundreds of nanometers).

Fabrication

A popular method to fabricate nano droplets of EGaIn is to use a sonication technique. There have been a few publications on how to stabilize the nano droplets with small size distribution.[121] ethanol has shown to be the most effective solution to disperse and stabilize the nano-droplets. However it is challenging to get high concentration of nanoparticles.[230] Additionally the next step would be

developing a method to get highly efficient nanodroplet of EGaIn embedded inside elastomers. There are some scientifically interesting questions that could be attacked by embedding nanodroplets inside elastomers. In the next 3 sections, I am going to try my best to paint the picture of what would encourage (or maybe discourage) researchers to attack this challenge.

Mechanical Behavior

The ability to embed nano-droplets of EGaIn inside elastomers can open up very interesting ways of controlling the nano structure and assembly of nano-droplets. By Using Atom Transfer Rapid Polymerization (ATRP)[226], it is possible to carefully make polymer brushes to control the nanostructure of LMEEs and program the assembly. Through this technique, the possibility of designing anisotropic composite with interesting properties in different direction worth pursuing.

However, due to the effect of surface tension on deformation of liquid droplets, smaller particles would induce higher stiffening effects than larger droplets. As seen in Fig. 6.4, particles with 10 nm size distribution would behave $\sim 5\times$ stiffer than particles with $10\mu m$ size (LMEEs with currently available technique). This could be a discouragement for pursuing this fabrication technique if the desired application is in the soft matter space.

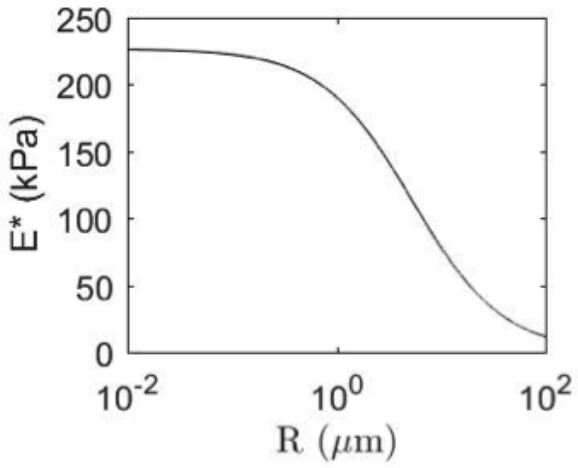

Figure 6.4: Theoretical prediction for dependence of effective modulus of inclusions (E^*) on droplet radius (R) for $E = 85\,kPa$ and $\gamma = 0.5\,N/m$. The prediction is based on a theory reported in Style et al.[138]

Dielectric Constant and Voltage Breakdown

Inclusions of micro droplets of liquid metals inside elastomer increases the dielectric constant of the composite by 4 fold. However this increase comes with a price of reducing the voltage breakdown from 16 KV/mm to ∼1 KV/mm. For applications in dielectric elastomer actuation and energy harvesting, the combination of high compliance, high dielectric constant and high voltage breakdown is required. In this work, the dielectric measurements was done with a LMEE sample fabricated using pestle and mortar. In this fabrication method the shape of particles are highly irregular with high fraction of particles with sharp edges. When voltage is being applied on a LMEE layer, charge can build up more on the sharp edges and cause lower voltage breakdown. A hypothesis (to be checked in future) is that by having nano-droplets with highly rounded shapes and uniform structure could improve the voltage breakdown. However there is a trade of in reducing the particle size if the LMs, in which the surface to volume ratio increases and consequently voltage breakdown can go down.

In closing, even though fabrication of LM nano-particles and embedding them inside elastomers is scientifically interesting and intriguing, there are competing effects in order to get highly desirable properties for soft matter applications. However as a curious scientist, I believe these investigation must be pursued.

6.1.4 System Integration of LMEEs with Soft Electronics

The next challenge, that will constitute a larger set of parameters, is the integration of soft, stretchable, and multifunctional materials with current existing sensing, actuation and computing elements to build a fully functional soft devices. Accomplishing this requires innovation in design guidelines, system integration and synthetic techniques. A proposed device that includes a multilayer design composed of a heat management layer, active layer and an electronics layer is illustrated in Fig. 6.5a.

- **Layer 1 - Sensing, control, and power regulation** consists of flexible electronics rapidly developing in the last decade.[234] Some of the great work here include wavy and serpentine electronics from John Rogers group,[37] Liquid metal and silver paste conductive electronics.[231]

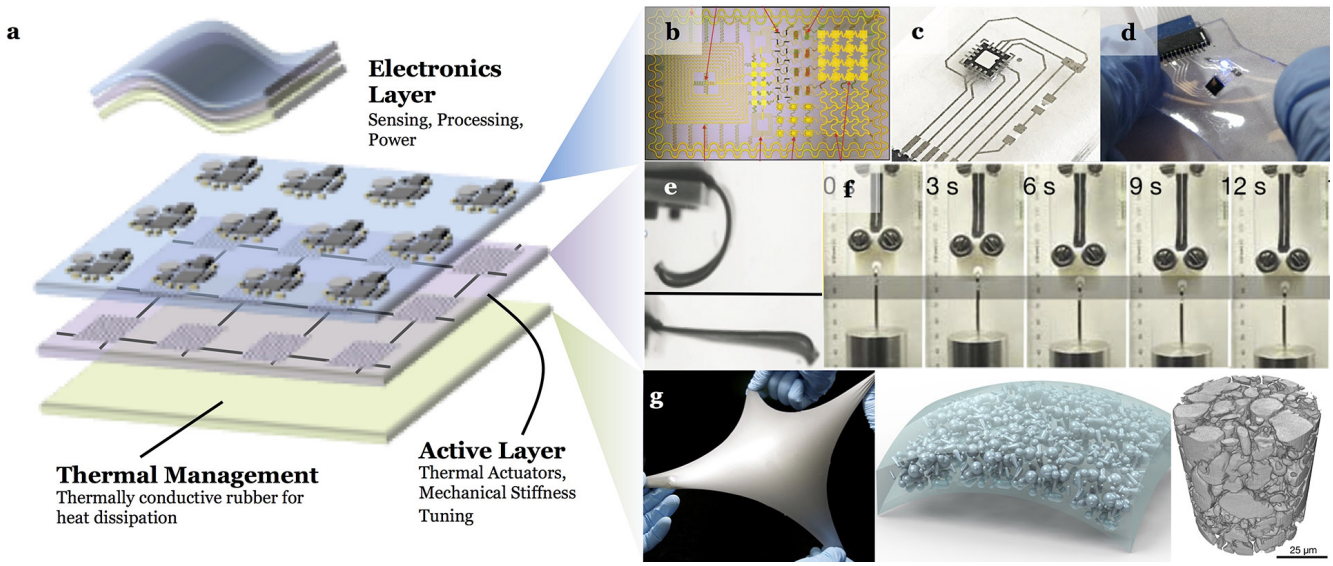

Figure 6.5: a) Proposed robotic material composed of three functional layers: electronics with b) wavy electronics[37] or c,d) LM microfluidics[231]; actuation and stiffness tuning with e) shape memory alloys or f) conductive thermoplastic elastomers[232,233]; heat management with g) LMEEs, which is composed of LM microdroplets embedded in a soft silicone rubber.

- **Layer 2 - Actuation and stiffness tuning** materials that change shape and/or stiffness in response to electrically powered Joule (Ohmic) heating; these will be composed of some combination of shape memory alloy (SMA; Fig. 6.5e), or conductive thermoplastic elastomers (Fig. 6.5f[232,233])

- **Layer 3 - Heat management** thermally conductive rubber ("LMEE") composite (Fig. 6.5g) that will spread and dissipate heat generated by the shape/stiffness-tuning elements in Layer 2; by simultaneously matching the compliance of soft silicone and the thermal conductivity of metals like stainless steel, the LMEE has the unique ability to manage heat without introducing mechanical stiffness.

Bibliography

[1] C. Majidi, "Soft robotics: a perspective – current trends and prospects for the future," *Soft Robotics*, vol. 1, no. 1, pp. 5–11, 2014.

[2] G. M. Whitesides, "Soft Robotics," *Angewandte Chemie International Edition*, pp. 2–18, 2018.

[3] S. Liang, Y. Li, Y. Chen, J. Yang, T. Zhu, D. Zhu, C. He, Y. Liu, S. Handschuh-Wang, and X. Zhou, "Liquid metal sponges for mechanically durable, all-soft, electrical conductors," *J. Mater. Chem. C*, vol. 5, no. 7, pp. 1586–1590, 2017.

[4] J. Park, S. Wang, M. Li, C. Ahn, J. K. Hyun, D. S. Kim, D. K. Kim, J. A. Rogers, Y. Huang, and S. Jeon, "Three-dimensional nanonetworks for giant stretchability in dielectrics and conductors," *Nature Communications*, vol. 3, no. May, p. 916, 2012.

[5] H. Stoyanov, M. Kollosche, S. Risse, D. N. McCarthy, and G. Kofod, "Elastic block copolymer nanocomposites with controlled interfacial interactions for artificial muscles with direct voltage control," *Soft Matter*, vol. 7, no. 1, pp. 194–202, 2011.

[6] J. A. Rogers, T. Someya, and Y. Huang, "Materials and Mechanics for Stretchable Electronics," *Science*, vol. 327, no. 5973, pp. 1603–1607, 2010.

[7] M. L. Hammock, A. Chortos, B. C. K. Tee, J. B. H. Tok, and Z. Bao, "25th anniversary article: The evolution of electronic skin (E-Skin): A brief history, design considerations, and recent progress," *Advanced Materials*, vol. 25, no. 42, pp. 5997–6038, 2013.

[8] M. A. Unger, H.-P. Chou, T. Thorsen, A. Scherer, and S. R. Quake, "Monolithic microfabricated valves and pumps by multilayer soft lithography," *Science*, vol. 288, no. 5463, pp. 113–116, 2000.

[9] J. C. McDonald and G. M. Whitesides, "Poly (dimethylsiloxane) as a material for fabricating microfluidic devices," *Accounts of chemical research*, vol. 35, no. 7, pp. 491–499, 2002.

[10] A. C. Siegel, D. A. Bruzewicz, D. B. Weibel, and G. M. Whitesides, "Microsolidics: Fabrication of three-dimensional metallic microstructures in poly(dimethylsiloxane)," *Advanced Materials*, vol. 19, no. 5, pp. 727–733, 2007.

[11] J. C. Halbur, R. P. Padbury, and J. S. Jur, "Silver decorated polymer supported semiconductor thin films by UV aided metalized laser printing," *Journal of Vacuum Science & Technology A: Vacuum, Surfaces, and Films*, vol. 34, no. 3, p. 031402, 2016.

[12] S. W. Thomas, G. D. Joly, and T. M. Swager, "Chemical sensors based on amplifying fluorescent conjugated polymers," *Chemical Reviews*, vol. 107, no. 4, pp. 1339–1386, 2007.

[13] J. Pecher and S. Mecking, "Nanoparticles of conjugated polymers," *Chemical Reviews*, vol. 110, no. 10, pp. 6260–6279, 2010.

[14] S. Günes, H. Neugebauer, and N. Sariciftci, "Conjugated polymer-based organic solar cells," *Chemical Reviews*, vol. 107, no. 4, pp. 1324–1338, 2007.

[15] A. C. Grimsdale, K. L. Chan, R. E. Martin, P. G. Jokisz, and A. B. Holmes, "Synthesis of light-emitting conjugated polymers for applications in electroluminescent devices," *Chemical Reviews*, vol. 109, no. 3, pp. 897–1091, 2009.

[16] C. A. Junwu and C. Yong, "Development of novel conjugated donor polymers for high-efficiency bulk-heterojunction photovoltaic devices," *Accounts of Chemical Research*, vol. 42, no. 11, pp. 1709–1718, 2009.

[17] G.-H. Kim, D. Lee, A. Shanker, L. Shao, M. S. Kwon, D. Gidley, J. Kim, and K. P. Pipe, "High thermal conductivity in amorphous polymer blends by engineered interchain interactions.," *Nature materials*, vol. 14, no. 3, pp. 295–300, 2015.

[18] Y. Xia and Yun Lu, "Fabrication and properties of conductive conjugated polymers/silk fibroin composite fibers," *Composites Science and Technology*, vol. 68, no. 6, pp. 1471–1479, 2008.

[19] X. Z. Niu, S. L. Peng, L. Y. Liu, W. J. Wen, and P. Sheng, "Characterizing and patterning of PDMS-based conducting composites," *Advanced Materials*, vol. 19, no. 18, pp. 2682–2686, 2007.

[20] M. Maiti, M. Bhattacharya, and A. K. Bhowmick, "Elastomer nanocomposites," *Rubber Chemistry and Technology*, vol. 81, no. 3, pp. 384–469, 2008.

[21] Z. Fan, J. C. Ho, T. Takahashi, R. Yerushalmi, K. Takei, A. C. Ford, Y. L. Chueh, and A. Javey, "Toward the Development of Printable Nanowire Electronics and Sensors," *Advanced Materials*, vol. 21, no. 37, pp. 3730–3743, 2009.

[22] Y. Sun and J. A. Rogers, "Inorganic semiconductors for flexible electronics," *Advanced Materials*, vol. 19, no. 15, pp. 1897–1916, 2007.

[23] W. Bauhofer and J. Z. Kovacs, "A review and analysis of electrical percolation in carbon nanotube polymer composites," *Composites Science and Technology*, vol. 69, no. 10, pp. 1486–1498, 2009.

[24] A. Khosla and B. L. Gray, "Preparation, characterization and micromolding of multi-walled carbon nanotube polydimethylsiloxane conducting nanocomposite polymer," *Materials Letters*, vol. 63, no. 13-14, pp. 1203–1206, 2009.

[25] P. Lee, J. Lee, H. Lee, J. Yeo, S. Hong, K. H. Nam, D. Lee, S. S. Lee, and S. H. Ko, "Highly stretchable and highly conductive metal electrode by very long metal nanowire percolation network," *Advanced Materials*, vol. 24, no. 25, pp. 3326–3332, 2012.

[26] M. B. Bryning, D. E. Milkie, M. F. Islam, L. A. Hough, J. M. Kikkawa, and A. G. Yodh, "Carbon nanotube aerogels," *Advanced Materials*, vol. 19, no. 5, pp. 661–664, 2007.

[27] S. M. Jung, H. Y. Jung, M. S. Dresselhaus, Y. J. Jung, and J. Kong, "A facile route for 3d aerogels from nanostructured 1d and 2d materials," *Scientific reports*, vol. 2, p. 849, 2012.

[28] N. Kazem, C. Majidi, and C. E. Maloney, "Gelation and mechanical response of patchy rods," *Soft Matter*, vol. 11, pp. 7877–7887, 2015.

[29] D.-Y. Khang, H. Jiang, Y. Huang, and J. A. Rogers, "A Stretchable Form of Single-Crystal," *Science*, vol. 311, no. January, pp. 208–212, 2006.

[30] D.-H. Kim, J.-H. Ahn, W. M. Choi, H.-S. Kim, T.-H. Kim, J. Song, Y. Y. Huang, Z. Liu, C. Lu, and J. A. Rogers, "Stretchable and Foldable Silicon Integrated Circuits," *Science*, vol. 320, pp. 507 LP – 511, apr 2008.

[31] H. C. Ko, M. P. Stoykovich, J. Song, V. Malyarchuk, W. M. Choi, C. J. Yu, J. B. Geddes 3rd, J. Xiao, S. Wang, Y. Huang, and J. A. Rogers, "A hemispherical electronic eye camera based on compressible silicon optoelectronics," *Nature*, vol. 454, no. 7205, pp. 748–753, 2008.

[32] H. C. Ko, G. Shin, S. Wang, M. P. Stoykovich, J. W. Lee, D. H. Kim, J. S. Ha, Y. Huang, K. C. Hwang, and J. A. Rogers, "Curvilinear electronics formed using silicon membrane circuits and elastomeric transfer elements," *Small*, vol. 5, no. 23, pp. 2703–2709, 2009.

[33] S.-I. Park, Y. Xiong, R.-H. Kim, P. Elvikis, M. Meitl, D.-H. Kim, J. Wu, J. Yoon, C.-J. Yu, Z. Liu, Y. Huang, K.-c. Hwang, P. Ferreira, X. Li, K. Choquette, and J. A. Rogers, "Printed Assemblies of Inorganic Light-Emitting Diodes for Deformable and Semitransparent Displays," *Science*, vol. 325, no. 5943, pp. 977 LP – 981, 2009.

[34] D.-H. Kim, J. Viventi, J. J. Amsden, J. Xiao, L. Vigeland, Y.-S. Kim, J. A. Blanco, B. Panilaitis, E. S. Frechette, D. Contreras, D. L. Kaplan, F. G. Omenetto, Y. Huang, K.-C. Hwang, M. R. Zakin, B. Litt, and J. A. Rogers, "Dissolvable films of silk fibroin for ultrathin conformal bio-integrated electronics," *Nature Materials*, vol. 9, no. 6, pp. 511–517, 2010.

[35] R.-H. Kim, D.-H. Kim, J. Xiao, B. H. Kim, S.-I. Park, B. Panilaitis, R. Ghaffari, J. Yao, M. Li, Z. Liu, V. Malyarchuk, D. G. Kim, A.-P. Le, R. G. Nuzzo, D. L. Kaplan, F. G. Omenetto, Y. Huang, Z. Kang, and J. A. Rogers, "Waterproof AlInGaP optoelectronics on stretchable substrates with applications in biomedicine and robotics," *Nature materials*, vol. 9, no. 11, pp. 929–37, 2010.

[36] D.-H. Kim, N. Lu, R. Ghaffari, Y.-S. Kim, S. P. Lee, L. Xu, J. Wu, R.-H. Kim, J. Song, Z. Liu, J. Viventi, B. de Graff, B. Elolampi, M. Mansour, M. J. Slepian, S. Hwang, J. D. Moss, S.-M.

Won, Y. Huang, B. Litt, and J. A. Rogers, "Materials for multifunctional balloon catheters with capabilities in cardiac electrophysiological mapping and ablation therapy," *Nature materials*, vol. 10, no. 4, pp. 316–23, 2011.

[37] H. Keum, M. Mccormick, P. Liu, Y.-W. Zhang, and F. G. Omenetto, "Epidermal Electronics," *Science*, vol. 333, no. September, pp. 838–844, 2011.

[38] I. Jung, J. Xiao, V. Malyarchuk, C. Lu, M. Li, Z. Liu, J. Yoon, Y. Huang, and J. A. Rogers, "Dynamically tunable hemispherical electronic eye camera system with adjustable zoom capability.," *Proceedings of the National Academy of Sciences of the United States of America*, vol. 108, no. 5, pp. 1788–93, 2011.

[39] S. Xu, Y. Zhang, J. Cho, J. Lee, X. Huang, L. Jia, J. a. Fan, Y. Su, J. Su, H. Zhang, H. Cheng, B. Lu, C. Yu, C. Chuang, T.-I. Kim, T. Song, K. Shigeta, S. Kang, C. Dagdeviren, I. Petrov, P. V. Braun, Y. Huang, U. Paik, and J. A. Rogers, "Stretchable batteries with self-similar serpentine interconnects and integrated wireless recharging systems.," *Nature communications*, vol. 4, p. 1543, 2013.

[40] S. Cheng and Z. Wu, "Microfluidic stretchable RF electronics.," *Lab on a Chip*, vol. 10, no. 23, pp. 3227–3234, 2010.

[41] H. J. Koo, J. H. So, M. D. Dickey, and O. D. Velev, "Towards all-soft matter circuits: Prototypes of quasi-liquid devices with memristor characteristics," *Advanced Materials*, vol. 23, no. 31, pp. 3559–3564, 2011.

[42] S. H. Jeong, A. Hagman, K. Hjort, M. Jobs, J. Sundqvist, and Z. Wu, "Liquid alloy printing of microfluidic stretchable electronics," *Lab on a Chip*, vol. 12, no. 22, p. 4657, 2012.

[43] A. Fassler and C. Majidi, "3d structures of liquid-phase gain alloy embedded in pdms with freeze casting," *Lab on a Chip*, vol. 13, no. 22, pp. 4442–4450, 2013.

[44] M. D. Dickey, "Emerging applications of liquid metals featuring surface oxides," *ACS Applied Materials and Interfaces*, vol. 6, no. 21, pp. 18369–18379, 2014.

[45] C. Koo, B. E. LeBlanc, M. Kelley, H. E. Fitzgerald, G. H. Huff, and A. Han, "Manipulating Liquid Metal Droplets in Microfluidic Channels With Minimized Skin Residues Toward Tunable RF Applications," *Journal of Microelectromechanical Systems*, vol. 24, no. 4, pp. 1069–1076, 2014.

[46] I. D. Joshipura, H. R. Ayers, C. Majidi, and M. D. Dickey, "Methods to pattern liquid metals," *J. Mater. Chem. C*, vol. 3, no. 16, pp. 3834–3841, 2015.

[47] S. W. Jin, J. Park, S. Y. Hong, H. Park, Y. R. Jeong, J. Park, S.-S. Lee, and J. S. Ha, "Stretchable Loudspeaker using Liquid Metal Microchannel," *Scientific Reports*, vol. 5, p. 11695, jul 2015.

[48] M. Wang, C. Trlica, M. R. Khan, M. D. Dickey, and J. J. Adams, "A reconfigurable liquid metal antenna driven by electrochemically controlled capillarity," *Journal of Applied Physics*, vol. 117, no. 19, 2015.

[49] C. B. Eaker and M. D. Dickey, "Liquid metal actuation by electrical control of interfacial tension," *Applied Physics Reviews*, vol. 3, no. 3, 2016.

[50] M. Khondoker and D. Sameoto, "Fabrication methods and applications of microstructured gallium based liquid metal alloys," *Smart Materials and Structures*, vol. 25, no. 9, p. 093001, 2016.

[51] M. U. Memon, K. Ling, Y. Seo, and S. Lim, "Frequency-switchable half-mode substrate-integrated waveguide antenna injecting eutectic gallium indium (EGaIn) liquid metal alloy," *Journal of Electromagnetic Waves and Applications*, vol. 29, no. 16, pp. 2207–2215, 2015.

[52] R. C. Chiechi, E. A. Weiss, M. D. Dickey, and G. M. Whitesides, "Eutectic gallium–indium (egain): A moldable liquid metal for electrical characterization of self-assembled monolayers," *Angewandte Chemie*, vol. 120, no. 1, pp. 148–150, 2008.

[53] A. Fassler and C. Majidi, "Soft-matter capacitors and inductors for hyperelastic strain sensing and stretchable electronics," *Smart Materials and Structures*, vol. 22, no. 5, p. 055023, 2013.

[54] J. S. Noh, "Conductive elastomers for stretchable electronics, sensors and energy harvesters," *Polymers*, vol. 8, no. 4, 2016.

[55] J.-B. Chossat, Y. Tao, V. Duchaine, and Y.-L. Park, "Wearable Soft Artificial Skin for Hand Motion Detection with Embedded Microfluidic Strain Sensing," in *2015 IEEE International Conference on Robotics and Automation (ICRA)*, pp. 2568–2573, 2015.

[56] M. Gao and L. Gui, "A handy liquid metal based electroosmotic flow pump.," *Lab on a Chip*, vol. 14, no. 11, pp. 1866–72, 2014.

[57] Y. Menguc, Y.-L. Park, H. Pei, D. Vogt, P. M. Aubin, E. Winchell, L. Fluke, L. Stirling, R. J. Wood, and C. J. Walsh, "Wearable soft sensing suit for human gait measurement," *The International Journal of Robotics Research*, vol. 33, no. 14, pp. 1748–1764, 2014.

[58] F. L. Hammond, R. K. Kramer, Q. Wan, R. D. Howe, R. J. Wood, F. L. H. Iii, R. K. Kramer, Q. Wan, R. D. Howe, and R. J. Wood, "Soft tactile sensor arrays for micromanipulation," *IEEE International Conference on Intelligent Robots and Systems*, vol. 14, no. 5, pp. 1443–1452, 2014.

[59] D. M. Vogt and R. J. Wood, "Wrist Angle Measurements using Soft Sensors," *IEEE Sensors*, vol. 2, pp. 1–4, 2014.

[60] C. Keplinger, J.-Y. Y. Sun, C. C. Foo, P. Rothemund, G. M. Whitesides, and Z. Suo, "Stretchable, transparent, ionic conductors.," *Science*, vol. 341, no. 6149, pp. 984–7, 2013.

[61] J.-Y. Sun, X. Zhao, W. R. K. Illeperuma, O. Chaudhuri, K. H. Oh, D. J. Mooney, J. J. Vlassak, and Z. Suo, "Highly stretchable and tough hydrogels," *Nature*, vol. 489, no. 7414, pp. 133–136, 2012.

[62] Y. Shi, L. Pan, B. Liu, Y. Wang, Y. Cui, Z. Bao, and G. Yu, "Nanostructured conductive polypyrrole hydrogels as high-performance, flexible supercapacitor electrodes," *Journal of Materials Chemistry A*, vol. 2, no. 17, p. 6086, 2014.

[63] J. Park, I. You, S. Shin, and U. Jeong, "Material approaches to stretchable strain sensors," *ChemPhysChem*, vol. 16, no. 6, pp. 1155–1163, 2015.

[64] S. Liu, X. Sun, O. J. Hildreth, and K. Rykaczewski, "Design and characterization of a single channel two-liquid capacitor and its application to hyperelastic strain sensing," *Lab on a Chip*, vol. 15, pp. 1376–1384, 2015.

[65] Y. L. Han, H. Liu, C. Ouyang, T. J. Lu, and F. Xu, "Liquid on Paper: Rapid Prototyping of Soft Functional Components for Paper Electronics.," *Scientific reports*, vol. 5, p. 11488, 2015.

[66] D. P. Parekh, C. Ladd, L. Panich, K. Moussa, and M. D. Dickey, "3D printing of liquid metals as fugitive inks for fabrication of 3D microfluidic channels," *Lab on a Chip*, vol. 16, no. 10, pp. 1812–1820, 2016.

[67] S. Kim, J. Lee, and B. Choi, "Stretching and twisting sensing with liquid-metal strain gauges printed on silicone elastomers," *IEEE Sensors Journal*, vol. 15, no. 11, pp. 6077–6078, 2015.

[68] R. A. Awang, T. Baum, M. Nasabi, S. Sriram, and W. S. T. Rowe, "Mechanically tolerant fluidic split ring resonators," *Smart Materials and Structures*, vol. 25, no. 7, p. 075023, 2016.

[69] A. Pourghorban Saghati, J. Singh Batra, J. Kameoka, and K. Entesari, "A Microfluidically Reconfigurable Dual-Band Slot Antenna with a Frequency Coverage Ratio of 3:1," *IEEE Antennas and Wireless Propagation Letters*, vol. 15, pp. 122–125, 2016.

[70] A. Pourghorban Saghati, J. S. Batra, J. Kameoka, and K. Entesari, "A Miniaturized Microfluidically Reconfigurable Coplanar Waveguide Bandpass Filter With Maximum Power Handling of 10 Watts," *IEEE Transactions on Microwave Theory and Techniques*, vol. 63, no. 8, pp. 2515–2525, 2015.

[71] K. Ling, H. K. Kim, M. Yoo, and S. Lim, "Frequency-switchable metamaterial absorber injecting eutectic gallium-indium (EGaIn) liquid metal alloy," *Sensors*, vol. 15, no. 11, pp. 28154–28165, 2015.

[72] D. Kim, J. H. Yoo, and J.-B. Lee, "Liquid metal-based reconfigurable and stretchable photolithography," *Journal of Micromechanics and Microengineering*, vol. 26, no. 4, p. 045004, 2016.

[73] B. L. Cumby, G. J. Hayes, M. D. Dickey, R. S. Justice, C. E. Tabor, and J. C. Heikenfeld, "Reconfigurable liquid metal circuits by Laplace pressure shaping," *Applied Physics Letters*, vol. 101, no. 17, pp. 1–6, 2012.

[74] R. C. Gough, A. M. Morishita, J. H. Dang, W. Hu, W. A. Shiroma, and A. T. Ohta, "Continuous electrowetting of non-toxic liquid metal for rf applications," *IEEE Access*, vol. 2, pp. 874–882, 2014.

[75] Z. Wu, K. Hjort, and S. H. Jeong, "Microfluidic stretchable radio-frequency devices," *Proceedings of the IEEE*, vol. 103, no. 7, pp. 1211–1225, 2015.

[76] A. P. Saghati, J. S. Batra, J. Kameoka, and K. Entesari, "Miniature and reconfigurable cpw folded slot antennas employing liquid-metal capacitive loading," *IEEE Transactions on Antennas and Propagation*, vol. 63, no. 9, pp. 3798–3807, 2015.

[77] R. C. Ordonez, C. K. Hayashi, C. M. Torres, N. Hafner, J. R. Adleman, N. M. Acosta, J. Melcher, N. M. Kamin, and D. Garmire, "Conformal Liquid-Metal Electrodes for Flexible Graphene Device Interconnects," *IEEE Transactions on Electron Devices*, vol. 63, no. 10, pp. 4018–4023, 2016.

[78] F. Ongul, S. Yuksel, S. Bozar, G. Cakmak, H. Guney, D. Egbe, and S. Gunes, "Vacuum-free processed bulk heterojunction solar cells with E-GaIn cathode as an alternative to Al electrode," *Journal of Physics D: Applied Physics*, vol. 48, no. 17, p. 175102, 2015.

[79] J. Wissman, L. Finkenauer, L. Deseri, and C. Majidi, "Saddle-like deformation in a dielectric elastomer actuator embedded with liquid-phase gallium-indium electrodes," *Journal of Applied Physics*, vol. 116, no. 14, 2014.

[80] K. Ling, K. Kim, and S. Lim, "Flexible liquid metal-filled metamaterial absorber on polydimethylsiloxane (PDMS)," *Optics Express*, vol. 23, no. 16, p. 21375, 2015.

[81] J. Wang, S. Liu, S. Guruswamy, and A. Nahata, "Reconfigurable terahertz metamaterial device with pressure memory," *Optics Express*, vol. 22, no. 4, p. 4065, 2014.

[82] H. K. Kim, D. Lee, and S. Lim, "Wideband-Switchable Metamaterial Absorber Using Injected Liquid Metal," *Scientific Reports*, vol. 6, no. August, p. 31823, 2016.

[83] M. R. Khan, C. B. Eaker, E. F. Bowden, and M. D. Dickey, "Giant and switchable surface activity of liquid metal via surface oxidation," *Proceedings of the National Academy of Sciences*, vol. 111, no. 39, pp. 14047–14051, 2014.

[84] J. Tang, J. Wang, J. Liu, and Y. Zhou, "Jumping liquid metal droplet in electrolyte triggered by solid metal particles," *Applied Physics Letters*, vol. 108, no. 22, 2016.

[85] J. Y. Zhu, S. Y. Tang, K. Khoshmanesh, and K. Ghorbani, "An Integrated Liquid Cooling System Based on Galinstan Liquid Metal Droplets," *ACS Applied Materials and Interfaces*, vol. 8, no. 3, pp. 2173–2180, 2016.

[86] A. Zavabeti, T. Daeneke, A. F. Chrimes, A. P. O'Mullane, J. Zhen Ou, A. Mitchell, K. Khoshmanesh, and K. Kalantar-zadeh, "Ionic imbalance induced self-propulsion of liquid metals," *Nature Communications*, vol. 7, no. May, p. 12402, 2016.

[87] M. Mohammed, R. Sundaresan, and M. D. Dickey, "Self-Running Liquid Metal Drops that Delaminate Metal Films at Record Velocities," *ACS Applied Materials and Interfaces*, vol. 7, no. 41, pp. 23163–23171, 2015.

[88] S. Y. Tang, J. Zhu, V. Sivan, B. Gol, R. Soffe, W. Zhang, A. Mitchell, and K. Khoshmanesh, "Creation of Liquid Metal 3D Microstructures Using Dielectrophoresis," *Advanced Functional Materials*, vol. 25, no. 28, pp. 4445–4452, 2015.

[89] L. Wang and J. Liu, "Electromagnetic rotation of a liquid metal sphere or pool within a solution," *Proceedings of the Royal Society A*, vol. 471, p. 20150177, 2015.

[90] J. Wang, K. Appusamy, S. Guruswamy, and A. Nahata, "Electrolytic reduction of liquid metal oxides and its application to reconfigurable structured devices.," *Scientific reports*, vol. 5, no. ii, p. 8637, 2015.

[91] M. R. Khan, C. Trlica, and M. D. Dickey, "Recapillarity: Electrochemically controlled capillary withdrawal of a liquid metal alloy from microchannels," *Advanced Functional Materials*, vol. 25, no. 5, pp. 671–678, 2015.

[92] S.-Y. Tang, Y. Lin, I. D. Joshipura, K. Khoshmanesh, and M. D. Dickey, "Steering liquid metal flow in microchannels using low voltages," *Lab on a Chip*, vol. 15, no. 19, pp. 3905–3911, 2015.

[93] E. Mitraka, L. Kergoat, Z. U. Khan, S. Fabiano, O. Douhéret, P. Leclère, M. Nilsson, P. Andersson Ersman, G. Gustafsson, R. Lazzaroni, M. Berggren, and X. Crispin, "Solution processed liquid metal-conducting polymer hybrid thin films as electrochemical pH-threshold indicators," *J. Mater. Chem. C*, vol. 3, no. 29, pp. 7604–7611, 2015.

[94] J. Zhang, Y. Yao, L. Sheng, and J. Liu, "Self-fueled biomimetic liquid metal mollusk," *Advanced Materials*, vol. 27, no. 16, pp. 2648–2655, 2015.

[95] W. Q. Fang, Z. Z. He, and J. Liu, "Electro-hydrodynamic shooting phenomenon of liquid metal stream," *Applied Physics Letters*, vol. 105, no. 13, pp. 18–22, 2014.

[96] K. S. Wimbush, R. M. Fratila, D. Wang, D. Qi, C. Liang, L. Yuan, N. Yakovlev, K. P. Loh, D. N. Reinhoudt, A. H. Velders, and C. A. Nijhuis, "Bias induced transition from an ohmic to a non-ohmic interface in supramolecular tunneling junctions with Ga2O3/EGaIn top electrodes.," *Nanoscale*, vol. 6, no. 19, pp. 11246–58, 2014.

[97] A. F. Chrimes, K. J. Berean, A. Mitchell, G. Rosengarten, and K. Kalantar-Zadeh, "Controlled Electrochemical Deformation of Liquid-Phase Gallium," *ACS Applied Materials and Interfaces*, vol. 8, no. 6, pp. 3833–3839, 2016.

[98] M. Dickey, C. Eaker, and M. R. Kahn, "A Method to Manipulate Surface Tension of a Liquid Metal via Surface Oxidation and Reduction," *Journal of Visualized Experiments*, no. January, pp. 1–7, 2016.

[99] G. Li, M. Parmar, D. Kim, J.-B. J. B. Lee, and D.-W. Lee, "PDMS based coplanar microfluidic channels for the surface reduction of oxidized Galinstan.," *Lab on a Chip*, vol. 14, no. 1, pp. 200–9, 2014.

[100] D. Kim, Y. Lee, D. W. Lee, W. Choi, K. Yoo, and J. B. Lee, "Hydrochloric acid-impregnated paper for gallium-based liquid metal microfluidics," *Sensors and Actuators, B: Chemical*, vol. 207, no. Part A, pp. 199–205, 2015.

[101] B. Kim, J. Jang, I. You, J. Park, S. Shin, G. Jeon, J. K. Kim, and U. Jeong, "Interfacing liquid metals with stretchable metal conductors," *ACS Applied Materials and Interfaces*, vol. 7, no. 15, pp. 7920–7926, 2015.

[102] G. Li, M. Parmar, and D.-W. Lee, "An oxidized liquid metal-based microfluidic platform for tunable electronic device applications," *Lab on a Chip*, vol. 15, pp. 766–775, 2015.

[103] M. R. Khan, C. Trlica, J.-H. So, M. Valeri, and M. D. Dickey, "Influence of water on the interfacial behavior of gallium liquid metal alloys.," *ACS applied materials & interfaces*, vol. 6, no. 24, pp. 22467–73, 2014.

[104] Y. L. Park, B. R. Chen, and R. J. Wood, "Design and fabrication of soft artificial skin using embedded microchannels and liquid conductors," *IEEE Sensors Journal*, vol. 12, no. 8, pp. 2711–2718, 2012.

[105] A. C. Siegel, S. S. Shevkoplyas, D. B. Weibel, D. A. Bruzewicz, A. W. Martinez, and G. M. Whitesides, "Cofabrication of electromagnets and microfluidic systems in poly(dimethylsiloxane)," *Angewandte Chemie - International Edition*, vol. 45, no. 41, pp. 6877–6882, 2006.

[106] M. D. Dickey, R. C. Chiechi, R. J. Larsen, E. A. Weiss, D. A. Weitz, and G. M. Whitesides, "Eutectic Gallium-Indium (EGaIn): A Liquid Metal Alloy for the Formation of Stable Structures in Microchannels at Room Temperature," *Advanced Functional Materials*, vol. 18, no. 7, pp. 1097–1104, 2008.

[107] S. Cheng and Z. Wu, "Microfluidic electronics.," *Lab on a Chip*, vol. 12, no. 16, pp. 2782–91, 2012.

[108] S. Yu and M. Kaviany, "Electrical, thermal, and species transport properties of liquid eutectic

Ga-In and Ga-In-Sn from first principles.," *The Journal of Chemical Physics*, vol. 140, no. 6, p. 064303, 2014.

[109] Y. Plevachuk, V. Sklyarchuk, S. Eckert, G. Gerbeth, and R. Novakovic, "Thermophysical Properties of the Liquid Ga–In–Sn Eutectic Alloy," *J. Chem. Eng. Data*, vol. 59, pp. 757–763, 2014.

[110] Y. Plevachuk, V. Sklyarchuk, N. Shevchenko, and S. Eckert, "Electrophysical and structure-sensitive properties of liquid Ga – In alloys," *International Journal of Materials Research*, vol. 106, 2015.

[111] J. N. Koster, "Directional solidification and melting of eutectic GaIn," *Crystal Research and Technology*, vol. 34, no. 9, pp. 1129–1140, 1999.

[112] Y. Lu, Q. Hu, Y. Lin, D. B. Pacardo, C. Wang, W. Sun, F. S. Ligler, M. D. Dickey, and Z. Gu, "Transformable liquid-metal nanomedicine," *Nature Communications*, vol. 6, no. May, p. 10066, 2015.

[113] T. Liu, P. Sen, and C. J. Kim, "Characterization of nontoxic liquid-metal alloy galinstan for applications in microdevices," *Journal of Microelectromechanical Systems*, vol. 21, no. 2, pp. 443–450, 2012.

[114] M. J. Regan, H. Tostmann, P. S. Pershan, O. M. Magnussen, E. Dimasi, B. M. Ocko, and M. Deutsch, "X-ray study of the oxidation of liquid-gallium surfaces," *Physical Review B*, vol. 55, no. 16, pp. 786–790, 1997.

[115] L. Cademartiri, M. M. Thuo, C. A. Nijhuis, W. F. Reus, S. Tricard, J. R. Barber, R. N. S. Sodhi, P. Brodersen, C. Kim, R. C. Chiechi, and G. M. Whitesides, "Electrical resistance of agts–s(ch2)n1ch3//ga2o3/egain tunneling junctions," *The Journal of Physical Chemistry C*, vol. 116, no. 20, pp. 10848–10860, 2012.

[116] R. J. Larsen, M. D. Dickey, G. M. Whitesides, and D. A. Weitz, "Viscoelastic properties of oxide-coated liquid metals," *Journal of Rheology*, vol. 53, no. 6, pp. 1305–1326, 2009.

[117] S. Liu, X. Sun, N. Kemme, V. G. Damle, C. Schott, M. Herrmann, and K. Rykaczewski, "Can liquid metal flow in microchannels made of its own oxide skin?," *Microfluidics and Nanofluidics*, vol. 20, no. 1, pp. 1–6, 2016.

[118] J. W. Boley, E. L. White, G. T. C. Chiu, and R. K. Kramer, "Direct writing of gallium-indium alloy for stretchable electronics," *Advanced Functional Materials*, vol. 24, no. 23, pp. 3501–3507, 2014.

[119] B. A. Gozen, A. Tabatabai, O. B. Ozdoganlar, and C. Majidi, "High-density soft-matter electronics with micron-scale line width," *Advanced Materials*, vol. 26, no. 30, pp. 5211–5216, 2014.

[120] T. Hutter, W. A. C. Bauer, S. R. Elliott, and W. T. S. Huck, "Formation of spherical and non-spherical eutectic Gallium-Indium liquid-metal microdroplets in microfluidic channels at room temperature," *Advanced Functional Materials*, vol. 22, no. 12, pp. 2624–2631, 2012.

[121] J. N. Hohman, M. Kim, G. A. Wadsworth, H. R. Bednar, J. Jiang, M. A. LeThai, and P. S. Weiss, "Directing substrate morphology via self-assembly: Ligand-mediated scission of gallium–indium microspheres to the nanoscale," *Nano letters*, vol. 11, no. 12, pp. 5104–5110, 2011.

[122] D.-H. Kim, N. Lu, R. Ma, Y.-S. Kim, R.-H. Kim, S. Wang, J. Wu, S. M. Won, H. Tao, A. Islam, K. J. Yu, T.-i. Kim, R. Chowdhury, M. Ying, L. Xu, M. Li, H.-J. Chung, H. Keum, M. McCormick, P. Liu, Y.-W. Zhang, F. G. Omenetto, Y. Huang, T. Coleman, and J. a. Rogers, "Epidermal electronics.," *Science (New York, N.Y.)*, vol. 333, no. 6044, pp. 838–843, 2011.

[123] M. Kaltenbrunner, T. Sekitani, J. Reeder, T. Yokota, K. Kuribara, T. Tokuhara, M. Drack, R. Schwödiauer, I. Graz, S. Bauer-Gogonea, S. Bauer, and T. Someya, "An ultra-lightweight design for imperceptible plastic electronics.," *Nature*, vol. 499, no. 7459, pp. 458–63, 2013.

[124] C. Majidi, "Soft Robotics: A Perspective—Current Trends and Prospects for the Future," *Soft Robotics*, vol. 1, pp. 5–11, mar 2014.

[125] R. F. Shepherd, F. Ilievski, W. Choi, S. a. Morin, A. a. Stokes, A. D. Mazzeo, X. Chen, M. Wang, and G. M. Whitesides, "Multigait soft robot.," *Proceedings of the National Academy of Sciences of the United States of America*, vol. 108, pp. 20400–3, dec 2011.

[126] S. J. A. Koh, X. Zhao, and Z. Suo, "Maximal energy that can be converted by a dielectric elastomer generator," *Applied Physics Letters*, vol. 94, no. 26, pp. 1–3, 2009.

[127] X. Niu, S. Peng, L. Liu, W. Wen, and P. Sheng, "Characterizing and patterning of PDMS-based conducting composites," *Advanced Materials*, vol. 19, no. 18, pp. 2682–2686, 2007.

[128] Z.-M. Dang, J.-K. Yuan, J.-W. Zha, T. Zhou, S.-T. Li, and G.-H. Hu, "Fundamentals, processes and applications of high-permittivity polymer–matrix composites," *Progress in Materials Science*, vol. 57, pp. 660–723, may 2012.

[129] A. Shakun, *Soft Elastomeric Material With Improved Dielectric Permittivity.* Master of science thesis, Tampere University of Technology, 2014.

[130] G. Gallone, F. Carpi, D. De Rossi, G. Levita, and A. Marchetti, "Dielectric constant enhancement in a silicone elastomer filled with lead magnesium niobate-lead titanate," *Materials Science and Engineering C*, vol. 27, no. 1, pp. 110–116, 2007.

[131] F. Carpi and D. De Rossi, "Improvement of electromechanical actuating performances of a silicone dielectric elastomer by dispersion of titanium dioxide powder," *IEEE Transactions on Dielectrics and Electrical Insulation*, vol. 12, no. 4, pp. 835–843, 2005.

[132] L. Bokobza and C. Belin, "Effect of strain on the properties of a styrene–butadiene rubber filled with multiwall carbon nanotubes," *Journal of Applied Polymer Science*, vol. 105, no. 4, pp. 2054–2061, 2007.

[133] A. R. Von Hippel, *Dielectric materials and applications: Papers by twenty-two contributors.* The Technology Press of MIT; John Wiley & Sons; Chapman & Hall, 1954.

[134] S. Ahmed and F. R. Jones, "A review of particulate reinforcement theories for polymer composites," *Journal of Materials Science*, vol. 25, no. 12, pp. 4933–4942, 1990.

[135] J. Cho, M. S. Joshi, and C. T. Sun, "Effect of inclusion size on mechanical properties of polymeric composites with micro and nano particles," *Composites Science and Technology*, vol. 66, no. 13, pp. 1941–1952, 2006.

[136] S. Y. Fu, X. Q. Feng, B. Lauke, and Y. W. Mai, "Effects of particle size, particle/matrix interface adhesion and particle loading on mechanical properties of particulate-polymer composites," *Composites Part B: Engineering*, vol. 39, no. 6, pp. 933–961, 2008.

[137] A. Fassler and C. Majidi, "Liquid-Phase Metal Inclusions for a Conductive Polymer Composite," *Advanced Materials*, vol. 27, no. 11, pp. 1928–1932, 2015.

[138] R. W. Style, R. Boltyanskiy, B. Allen, K. E. Jensen, H. P. Foote, J. S. Wettlaufer, and E. R. Dufresne, "Stiffening solids with liquid inclusions," *Nat Phys*, vol. 11, pp. 82–87, jan 2015.

[139] M. F. Ashby, L. J. Gibson, U. Wegst, and R. Olive, "The Mechanical Properties of Natural Materials. I. Material Property Charts," *Proceedings of the Royal Society of London. Series A: Mathematical and Physical Sciences*, vol. 450, no. 1938, pp. 123–140, 1995.

[140] R. C. Chiechi, E. a. Weiss, M. D. Dickey, and G. M. Whitesides, "Eutectic gallium-indium (EGaIn): A moldable liquid metal for electrical characterization of self-assembled monolayers," *Angewandte Chemie - International Edition*, vol. 47, no. 1, pp. 142–144, 2008.

[141] M. D. Dickey, R. C. Chiechi, R. J. Larsen, E. a. Weiss, D. a. Weitz, and G. M. Whitesides, "Eutectic gallium-indium (EGaIn): A liquid metal alloy for the formation of stable structures in microchannels at room temperature," *Advanced Functional Materials*, vol. 18, no. 7, pp. 1097–1104, 2008.

[142] I. D. Joshipura, H. R. Ayers, C. Majidi, and M. D. Dickey, "Methods to pattern liquid metals," *J. Mater. Chem. C*, vol. 3, no. 16, pp. 3834–3841, 2015.

[143] D. A. G. Bruggeman, "Berechnung verschiedener physikalischer Konstanten von heterogenen Substanzen. I. Dielektrizitätskonstanten und Leitfähigkeiten der Mischkörper aus isotropen Substanzen," *Annalen der Physik*, vol. 416, no. 7, pp. 636–664, 1935.

[144] J. C. M. Garnett, "Colours in Metal Glasses and in Metallic Films," *Philosophical Transactions of the Royal Society of London A: Mathematical, Physical and Engineering Sciences*, vol. 203, no. 359-371, pp. 385–420, 1904.

[145] T. C. Choy, *Effective Medium Theory: Principles and Applications*. International series of monographs on physics, Clarendon Press, Oxford, 1999.

[146] C.-W. Nan, R. Birringer, D. R. Clarke, and H. Gleiter, "Effective thermal conductivity of particulate composites with interfacial thermal resistance," *Journal of Applied Physics*, vol. 81, no. 10, pp. 6692–6699, 1997.

[147] Q. Xu, N. Oudalov, Q. Guo, H. M. Jaeger, and E. Brown, "Effect of oxidation on the mechanical properties of liquid gallium and eutectic gallium-indium," *Physics of Fluids*, vol. 24, no. 6, p. 063101, 2012.

[148] L. Mullins, "Softening of Rubber by Deformation," *Rubber Chemistry and Technology*, vol. 42, no. 1, pp. 339–362, 1969.

[149] J. Diani, B. Fayolle, and P. Gilormini, "A review on the Mullins effect," vol. 45, no. 3, pp. 601–612, 2009.

[150] Virendra and Singh, "High thermal conductivity of chain-oriented amorphous polythiophene," *Nature nanotechnology*, vol. 9, no. 5, pp. 384–390, 2014.

[151] X. S. Wang, H. P. Tang, X. D. Li, and X. Hua, "Investigations on the mechanical properties of conducting polymer coating-substrate structures and their influencing factors," *International Journal of Molecular Sciences*, vol. 10, no. 12, pp. 5257–5284, 2009.

[152] P. Miranzo, E. García, C. Ramírez, J. González-Julián, M. Belmonte, and M. Isabel Osendi, "Anisotropic thermal conductivity of silicon nitride ceramics containing carbon nanostructures," *Journal of the European Ceramic Society*, vol. 32, no. 8, pp. 1847–1854, 2012.

[153] C. P. Wong and R. S. Bollampally, "Thermal conductivity, elastic modulus, and coefficient of thermal expansion of polymer composites filled with ceramic particles for electronic packaging," *Journal of Applied Polymer Science*, vol. 74, no. 14, pp. 3396–3403, 1999.

[154] Y. P. Mamunya, V. V. Davydenko, P. Pissis, and E. V. Lebedev, "Electrical and thermal conductivity of polymers filled with metal powders," *European Polymer Journal*, vol. 38, no. 9, pp. 1887–1897, 2002.

[155] R. C. Zeller and R. O. Pohl, "Thermal conductivity and specific heat of noncrystalline solids," *Physical Review B*, vol. 4, no. 6, pp. 2029–2041, 1971.

[156] J. Plawsky, *Transport Phenomena Fundamentals*. CRC Press, 2014.

[157] S. Shen, A. Henry, J. Tong, R. Zheng, and G. Chen, "Polyethylene nanofibres with very high thermal conductivities.," *Nature nanotechnology*, vol. 5, pp. 251–5, apr 2010.

[158] D. M. Bigg, "Thermally conductive polymer compositions," *Polymer Composites*, vol. 7, no. 3, pp. 125–140, 1986.

[159] H. Cong and T. Pan, "Photopatternable Conductive PDMS Materials for Microfabrication," *Advanced Functional Materials*, vol. 18, pp. 1912–1921, jul 2008.

[160] S. H. Jeong, S. Chen, J. Huo, E. K. Gamstedt, J. Liu, S.-L. Zhang, Z.-B. Zhang, K. Hjort, and Z. Wu, "Mechanically Stretchable and Electrically Insulating Thermal Elastomer Composite by Liquid Alloy Droplet Embedment," *Scientific Reports*, vol. 5, p. 18257, 2015.

[161] R. F. Hill and P. H. Supancic, "Thermal Conductivity of Platelet-Filled Polymer Composites," *Journal of American Ceramic Society*, vol. 85, no. 4, pp. 851–857, 2002.

[162] Y.-M. Chen and J.-M. Ting, "Ultra high thermal conductivity polymer composites," *Carbon*, vol. 40, no. 3, pp. 359–362, 2002.

[163] M. J. Biercuk, M. C. Llaguno, M. Radosavljevic, J. K. Hyun, A. T. Johnson, and J. E. Fischer, "Carbon nanotube composites for thermal management," *Applied Physics Letters*, vol. 80, no. 15, pp. 2767–2769, 2002.

[164] K. M. F. Shahil and A. A. Balandin, "Graphene-multilayer graphene nanocomposites as highly efficient thermal interface materials," *Nano Letters*, vol. 12, no. 2, pp. 861–867, 2012.

[165] K. Kurabayashi, "Anisotropic Thermal Properties of Solid Polymers," *International Journal of Thermophysics*, vol. 22, no. 1, pp. 277–288, 2001.

[166] S. Stankovich, D. A. Dikin, G. H. B. Dommett, K. M. Kohlhaas, E. J. Zimney, E. A. Stach, R. D. Piner, S. T. Nguyen, and R. S. Ruoff, "Graphene-based composite materials," *Nature*, vol. 442, no. 7100, pp. 282–286, 2006.

[167] Y. Nagasaka and A. Nagashima, "Absolute Measurement of the Thermal Conductivity of Electrically Conducting Liquids By the Transient Hot-Wire Method.," *Journal of Physics E: Scientific Instruments*, vol. 14, no. 12, pp. 1435–1440, 1981.

[168] T. Ohmura, M. Tsuboi, and T. Tomimura, "Estimation of the Mean Thermal Conductivity of Anisotropic Materials," *International Journal*, vol. 23, no. 3, pp. 843–853, 2002.

[169] T. Borca-Tasciuc, A. R. Kumar, and G. Chen, "Data reduction in 3ω method for thin-film thermal conductivity determination," *Review of Scientific Instruments*, vol. 72, no. 4, pp. 2139–2147, 2001.

[170] Z. Han and A. Fina, "Thermal conductivity of carbon nanotubes and their polymer nanocomposites: A review," *Progress in Polymer Science (Oxford)*, vol. 36, no. 7, pp. 914–944, 2011.

[171] P. A. Sen, C. Scala, and M. H. Cohen, "A self-similar model for sedimentary rocks with application to the dielectric constant of fused glass bead," *Geophysics*, vol. 46, no. 5, pp. 781–795, 1981.

[172] C. S. Haines, M. D. Lima, N. Li, G. M. Spinks, J. Foroughi, J. D. Madden, S. H. Kim, S. Fang, M. Jung de Andrade, F. Goktepe, O. Goktepe, S. M. Mirvakili, S. Naficy, X. Lepro, J. Oh, M. E. Kozlov, S. J. Kim, X. Xu, B. J. Swedlove, G. G. Wallace, and R. H. Baughman, "Artificial muscles from fishing line and sewing thread," *Science*, vol. 343, no. 6173, pp. 868–872, 2014.

[173] S. A. Morin, R. F. Shepherd, S. W. Kwok, A. A. Stokes, A. Nemiroski, and G. M. Whitesides, "Camouflage and Display for Soft Machines," *Science*, vol. 337, pp. 828–832, aug 2012.

[174] C. Larson, B. Peele, S. Li, S. Robinson, M. Totaro, L. Beccai, B. Mazzolai, and R. Shepherd, "Highly stretchable electroluminescent skin for optical signaling and tactile sensing," *Science*, vol. 351, pp. 1071–1074, mar 2016.

[175] R. W. Style, R. Boltyanskiy, B. Allen, K. E. Jensen, H. P. Foote, J. S. Wettlaufer, and E. R. Dufresne, "Stiffening solids with liquid inclusions," *Nature Physics*, vol. 11, pp. 82–87, Jan 2015.

[176] E. Caló and V. V. Khutoryanskiy, "Biomedical applications of hydrogels: A review of patents and commercial products," *European Polymer Journal*, vol. 65, pp. 252–267, 2015.

[177] C. Keplinger, J.-Y. Sun, C. C. Foo, P. Rothemund, G. M. Whitesides, and Z. Suo, "Stretchable, Transparent, Ionic Conductors," *Science*, vol. 341, no. 6149, pp. 984–987, 2013.

[178] E. Guth, "Theory of filler reinforcement," *Journal of Applied Physics*, vol. 16, no. 1, pp. 20–25, 1945.

[179] A. Agrawal, N. Rahbar, and P. D. Calvert, "Strong fiber-reinforced hydrogel," *Acta Biomaterialia*, vol. 9, no. 2, pp. 5313–5318, 2013.

[180] S. Lin, C. Cao, Q. Wang, M. Gonzalez, J. E. Dolbow, and X. Zhao, "Design of stiff, tough and stretchy hydrogel composites via nanoscale hybrid crosslinking and macroscale fiber reinforcement," *Soft Matter*, vol. 10, no. 38, pp. 7519–7527, 2014.

[181] J. P. Gong, Y. Katsuyama, T. Kurokawa, and Y. Osada, "Double-network hydrogels with extremely high mechanical strength," *Advanced Materials*, vol. 15, no. 14, pp. 1155–1158, 2003.

[182] H. Peterlik, P. Roschger, K. Klaushofer, and P. Fratzl, "From brittle to ductile fracture of bone," *Nature Materials*, vol. 5, no. January, pp. 52–55, 2005.

[183] K. J. Koester, J. W. Ager, R. O. Ritchie, J. W. Ager III, and R. O. Ritchie, "The true toughness of human cortical bone measured with realistically short cracks," *Nature materials*, vol. 7, no. 8, pp. 672–677, 2008.

[184] W. Yang, V. R. Sherman, B. Gludovatz, E. Schaible, P. Stewart, R. O. Ritchie, and M. A. Meyers, "On the tear resistance of skin.," *Nature communications*, vol. 6, p. 6649, 2015.

[185] E. Ducrot, Y. Chen, M. Bulters, R. P. Sijbesma, and C. Creton, "Toughening elastomers with sacrificial bonds and watching them break," *Science*, vol. 344, no. 6180, pp. 186–189, 2014.

[186] C. Creton and M. Ciccotti, "Fracture and adhesion of soft materials: a review," *Reports on Progress in Physics*, vol. 79, no. 4, p. 046601, 2016.

[187] K. Tsunoda, J. J. C. Busfield, C. K. L. Davies, and A. G. Thomas, "Effect of materials variables on the tear behaviour of a non-crystallizing elastomer," *Journal of Materials Science*, vol. 35, no. 20, pp. 5187–5198, 2000.

[188] J. J. C. Busfield, C. Deeprasertkul, and A. G.Thomas, "The effect of liquids on the dynamic properties of carbon black filled naturalrubber as a function of pre-strain," *Polymer*, vol. 41, pp. 9219–9225, 2000.

[189] A. C. Balazs, T. Emrick, and T. P. Russell, "Nanoparticle Polymer Composites: Where Two Small Worlds Meet," *Science*, vol. 314, no. 5802, pp. 1107–1110, 2006.

[190] C. Nah, J. Y. . Lim, B. H. . Cho, C. K. . Hong, and A. N. Gent, "Reinforcing rubber with carbon nanotubes," *Journal of Applied Polymer Science*, vol. 118, no. 3, pp. 1574–1581, 2010.

[191] S. C. Wong, A. Baji, and A. N. Gent, "Effect of specimen thickness on fracture toughness and adhesive properties of hydroxyapatite-filled polycaprolactone," *Composites Part A: Applied Science and Manufacturing*, vol. 39, no. 4, pp. 579–587, 2008.

[192] D. Kohls and G. Beaucage, "Rational design of reinforced rubber," *Current Opinion in Solid State and Materials Science*, vol. 6, no. 3, pp. 183–194, 2002.

[193] D. R. King, T. L. Sun, Y. Huang, T. Kurokawa, T. Nonoyama, A. J. Crosby, and J. P. Gong, "Extremely tough composites from fabric reinforced polyampholyte hydrogels," *Mater. Horiz.*, vol. 2, no. 6, pp. 584–591, 2015.

[194] Q. Chen, H. Chen, L. Zhu, and J. Zheng, "Engineering of Tough Double Network Hydrogels," *Macromolecular Chemistry and Physics*, vol. 217, no. 9, pp. 1022–1036, 2016.

[195] M. D. Bartlett, A. Fassler, N. Kazem, E. J. Markvicka, P. Mandal, and C. Majidi, "Stretchable, High-k Dielectric Elastomers through Liquid-Metal Inclusions," *Advanced Materials*, vol. 28, no. 19, pp. 3726–3731, 2016.

[196] P. S. Owuor, S. Hiremath, A. C. Chipara, R. Vajtai, J. Lou, D. R. Mahapatra, C. S. Tiwary, and P. M. Ajayan, "Nature Inspired Strategy to Enhance Mechanical Properties via Liquid Reinforcement," *Advanced Materials Interfaces*, vol. 1700240, pp. 1–9, 2017.

[197] B. S. Chang, R. Tutika, J. Cutinho, S. Oyola-Reynoso, J. Chen, M. D. Bartlett, and M. M. Thuo, "Mechanically triggered composite stiffness tuning through thermodynamic relaxation (st3r)," *Mater. Horiz.*, 2018.

[198] M. D. Dickey, R. C. Chiechi, R. J. Larsen, E. a. Weiss, D. a. Weitz, and G. M. Whitesides, "Eutectic gallium-indium (EGaIn): A liquid metal alloy for the formation of stable structures in microchannels at room temperature," *Advanced Functional Materials*, vol. 18, no. 7, pp. 1097–1104, 2008.

[199] N. Kazem, M. D. Bartlett, M. J. Powell-Palm, X. Huang, W. Sun, J. A. Malen, and C. Majidi, "High thermal conductivity in soft elastomers with elongated liquid metal inclusions," *APS March Meeting*, 2017.

[200] M. D. Bartlett, N. Kazem, M. J. Powell-Palm, X. Huang, W. Sun, J. A. Malen, and C. Majidi, "High thermal conductivity in soft elastomers with elongated liquid metal inclusions," *Proceedings of the National Academy of Sciences*, vol. 114, pp. 2143–2148, feb 2017.

[201] G. R. Hamed and A. A. Al-Sheneper, "Effect of Carbon Black Concentration on Cut Growth in NR Vulcanizates," *Rubber Chemistry and Technology*, vol. 76, no. 2, pp. 436–460, 2003.

[202] A. Goldberg, D. R. Lesuer, and J. Patt, "Observations Made During Stretching, Tearing, and Failure of NR and SBR Loaded with Various Amounts of Carbon Black," *Rubber Chemistry and Technology*, vol. 62, no. 2, pp. 288–304, 1989.

[203] H. Guo, C. Mussault, A. Brûlet, A. Marcellan, D. Hourdet, and N. Sanson, "Thermoresponsive Toughening in LCST-Type Hydrogels with Opposite Topology: From Structure to Fracture Properties," *Macromolecules*, vol. 49, no. 11, pp. 4295–4306, 2016.

[204] D. De and A. N. Gent, "Tear Strength of Carbon-Black-Filled Compounds," *Rubber Chemistry and Technology*, vol. 69, no. 5, pp. 834–850, 1996.

[205] K. A. Boroujeni and K. Han, "Perspective-based image-to-bim alignment for automated visual data collection and construction performance monitoring," *Computing in Civil Engineering*, pp. 171–178, 2017.

[206] G. J. Lake and A. G. Thomas, "The Strength of Highly Elastic Materials," *Proceedings of the Royal Society of London A: Mathematical, Physical and Engineering Sciences*, vol. 300, no. 1460, pp. 108–119, 1967.

[207] A. N. Gent, *Fracture : an advanced treatise*. New York : Academic Press, 1972.

[208] X. Zhao, "Designing toughness and strength for soft materials," *Proceedings of the National Academy of Sciences*, p. 201710942, 2017.

[209] F. Bueche, "Tensile strength of filled GR-S vulcanizates," *Journal of Polymer Science*, vol. 33, no. 126, pp. 259–271, 1958.

[210] E. H. Andrews and A. Walsh, "Rupture Propagation in Inhomogeneous Solids - an Electron Microscopic Study of Rubber Containing Colloidal Carbon Black," *Proceedings of the Physical Society*, vol. 72, no. 463, p. 42, 1958.

[211] R. S. Rivlin and a. G. Thomas, "Rupture of rubber. I. Characteristic energy for tearing," *Journal of Polymer Science*, vol. 10, no. 3, pp. 291–318, 1953.

[212] W. C. Navidi, *Statistics for engineers and scientists*, vol. 2. McGraw-Hill New York, 2006.

[213] R. J. Young and P. A. Lovell, *Introduction to polymers*. CRC press, 3rd edition ed., 2011.

[214] S. Mzabi, D. Berghezan, S. Roux, F. Hild, and C. Creton, "A critical local energy release rate criterion for fatigue fracture of elastomers," *Journal of Polymer Science, Part B: Polymer Physics*, vol. 49, no. 21, pp. 1518–1524, 2011.

[215] T. Zhang, S. Lin, H. Yuk, and X. Zhao, "Predicting fracture energies and crack-tip fields of soft tough materials," *Extreme Mechanics Letters*, vol. 4, pp. 1–8, 2015.

[216] J. Cook and J. Gordon, "A mechanism for the control of crack propagation in all-brittle systems," *Proceedings of the Royal Society of London A: Mathematical, Physical and Engineering Sciences*, vol. 282, no. 1391, pp. 508–520, 1964.

[217] J. Li, W. R. K. Illeperuma, Z. Suo, and J. J. Vlassak, "Hybrid Hydrogels with Extremely High Stiffness and Toughness," *ACS Macro Letters*, vol. 3, no. 6, pp. 520–523, 2014.

[218] D. Turnbull, "Formation of crystal nucleai in liquid metals," *j. Appl. Phy*, vol. 21, no. 10, pp. 1022–1028, 1950.

[219] D. Turnbull, "The supercooling of aggregates of small metal particles," *Journal of Metals*, vol. 2, no. 9, pp. 1144–1148, 1950.

[220] I. D. Tevis, L. B. Newcomb, and M. Thuo, "Synthesis of liquid core-shell particles and solid patchy multicomponent particles by shearing liquids into complex particles (SLICE)," *Langmuir*, vol. 30, no. 47, pp. 14308–14313, 2014.

[221] S. Çnar, I. D. Tevis, J. Chen, and M. Thuo, "Mechanical Fracturing of Core-Shell Undercooled Metal Particles for Heat-Free Soldering.," *Scientific reports*, vol. 6, no. September 2015, p. 21864, 2016.

[222] S. J. FRENCH, D. J. SAUNDERS, and G. W. INGLE, "the System Gallium-Indium," *The Journal of Physical Chemistry*, vol. 42, no. 2, pp. 265–274, 1937.

[223] G. B. Parravicini, A. Stella, P. Ghigna, G. Spinolo, A. Migliori, F. D'Acapito, and R. Kofman, "Extreme undercooling (down to 90 K) of liquid metal nanoparticles," *Applied Physics Letters*, vol. 89, no. 3, pp. 1–4, 2006.

[224] N. Bosq, N. Guigo, J. Persello, and N. Sbirrazzuoli, "Melt and glass crystallization of PDMS and PDMS silica nanocomposites," *Phys. Chem. Chem. Phys.*, vol. 16, no. 17, pp. 7830–7840, 2014.

[225] T. Dollase, H. W. Spiess, M. Gottlieb, and R. Yerushalmi-Rozen, "Crystallization of PDMS : The effect of physical and chemical crosslinks," *Europhysics Letters*, vol. 60, no. 3, pp. 390–396, 2002.

[226] K. Matyjaszewski and J. Xia, "Atom transfer radical polymerization," *Chemical Reviews*, vol. 101, no. 9, pp. 2921–2990, 2001.

[227] C. K. Schoff, *Rheology*. Federation of Societies for Coating Technology, 1991.

[228] D. M. Hoyle, D. Auhl, O. G. Harlen, V. C. Barroso, M. Wilhelm, and T. C. B. McLeish, "Large amplitude oscillatory shear and Fourier transform rheology analysis of branched polymer melts," *Journal of Rheology*, vol. 58, no. 4, pp. 969–997, 2014.

[229] K. P. Menard, *Dynamic mechanical analysis: a practical introduction*. CRC press, 2008.

[230] L. R. Finkenauer, Q. Lu, I. F. Hakem, C. Majidi, and M. R. Bockstaller, "Analysis of the Efficiency of Surfactant-Mediated Stabilization Reactions of EGaIn Nanodroplets," *Langmuir*, vol. 33, no. 38, pp. 9703–9710, 2017.

[231] B. Ozutemiz, J. Wissman, B. Ozdoganlar, and C. Majidi, "EGaIn-Metal Interfacing for Liquid Metal Circuitry and Microelectronics Integration," *Advanced Materials Interfaces*, vol. in press, pp. 1–13, 2018.

[232] S. Rich, S. H. Jang, Y. L. Park, and C. Majidi, "Liquid Metal-Conductive Thermoplastic Elastomer Integration for Low-Voltage Stiffness Tuning," *Advanced Materials Technologies*, vol. 2, no. 12, pp. 1–6, 2017.

[233] W. Shan, S. Diller, A. Tutcuoglu, and C. Majidi, "Rigidity-tuning conductive elastomer," *Smart Materials and Structures*, vol. 24, no. 6, 2015.

[234] M. D. Dickey, "Stretchable and Soft Electronics using Liquid Metals," *Advanced Materials*, vol. 29, no. 27, pp. 1–19, 2017.